Faculteit Wetenschappen
Departement Fysica

Advances in X-ray reconstruction algorithms for limited data problems in conventional and non-conventional projection geometries

---

Verbeteringen in X-stralen reconstructie algoritmes voor gelimiteerde dataproblemen in conventionele en niet-conventionele projectie geometrieën

Proefschrift voorgelegd tot het behalen van de graad van

Doctor in de Wetenschappen/Fysica

aan de Universiteit Antwerpen, te verdedigen door

Eline Janssens

Promotoren:
Prof. dr. Jan Sijbers
Dr. ir. Jan De Beenhouwer

Antwerpen, 2018

Doctoral committee

Dr. ir. Jan De Beenhouwer
Prof. dr. Joris Dirckx
Prof. dr. Jan Sijbers
Prof. dr. Sandra Van Aert

External jury members

Dr. Christoph Heinzl
Dr. Pieter Verboven

Contact information:

✉ **Eline Janssens**
imec-Vision Lab, Dept. of Physics
University of Antwerp (CDE)
Universiteitsplein 1, Building N1.09
B-2610 Wilrijk, Antwerpen, Belgium
☎ +32(0)3 265 24 49
janssens.eline@hotmail.com
http://visielab.uantwerpen.be/people/eline-janssens

Voorwoord

Table of Contents

Samenvatting

X-stralen *Computer Tomografie (CT)* is een krachtige beeldvormingstechniek die visualisatie van de interne structuur van een object mogelijk maakt door het opnemen van een reeks X-stralen projecties vanuit verschillende projectierichtingen. *Fase Contrast Computer Tomografie (PCCT)* is een uitbreiding van X-stralen CT waarmee zowel de verdeling van de imaginaire brekingsindex als de verstrooiing in een object gevisualiseerd kunnen worden. Beide technieken hebben veel toepassingen in verschillende domeinen zoals medische beeldvorming, materiaal wetenschap, inspectie, etc.

De kwaliteit van een reconstructie is sterk afhankelijk van het aantal opgenomen X-stralen projecties en hun angulaire verdeling. Vaak kan slechts een beperkt aantal X-stralen projecties opgenomen worden waardoor conventionele reconstructie-algorithmes (zoals FBP en SIRT) er niet in slagen goede reconstructies te maken. Bovendien zorgen niet-conventionele acquisitiegeometrieën voor extra uitdagingen in het reconstructieproces. Na de reconstructie en voor de beeldanalyse worden vaak nabewerkingsalgoritmes toegepast op de reconstructiedata om de analyse te vereenvoudigen. Segmentatie- en beeldfusie-algoritmes in het geval van PCCT zijn frequent gebruikte voorbeelden. Echter, de beelden na de nabewerking hebben dikwijls dezelfde artefacten als de gereconstrueerde beelden en de algoritmes vragen extra tijd.

De rode draad doorheen deze thesis is de zoektocht naar reconstructie-algoritmes die adequate reconstructies kunnen opleveren in het geval dat slechts een beperkt aantal projectiebeelden opgenomen kunnen worden. De sleutel hiertoe is het verrijken van de algoritmes met voorkennis over de objecten die geïnspecteerd worden. Deze voorkennis kan komen van de vorm of de materiaalsamenstelling van het object of van vorige scans van gelijkaardige objecten. De thesis is onderverdeeld in drie delen. In het eerste deel worden de basisconcepten van transmissie CT en PCCT uitgelegd. Het tweede deel focust op inline inspectie van objecten met transmissie X-stralen CT. Het reconstructie-algoritme dat hiervoor werd ontwikkeld werd toegepast op twee verschillende applicaties. In het derde deel is PCCT de belangrijkste beelvormingstechniek. Hier wordt een alternatief voorgesteld voor de wieg van Euler en worden beeldfusie en segmentatie gebruikt om de reconstructie kwaliteit te verbeteren van data die opgenomen is met een lage kwaliteit.

Deel I: Introductie

In de eerste twee hoofdstukken zal de lezer kennis maken met de basis van transmissie Computer Tomografie (hoofdstuk 1) en Fase Contrast Computer Tomografie

(hoofdstuk 2). Zowel de basis fysica achter X-stralen tomografie als de meest conventionele reconstructie-algoritmes worden besproken. De concepten die aangeraakt worden in deze hoofdstukken zijn cruciaal om de volgende hoofdstukken te begrijpen.

Deel II: Inline X-stralen inspectie

In dit deel staat de ontwikkeling van reconstructie-algoritmes voor inline kwaliteitsinspectie van producten centraal.

Hoofdstuk 3 – NN-hFBP voor snelle inline X-stralen inspectie

Door de hoge eisen van klanten in de voedingsindustrie stijgt de vraag naar individuele X-stralen inspectie van producten. De haalbaarheid van deze vraag hangt af van de snelheid van de acquisitie en de daaropvolgende reconstructie. Meestal wordt een afweging gemaakt tussen de reconstructietijd en de reconstructiekwaliteit. Conventionele reconstructie algoritmes zijn dikwijls ofwel snel maar presteren slecht met beperkte data ofwel vereisen ze te veel reconstructietijd.

In dit hoofdstuk introduceren we een snel reconstructie-algoritme voor de inline inspectie van objecten dat voorkennis gebruikt om de reconstructie te verbeteren. Data van eerder gescande objecten met reconstructies van goede kwaliteit wordt gebruikt om de filters van verschillende hFBP reconstructie algoritmes te trainen met een neuraal netwerk. De combinatie van deze hFBP reconstructies resulteert in een finaal reconstructiebeeld.

Het algoritme werd gevalideerd met simulatie data van appels en paprika's en reële scans van walnoten. D resultaten tonen dat het NN-hFBP algoritme in staat is om adequate reconstructies te verkrijgen in een zeer korte tijd die de reconstructie kwaliteit verkregen met FBP and SIRT overstijgen, waardoor individuele X-stralen inspectie haalbaar wordt.

Hoofdstuk 4 – Inline detectie van barsten

In een productie proces is het cruciaal dat defecten in individuele onderdelen vroeg gedetecteerd worden alvorens de componenten samengesteld worden in een groter product. Hierdoor kan het weggooien van andere, goede componenten vermeden worden. De inspectietijd is een belangrijke factor die mede bepaald of de individuele inspectie haalbaar is.

In dit hoofdstuk wordt een detectieprocess voorgesteld dat bestaat uit twee stappen: een stap waarin de objecten gereconstrueerd worden en daarop volgend een classificatiestap. In de eerste stap wordt het NN-hFBP algorithme, dat ontwikkeld werd in het vorige hoofdstuk, aangepast voor de inline inspectiegeometrie

van SVS adaptors. Vervolgens is een methode ontwikkeld om de barsten te detecteren op de gereconstrueerde afbeeldingen. Beide stappen moeten uitgevoerd worden in een zeer korte tijd.

Het algorithme werd gevalideerd op reële scans van SVS adaptors. De resultaten tonen dat de NN-hFBP voldoet aan de vereisten voor het inline reconstructiealgorithme en dat de detectie van de barsten uitgevoerd kan worden binnen een acceptabele tijd met een gelijkaardige accuraatheid.

Deel III: TLGI Reconstructie algoritmes

In dit deel worden twee methoden geïntroduceerd die als doel hebben om de reconstructiekwaliteit van TLGI data te verbeteren.

Hoofdstuk 5 – Dubbele-as Tomografie

Met een TLGI kunnen verstrooiing en faseveranderingen die veroorzaakt worden door een object enkel gemeten worden in één richting. Bovendien is de correctheid van de gemeten faseveranderingen sterk afhankelijk van de hoeveelheid verstrooiing. Hierdoor is de informatie in de projectiedata vaak onvolledige waardoor de resulterende reconstructies van lage kwaliteit zijn. Een wieg van Euler is een toestel waarmee veel projecties in verschillende vlakken opgenomen kunnen worden maar ten koste van een hoge acquisitietijd.
In dit hoofdstuk wordt een dubbele-as scan voorgesteld als een alternatief voor de wieg van Euler voor CFRP stalen. Hier wordt projectiedata van twee loodrechte oriëntaties opgenomen om de vezelbundels te visualiseren waardoor de acquisitietijd aanzienlijk daalt. Op basis van de opgenomen projectie data kan ook een verstrooiingstensor geconstrueerd worden in elke voxel.
Een eerste validatie van de method is gedaan op een CFRP staal. De dubbele-as reconstructies van DFC en DPC data bevatten duidelijk meer informatie en een hogere beeldkwaliteit in vergelijking met de conventionele reconstructies om één as.

Hoofdstuk 6 – Discrete Fase Contrast Computer Tomografie: MV-DART

Voor de detectie van vezelbundels in een CFRP staal wordt beeldsegmentatie uitgevoerd in PCCT op de gereconstrueerde AC, DFC en DPC beelden of op het gecombineerde beeld verkregen door beeldfusie. Hierdoor worden artefacten in de gereconstrueerde beelden doorgegeven naar het gefuseerde beeld en het gesegmenteerde beeld.

In dit hoofdstuk wordt het MV-DART algoritme met en zonder DFC weging voorgesteld waarmee een discreet reconstructiebeeld gecreëerd wordt gebaseerd op de gecombineerde informatie van de AC, DPC en DFC projectie data. Door

de combinatie van de verschillende modaliteiten in het reconstructie-algoritme, kunnen artefacten in een van de modaliteiten gecorrigeerd worden om een gefuseerd reconstructiebeeld te creëren. Omdat dit beeld discreet is, is geen additioneel segmentatie-algoritme vereist.

Eerste testen zijn uitgevoerd met het algoritme op simulatie en reële data. Ze tonen aan dat de combinatie van de modaliteiten in het reconstructie-algoritme de reconstructie kwaliteit significant verbetert in het geval dat geen onderscheid kan gemaakt worden tussen verschillende materialen in een modaliteit of wanneer de data van slechte kwaliteit is door artefacten.

Deel IV: Conclusies en Appendices

In dit deel worden algemene conclusies gepresenteerd over het werk dat besproken werd in de vorige hoofdstukken.

Summary

X-ray *Computed Tomography (CT)* is a very powerful imaging technique that allows to visualize the internal structure of an object non-destructively by acquiring a set of X-ray projection images at various projection directions. *Phase Contrast Computed Tomography (PCCT)* is an extension to X-ray CT in which both the distribution of the whole imaginary refractive index and the scattering inside an object are visualized. Both techniques have many applications in various fields such as medical imaging, materials science, inspection, etc.

The quality of a reconstruction is highly dependent on the number of X-ray projections and their angular distribution. Often, only limited projection data can be acquired, for which conventional reconstruction algorithms (like FBP and SIRT) fail to provide good reconstructions. Moreover, non-conventional acquisition geometries impose extra challenges on the reconstruction process. After reconstruction and prior to image analysis, post-processing algorithms are often performed on the reconstruction data that aid the analysis. Segmentation and image fusion algorithms in case of PCCT are frequently used examples. However, the images after post-processing often suffer from the same artefacts as the reconstructed images and the algorithms require additional time.

The central theme throughout this thesis is the search for reconstruction algorithms that still provide adequate reconstructions in case of limited projection data. The key here is to enrich the algorithm with prior knowledge on the objects that are inspected. This prior knowledge can be obtained from the shape or material composition of the object, or from previous scans of similar objects. The dissertation is divided into three parts. In the first part, the basic concepts of transmission CT and PCCT are explained. The second part focuses on inline inspection of objects with transmission X-ray CT. The algorithm is engineered for two different applications. In the third part, the main imaging method is PCCT. An alternative to the Eulerian cradle is proposed and image fusion and segmentation are used to improve the reconstruction quality of highly corrupted data.

Part I: Introduction

In the first two chapters, the reader will become familiar with the basics of transmission Computed Tomography (chapter 1) and Phase Contrast Computed Tomography (chapter 2). The basic physics behind X-ray imaging as well as the most conventional reconstruction algorithms are discussed. The concepts touched upon in these chapters are crucial to understand the remaining chapters.

Part II: Inline X-ray Inspection

This part focusses on the development of reconstruction algorithms for inline quality inspection of objects.

Chapter 3 – NN-hFBP for fast inline X-ray inspection

Due to high consumer demands in the food industry, the need for individual X-ray inspection of products arises. The feasibility of this demand depends on the speed of the imaging and subsequent reconstruction. Typically a trade-off is made between the reconstruction time and quality. Conventional reconstruction algorithms are often either fast but perform poorly with limited data or require too much reconstruction time.

In this chapter, we introduce a very fast reconstruction algorithm for inline inspection of objects that uses prior knowledge to improve the reconstruction. Data from previously scanned object with high quality reconstructions is used to train the filters of several hFBP reconstruction algorithms with a neural network. Combination of the hFBP reconstructions provides the final reconstruction image.

The algorithm is validated on simulation data of apples and bell peppers and real scans of walnuts. Results show that the NN-hFBP algorithm is capable of providing adequate reconstructions which surpass the reconstructions of FBP and SIRT in a very short time, making individual X-ray inspection feasible.

Chapter 4 – Inline Crack Detection

Early detection of defects in individual parts during the manufacturing process is crucial before the components are composed into a larger products. If early detection can be achieved, wasting other, good components can be avoided. The inspection time is an important factor indicating the feasibility of individual inline inspection.

In this chapter, a detection process is proposed consisting of two steps: an object reconstruction step and a classification step. In the first step, the NN-hFBP algorithm, developed in the previous chapter, is adapted for the inline inspection set-up of SVS adapters. Secondly, a crack detection method is developed that can be applied on the reconstructed images. Both steps should be performed in a very limited time.

The algorithm is validated on real scans of SVS adapters. Results show that the NN-hFBP meets the requirements for the inline reconstruction algorithm and the crack detection can be performed in an acceptable time frame with similar accuracy.

Part III: TLGI Reconstruction Algorithms

In this part, two methods are introduced that aim to improve the reconstruction quality of TLGI data.

Chapter 5 – Dual-axis Tomography

With a TLGI, the small angle scattering and phase shifts induced by the sample can only be measured in one direction. The accuracy of the phase shift measurement is furthermore highly dependent on the amount of scattering. The information in the projection data is therefore incomplete, which results in poor reconstructions. An Eulerian cradle is a piece of equipment that allows to acquire many projections in various planes but at the cost of a very large acquisition time.
In this chapter, a dual-axis scan is proposed as an alternative to the Eulerian cradle for CFRP samples. Projection data of two perpendicular orientations is acquired to visualize the fiber bundles, which highly reduces the acquisition time. Based on the projection data, a scattering tensor in each voxel can be constructed.
A first validation of the method is performed on a CFRP sample. The dual-axis reconstructions of DFC and DPC data clearly show additional information and an improved image quality compared to the single-axis reconstructions.

Chapter 6 – Discrete Phase Contrast Computed Tomography: MV-DART

For detection of fibre bundles in CFRP samples, posterior image segmentation is performed in PCCT on the reconstructed AC, DFC and DPC images or on a combined image obtained with posterior image fusion. As a result, artefacts in the reconstructed images propagate to the fused image and the segmented image.
In this chapter, the MV-DART algorithm with and without DFC weighting is proposed in which a discrete reconstruction image is created based on the combined information of the AC, DPC and DFC projection data. Due to combination of the different modalities in the reconstruction algorithm, artefacts in one modality can be corrected for in time before a fused reconstructed image is created. Since the fused image is discrete, no additional segmentation algorithm is required.
Preliminary tests are performed with the algorithm on simulated and real data. They indicate that combination of the modalities in the reconstruction algorithm can improve the reconstructed image in case different materials cannot be distinguished in one modality or when the data is of low quality due to artefacts. Further testing is however required for proper validation.

Part IV: Conclusions and Appendices

In this part, general conclusions on the work discussed in the previous chapters are presented.

Part I

Introduction

1

Transmission X-ray Tomography

Contents

In this chapter, a brief introduction is given on the physical processes underpinning X-ray imaging and the mathematical algorithms behind transmission Computed Tomography (CT). X-ray CT is an advanced imaging technique which allows to visualize the interior structure of objects non-destructively. A set of X-ray images or radiographic projections are taken around an object at different projection directions as shown in Fig. 1.1a. Based on the information enclosed in the projections, mathematical algorithms are used to reconstruct the interior structure of the object. The process is visualised in Fig. 1.1b. The chapter starts with a brief history on X-ray imaging and transmission CT. In Section 1.2, the physical process of how the X-ray projections are acquired is explained. After the generation of X-rays is discussed, a closer look is taken at their interactions with materials and finally the detection of X-rays is explained. The section ends with a description of the most common X-ray scanning geometries. The mathematical algorithms that can be used to obtain reconstructions are described in Section 1.3. They are divided in analytical, algebraic and statistical algorithms. Finally, the chapter ends with an overview of several applications of transmission X-ray CT.

1.1 History of transmission X-ray tomography

In 1895, the German physicist Wilhelm Conrad Röntgen (Fig. 1.2a) discovered an unknown type of radiation while experimenting with vacuum tubes. After placing a Crookes tube covered with cardboard in a dark room, he applied an electrical charge on it and discovered a fluorescent effect on a barium platinocyanide screen one meter away from the tube. He concluded that invisible rays were passing through the cardboard to make the screen glow, which he named X-rays. Röntgen published his work in a very short time frame [1] and received the Nobel Price for his discovery in 1901[2].

The first medical radiograph was made several weeks later when he photographed the hand of his wife with the newly discovered X-rays. The photograph is shown in Fig. 1.2b. Only then, the medical significance of his discovery became clear. In the next couple of years, X-ray scanners were widely used in everyday life, for example for shoe fitting and medical investigations. However, little by little, the dangourous side-effects of the X-rays became clear when people started complaining about bold spots, deformations, tumors etc. Soon it was understood that radiation with X-rays could be harmful and should be used with caution.
Despite their danger, X-rays are still valuable for diagnostic medical purposes. To improve their diagnostic value, it would be interesting to image slices through the body instead of radiographs. This is the concept of CT. To do tomography, one single radiograph is not sufficient. Several radiographs from different directions around the body have to be acquired to create good reconstructions of the body

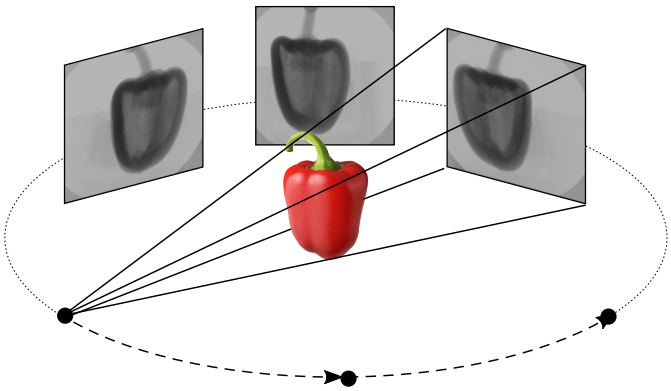

(a) Acquisition of several radiographic projections.

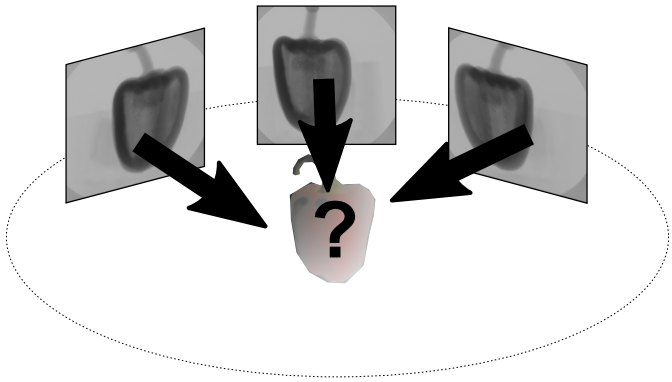

(b) Reconstrution of the interior structure based on the acquired projections.

Figure 1.1: Conceptual visualization of the two steps involved in X-ray CT of a bell pepper.

(a)

(b)

Figure 1.2: (a) Wilhelm Conrad Röntgen **(b)**The first X-ray image of the hand of Anna Bertha, Röntgen's wife [3].

slices. The basis for Computed Tomography was made by an Austrian mathematician Johann Radon through the introduction of the Radon Transform in 1917 [4]. This transform creates 1D projections from an object function $f(x, y)$ defined on a plane by taking line integrals. He also provided the inverse Radon Transform, which he knew could be used to reconstruct the original object function f. Further details on the Radon transform and its inverse will be given in Section 1.3.1.1.
In the 1930s, the first type of tomography, focal plane tomography, was developed by an Italian radiologist Alessandro Vallebona [5]. In focal plane tomography, the source and detector move simultaneously between two radiographs but in such a way to keep a consistent exposure of the plane of interest. This results in a reduction of the superposition of structures and a sharper plane of interest. The method has later on further developed to e.g. tomosynthesis. Despite this first type of tomography, it took until 1963 and 1964, before an American physicist Allan MacLeod Cormack published two papers on the theoretical substantiation of computed tomography [6, 7]. The publications initially only got little attention. The attention came when in 1967, Sir Godfrey Hounsfield invented the first commercial CT scanner [8], which put Cormack's theoretical underpinning in a real application. For their work, Cormack and Hounsfield recieved a Nobel Prize in 1979. Hounsfield first tested his CT scanner on a preserved human brain. In

1971, the scanner was introduced in medical practice, scanning a cerebral cyst of a patient in London.
Throughout the years, the world of medicine has gone through seven generations of CT scanners to obtain the high quality scans that are available today [9, 10]. First generation scanners existed of a single source and a single detector pixel at which a ray was casted as shown in Fig. 1.3a. To acquire a scan of one projection angle, the source and detector pixel performed a linear translation. This way the exact number of parallel rays could be defined manually. In the second generation scanners, the single detector pixel was replaced by several detector pixels placed in a line. As a result, a fan beam was captured. In the scanner, translation of the source and detector array was still needed for each projection angle to cover the whole field of view. The third generation scanner has a fan-beam geometry. Fig. 1.3b shows a schematic. In this scanner, the source is fixed in the middle and a large array of detector pixels is placed on the opposite side. The fan-beam from the source to the detector pixels covers the whole region of interest, and therefore, translation is not necessary, causing a great decrease in scanning time. A fourth generation CT-scanner is shown in Fig. 1.3c. The detectors form a fixed ring around the object to be scanned and the source rotates in between. The scanner has a higher detector efficiency, but the results are compromised by scattering. The fifth generation CT scanner is an electron beam computed tomography (EBCT) scanner. An electron beam swipes around a semicircular tungsten anode target so that the focal spot moves around the patient and generates X-rays that are collimated in a fan-beam and pass through the patient. The X-rays are detected on a large detector ring as in the fourth generation scanners. The advantage of the method is that the scanning is very fast and the source and detector do not rotate, but the system is very expensive. The sixth generation CT scanner (Fig. 1.3d) is called the helical CT. Here, the source and detector rotate around the patient as in the third or fourth generation CT scanner, while the patient translates through the source detector plane. In this way, several planes throughout the body can be scanned simultaneously. The seventh generation CT scanner is the multislice CT and emerges from the need for scanning multiple slices at the same time. The detector has expanded to multiple rows of detector pixels, which are all at the same time irradiated as demonstrated in Fig. 1.3e. The scanner is called a cone-beam CT scanner. Details on the parallel-beam, fan-beam and cone-beam scanning geometries will be given in Section 1.2.4. Finally, nowadays the helical and cone-beam scanner are often combined as in Fig. 1.3f to further reduce the scanning time.

Today, X-ray CT is also an important technique for biomedical research and material science. For these applications, scanning is performed by a μCT scanner. The scanners are often from the seventh generation or combine the cone-beam and helical CT scanner and have a very high spatial resolution. An example

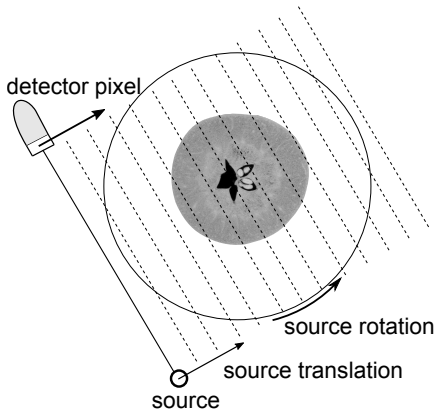

(a) First generation scanner: parallel beam

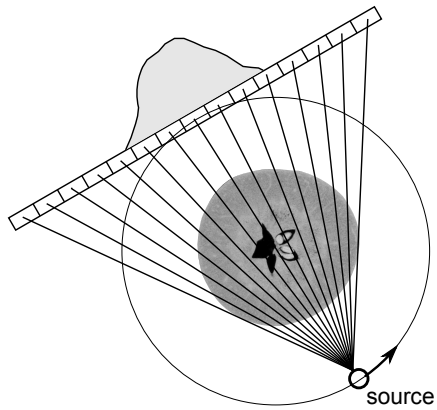

(b) Third generation scanner: fan beam

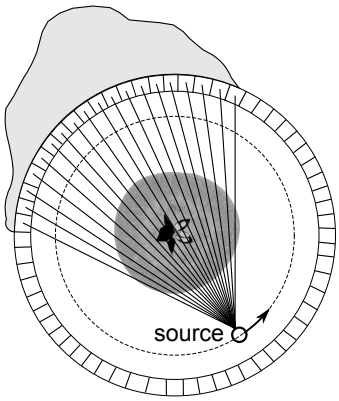

(c) Fourth generation scanner

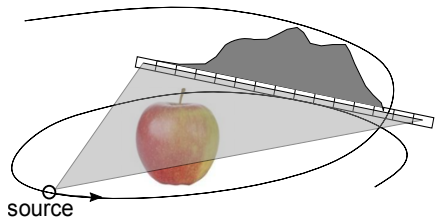

(d) Sixth generation scanner: helical scan

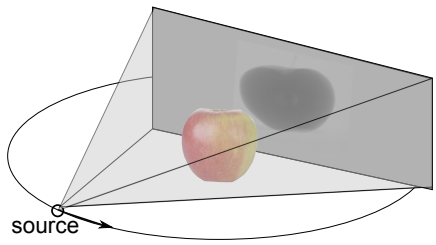

(e) Seventh generation scanner: circular cone beam

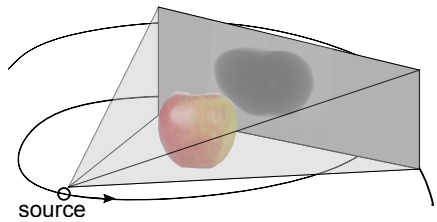

(f) Combination of sixth and seventh generation scanner: helical cone beam

Figure 1.3: Different generations of scanners

of a μCT scanner is shown in Fig. 1.4a. Another way to scan biomedical and material samples is at a synchrotron facility. A schematic of a synchrotron facility is shown in Fig. 1.4b. There, electrons are accelerated to very high velocities that approximate the speed of light. When these electrons are forced to change direction, the emitted energy is in the X-ray wavelength. The resulting X-ray beam is quasi monochromatic and has a high signal-to-noise ratio, which allows high quality reconstructions [11].

(a) **(b)**

Figure 1.4: (a) micro-CT scanner of Bruker MicroCT: Bruker micro-CT Skyscan 1272 **(b)** A photograph of the ESRF synchrotron facility near Grenoble in France.

Although very high quality scanners are available today, challenges remain. Driven by time, cost and ethical constraints, a short scan time with few projections is often preferred with the drawback of a noisy reconstruction corrupted with artefacts. Therefore, much work is done on improving the reconstruction algorithms which translate the recorded projection data into a 3D rendering of the scanned volume. In Section 1.3.1 and Section 1.3.2, more details will be given on these reconstruction algorithms.

1.2 Image Acquisition

In this section, the acquisition process for an X-ray image or radiograph is considered. Therefore, the physics behind X-ray imaging are explained. First, the generation of X-rays is discussed in Section 1.2.1. Then in Section 1.2.2 a closer look is taken at the interactions that X-rays undergo when they pass through a sample. Section 1.2.3 describes the detection of X-rays. And since the measured projection images are dependent on the type of projection geometry in the scanner, in Section 1.2.4, different projection geometries are studied.

1.2.1 X-rays generation

X-rays are a type of electromagnetic radiation with an energy range between 100eV and 100keV, wavelength between 10pm and 10nm and a frequency between $30 \cdot 10^{12}$Hz and $30 \cdot 10^{15}$ Hz. They have wave-like properties that can be measured by studying their interference pattern. On the other hand, they also exhibit particle-like properties. In that case, they are described by a flow of photons with a specific energy spectrum. In this chapter, we focus on the particle behaviour of the X-rays, while the wave properties will be discussed in the next chapter.
The first X-rays were produced with a Crookes tube in 1895. Modern X-ray tubes are a variant of the improved Coolidge tube [12]. An X-ray tube is a vacuum tube with a tungsten filament that functions as a cathode through which an electric current is sent and an anode that is often made of molybdenum coated with a rhenium-alloyed tungsten. Fig. 1.6a shows a schematic of an X-ray tube. Through a process called thermionic emission, the filament is heated until the thermal energy exceeds the binding energy of the electrons of the filament and they are discharged in a cloud around the filament. When a high voltage is then applied on the anode, the electrons are accelerated towards the anode, creating a tube current typically between 1 and 1200mA. When the electrons hit the anode, they interact with the rhenium-tungsten material and emit a spectrum of X-rays. Two types of interactions occur at the tungsten surface of the anode [9]:

- The incoming electron interacts with the nuclei of the surrounding atoms. The positive charge of a nucleus attracts the moving electron causing the electron to bend and decelerate. The loss in kinetic energy is converted to electromagnetic photons. When the electron hits the nucleus, this energy loss is maximum and equal to the anode-cathode potential. Typically, a continuous spectrum of radiation is obtained which is referred to as *brehmsstrahlung*. It is the smooth part of the X-ray spectrum in Fig. 1.5. Due to brehmsstrahlung, X-ray sources are polychromatic. Photons with a very low energy are more likely to be created but are often absorbed by the anode itself, causing the brehmsstrahlung outside the tube to be zero at these energies. The intensity of the brehmsstrahlung increases with the energy of the incident electron and with the atomic number of the atom with which it interacts.

- The incoming electron ionizes the atom by collision with a K-shell electron. Electrons from other shells can then fill in the vacancy of the missing electron, while radiating an electromagnetic wave with a specific energy equal to the difference in binding energy between the two shells. The binding energies of the electrons on the different shells is fixed, giving the photons discrete energy levels. The emitted photons are called *characteristic x-rays* and represent the peaks in Fig. 1.5. For characteristic X-rays to be generated, the energy

of the electrons should be sufficient to eject K-shell atoms. For a tungsten anode, this energy should be at lease 57.984 keV.

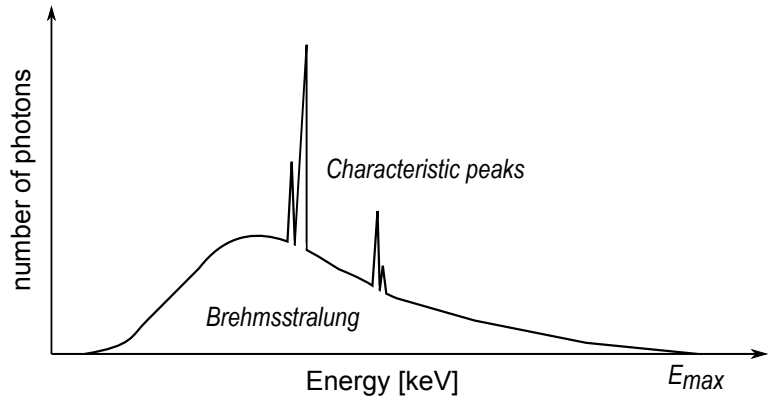

Figure 1.5: Schematic of the spectrum of X-rays that leave the X-ray tube.

An important issue of X-ray tubes is the production of heat. The filament is made of Tungsten since it has a very high melting point (3370°C), but the largest problem occurs at the side of the anode. When the electrons accelerate towards the anode, they are focused on a small spot of the anode, the focal spot. The size of this spot is inversely related to the clarity of the measured projection images. A larger spot size causes penumbra blurring and decreases the spatial resolution of the X-ray projection. The modulation transfer function is a mathematical expression that measures the image quality of the projection images. When the electron beam hits the focal spot, only 1% of its kinetic energy is converted to X-rays, the other 99% is converted to heat. By using a rotating anode disk, the heat can be distributed more evenly over the anode. This anode is often used in medical CT. The focal spot size that can be achieved with a rotating anode is however too large for microCT applications. Microfocus X-ray tubes can achieve focal spot sizes of 5-20μm but at the cost of a very low power [13]. For instance, an X-ray tube with a focal spot size of 10μm can only reach a power of 4-10W. An alternative is to use a metal-jet-anode microfocus X-ray tube, where the anode is replaced by a jet of liquid metal for better heat dissipation. With this X-ray tube, small focal spot sizes can be achieved with a higher power [14, 15]. A metal-jet-anode microfocus X-ray tube with the same focal spot size of 10μm as in the previous example can now reach a power of 30-60W. The importance of the focal spot size is shown in Fig. 1.6b.
A different way to generate X-rays is with a synchrotron light source. There,

electron bundles are accelerated to a very high speed and then forced into a circular path by magnets. Due to this deviation from a straight path, X-rays are emitted with a energy directly related to the velocity of the electron bundle. The main advantages of the resulting X-rays beams are that they are monochromatic and have a high flux and brilliance [11, 16].

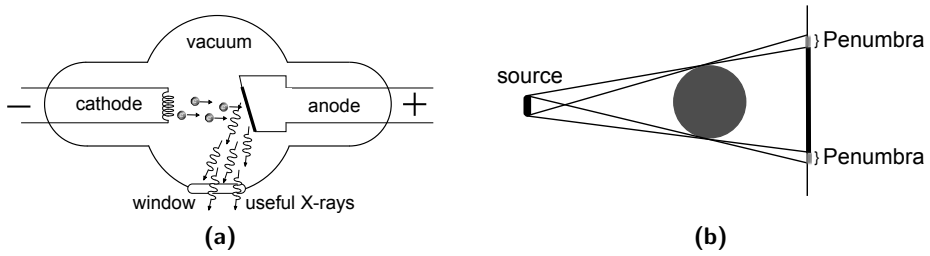

Figure 1.6: (a) schematic of an X-ray tube **(b)** Penumbra blurring

1.2.2 X-ray - matter interactions

Visualization of internal structures with X-rays is possible due to their interacting behaviour when passing through material. When the X-rays leave the X-ray tube, they have an initial intensity I_0. This intensity decreases along their path through interactions with material. The intensity at each point along the path can be written as $I(\xi)$ where ξ denotes the position along the path of the X-rays. The most important interactions that can occur between a photon and matter are:

- **The Photoelectric effect:** The incident photon interacts with the Coulomb field of the nucleus. It is completely absorbed by the atom, causing the ejection of a photoelectron with an energy equal to the difference between the energy of the photon and the electron's binding energy. The vacancy in the atom is then filled with an electron from a higher shell, creating another photon (Fig. 1.7a).

- **Coherent scattering:** The energy of the incident photon is not enough to eject an electron from its orbit as in Compton scattering. Therefore, the energy of the photon remains unchanged but the photon changes direction. Thomson scattering and Rayleigh scattering are two examples of coherent scattering (Fig. 1.7b).

- **Compton Scattering:** The incident photon strikes a valence electron and

ejects it from its orbit. Hereby, it changes direction and part of its energy is transferred to the recoil electron (Fig. 1.7c).

- **Pair production:** By incidence of a photon with an energy that exceeds twice the electron rest mass energy, the photon is absorbed and an electron-positron pair is created. The kinetic energy of the pair is dependent on the difference between the energy of the photon and twice the electron rest mass energy [17] (Fig. 1.7d).

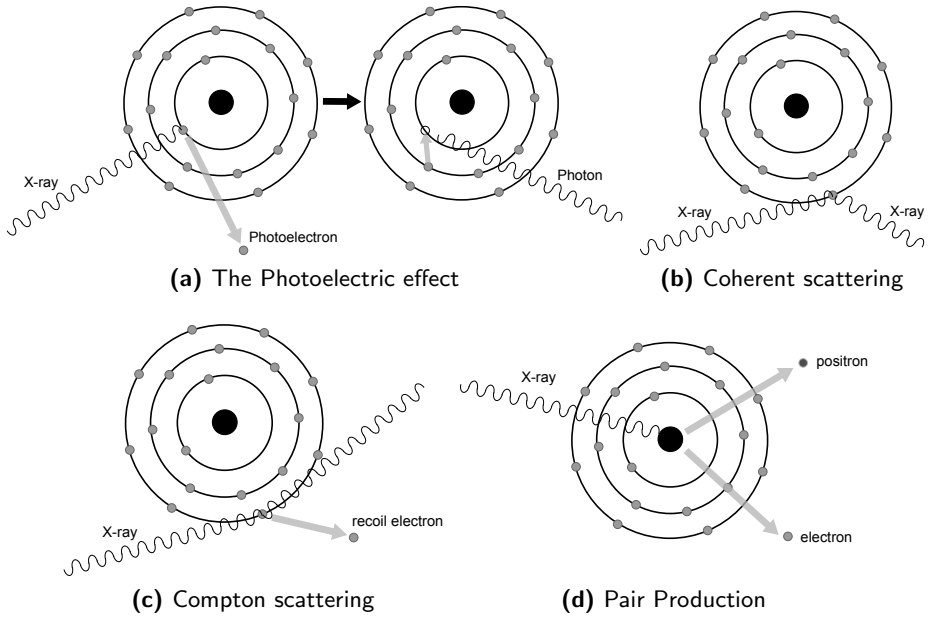

(a) The Photoelectric effect **(b)** Coherent scattering

(c) Compton scattering **(d)** Pair Production

Figure 1.7: Various types of interactions between X-rays and material

From the four interactions, pair production never occurs for medical inspection since the required energy of the incident photon clearly exceeds the photon energy of clinical X-rays. Coherent scattering occurs very rarely and is therefore not relevant for transmission X-ray inspection. However, in the next chapter, scattering inside the object will be measured and visualized. Therefore, this type of interaction is included in the list. For transmission X-ray imaging, the photoelectric effect and Compton scattering are the two main interactions that reduce the measured X-ray intensity. The likelihood of all previous effects happening in a material is captured in the attenuation coefficient μ of the material, which depends on its

atomic number. When an X-ray beam passes a distance $\Delta\xi$ through a material where the attenuation factor is constant, the radiation intensity before the material $I(\xi)$ is then decreased based on the distance and the attenuation factor. The radiation intensity after the distance becomes:

$$I(\xi + \Delta\xi) = I(\xi) - \mu(\xi)\Delta\xi I(\xi). \tag{1.1}$$

From this equation, the Lambert-Beer law can be derived. The law describes the exponential reduction of the intensity along an X-ray beam when it passes through a material.

$$I = I_0 e^{-\int_0^s \mu(\xi)d\xi}. \tag{1.2}$$

Here, the intensity of the X-rays exponentially decreases along the line of the line integral and the initial intensity I_0 is known.

1.2.3 X-ray detection

After passing through an object, the X-ray beam has a certain intensity I. This intensity is measured by a detector. The X-ray detector that Röntgen used was a photographic plate. The first digital detector for radiography was a phosphor plate, on which X-rays were recorded using photostimulated luminescence [18]. Nowadays, in CT, flat panel detectors are widely used. They either directly convert X-ray photons into an electrical charge or convert X-ray photons into visible light, which is subsequently converted to an electrical charge. From the electrical charge, a digital image is created. Some important parameters for an X-ray detector are its size, frame rate, spatial resolution, cost, dynamic range, uniformity, noise characteristic, sensitivity, quantum efficiency and cost [19, 20].
The intensity that is measured at the detector can be described by the Beer-Lambert law. However, ultimately, we are interested in the attenuation values μ along the projection line. Therefore, before applying a reconstruction algorithm to obtain these values, two preprocessing steps are performed. The first step is a *flatfield correction* step, where the measured intensity is divided by the initial intensity. In the second step, the negative logarithm is taken of the flatfield corrected projections. This step is called *log correction*. Finally, the projection data p that is used for image reconstruction is given in Eq. 1.3.

$$p = \int_0^s \mu(\xi)d\xi = -\ln\left(\frac{I}{I_0}\right). \tag{1.3}$$

Eq. 1.2 and 1.3 are given for a monochromatic X-ray beam.

1.2.4 Projection geometries

A reconstruction algorithms allows to create an image which visualizes the distribution of the attenuation coefficients inside a volume. The form of the algorithm depends on the projection geometry with which the X-ray images are acquired. In this subsection, the most common projection geometries are discussed.
In 2D imaging, the most common geometries are a *parallel beam* or a *fan beam* geometry. Typically, in both geometries, the source and detector rotate around the object along a circular path. In parallel beam, the rays from source to detector are parallel to each other. This can in practice only be achieved in a lab when the source translates in a direction perpendicular to the casted rays (Fig. 1.3a). In a fan beam geometry, the rays start from one point and open towards the detector in the shape of a fan (Fig. 1.3b).
The equivalents of a parallel beam and fan beam geometry in 3D imaging are a *parallel beam* geometry in 3D and a *cone beam* geometry. The parallel beam geometry is similar to the 2D equivalent, only the rays are now emitted on a plane instead of a detector line. This geometry can be achieved at a synchrotron facility. In a cone beam geometry, the photons form a cone from the source towards a 2D detector. Two types of cone beam geometries are often used: a *circular cone beam* geometry (Fig. 1.3e) and a *helical cone beam* geometry (Fig. 1.3f). In the first geometry, the source and detector perform a circular path around the object. In the second geometry, the source and detector describe a helical path around the object. The last one is commonly used in medical CT. The geometries described here are the most common X-ray scanning geometries. They are however not limited to these examples. In Chapter 3 another scanning geometry will be described.

1.3 Reconstruction Methods

In the previous section, the acquisition of X-ray images or radiographs has been discussed. Although X-ray images are valuable for example in different types of inspection [21, 22, 23, 24], they do not provide detailed spatial information on the scanned object since the projection accumulates all the attenuation values along a line and projects them onto one detector pixel. To retreive the 3D information of a sample, a *reconstruction algorithm* is required. This is an algorithm that takes the 2D projections along many projection directions as an input and generates 3D spatial information on the distribution of the attenuation coefficients at the inside of an object as an output. Typically, reconstruction algorithms are divided into 3 types: *analytical, algebraic and statistical* reconstruction algorithms. These will be discussed in Section 1.3.1-1.3.3.

1.3.1 Analytical reconstruction methods

Analytical reconstruction methods tend to reconstruct an object function $f(x, y)$, which contains the attenuation coefficients μ at positions (x, y). The Radon transform, described in Section 1.3.1.1 provides the mathematical basis for analytical reconstruction methods. An important theorem for the Filtered Back Projection is described in Section 1.3.1.3. After which the Filtered Back Projection is described in Section 1.3.1.4 for parallel beam and in Section 1.3.1.5 for fan beam data. The main advantage of analytical reconstruction methods is their short reconstruction time. Therefore, they are commonly used. Their major drawbacks are that their projection geometry should be fixed and that they are inflexible in terms of incorporating prior knowledge. The section ends with a description of some 3D reconstruction methods and some analytical methods that try to exploit prior knowledge.

1.3.1.1 Radon transform

In 2D parallel beam X-ray imaging, X-rays are passing through a sample as parallel rays. Hereby, a 2D image $f(x, y)$ is mapped onto a 1D projection. The process is mathematically described by the Radon Transform [4, 25], where each ray is represented as a line L. Each line L is then characterized by a certain projection angle θ and a distance l to the origin. The projection angle θ is measured counterclockwise with respect to the y-axis. The lines are defined in 2D space as:

$$L(l, \theta) = \{(x, y) \in \mathbb{R}^2 | x\cos\theta + y\sin\theta = l\}. \tag{1.4}$$

The line integral through the function $f(x, y)$ along line $L(l, \theta)$ is then given by:

$$p_\theta(l) = \int_{L(l,\theta)} f(x, y)ds, \tag{1.5}$$

which can also be written as:

$$p_\theta(l) = \int_{-\infty}^{\infty}\int_{-\infty}^{\infty} f(x, y)\delta(x\cos\theta + y\sin\theta - l)dxdy. \tag{1.6}$$

This projection function $p_\theta(l)$ is equal to the log- and flatfield corrected projection data recorded in X-ray imaging, since the projection data is the line integral of the attenuation coefficients μ corresponding to each point (x, y) (Eq. 1.3). The projection function is also the Radon transform $\mathcal{R}f$ of $f(x, y)$ at position (l, θ). More generally, the Radon transform $\mathcal{R}$ is a transformation that maps the function

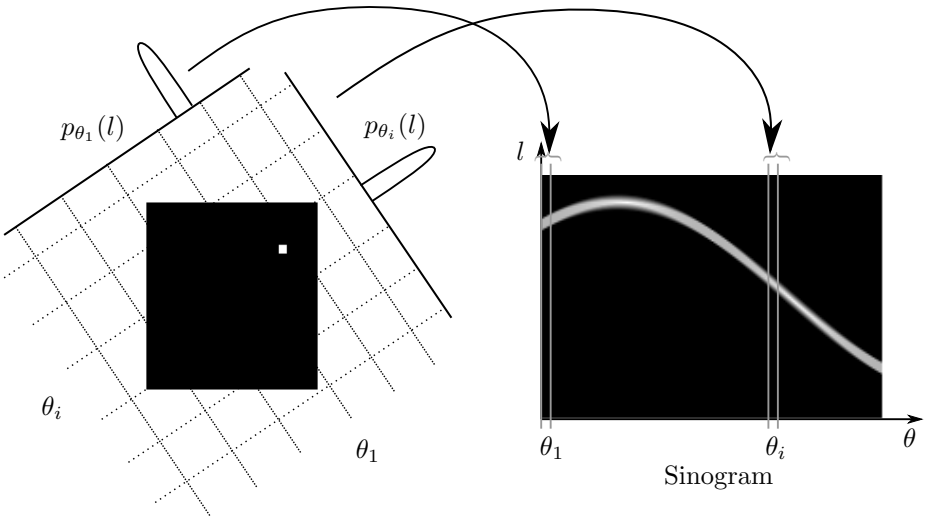

Figure 1.8: Creation of a sinogram by an off-center point.

$f(x, y)$ on the complete set of projection data:

$$f(x,y) \overset{\mathcal{R}}{\longleftrightarrow} \{p_\theta(l) | \theta \in [0, \pi[, l \in \mathbb{R}\}. \tag{1.7}$$

The projection data is often called a *sinogram*, since an off-center point in the object function describes a sinusoid in the projection data as shown in Fig. 1.8.

1.3.1.2 Simple Back Projection

The Radon transform provides useful information in the projection process of CT. It is however the inverse problem that should be solved for reconstruction. It is not straightforward to retrieve the attenuation values of the object function based on the measured projection data. The most basic way to do so, is to smear out the projection data as a constant value along the lines of the line integrals. The reconstruction formula then becomes:

$$f(x,y) = \int_0^\pi p(l,\theta)|_{l=x\cos\theta+y\sin\theta} d\theta. \tag{1.8}$$

The reconstructions obtained with a simple back projection are blurry. After all, the smearing operation is not the exact inverse of the Radon transform. A reconstruction of the Shepp-Logan phantom [26] made with the Simple Back Projection algorithm is shown in Fig. 1.11a. To obtain better reconstructions, more advanced

methods are considered in the next sections. A simple back projection however often serves as a base for more complex reconstruction algorithms.

1.3.1.3 Fourier slice theorem

Another way to retrieve the attenuation values of an object function based on its projection data is by exploiting the Fourier Slice Theorem. This theorem is the key to most analytical tomographic reconstruction algorithms. It states that the 1D Fourier transform of the projection data $p_\theta(l)$ is equal to a slice of the two dimensional Fourier transform of the original object at angle θ [27, 28]. Theoretically, based on the projection data, the original object can then be recovered by performing a 2D inverse Fourier Transform. To proof the the Fourier Slice Theorem, one starts with the two-dimensional Fourier transform of the object function:

$$F(u,v) = \int_{-\infty}^{\infty}\int_{-\infty}^{\infty} f(x,y)e^{-i2\pi(ux+vy)}dxdy. \tag{1.9}$$

Likewise, the one dimensional Fourier transform of a projection at angle θ is defined as:

$$P_\theta(\omega) = \int_{-\infty}^{\infty} p_\theta(l)e^{-i2\pi\omega l}dl. \tag{1.10}$$

The projection data $p_\theta(l)$ can be replaced by the line integral of Eq. 1.6:

$$P_\theta(\omega) = \int_{-\infty}^{\infty}\left[\int_{-\infty}^{\infty}\int_{-\infty}^{\infty} f(x,y)\delta(x\cos\theta + y\sin\theta - l)dxdy\right]e^{-i2\pi\omega l}dl, \tag{1.11}$$

$$P_\theta(\omega) = \int_{-\infty}^{\infty}\int_{-\infty}^{\infty} f(x,y)e^{-i2\pi\omega(x\cos\theta+y\sin\theta)}dxdy. \tag{1.12}$$

Comparing this equation to the two-dimensional Fourier transform of the object function yields the following equality:

$$P_\theta(\omega) = F(\omega\cos\theta, \omega\sin\theta). \tag{1.13}$$

This proves that the one dimensional Fourier transform of a projection slice equals a slice through the two-dimensional Fourier transform of the object function and it is exactly the slice at angle θ. Fig. 1.9 shows a visual representation of the Fourier Slice Theorem.

In tomography, various projections around the object are taken. When an infinite number of projections could be acquired, the whole frequency space would be sampled and $F(u,v)$ would be known at all points in the uv-plane. In that case, the original object function could be retrieved by performing an inverse

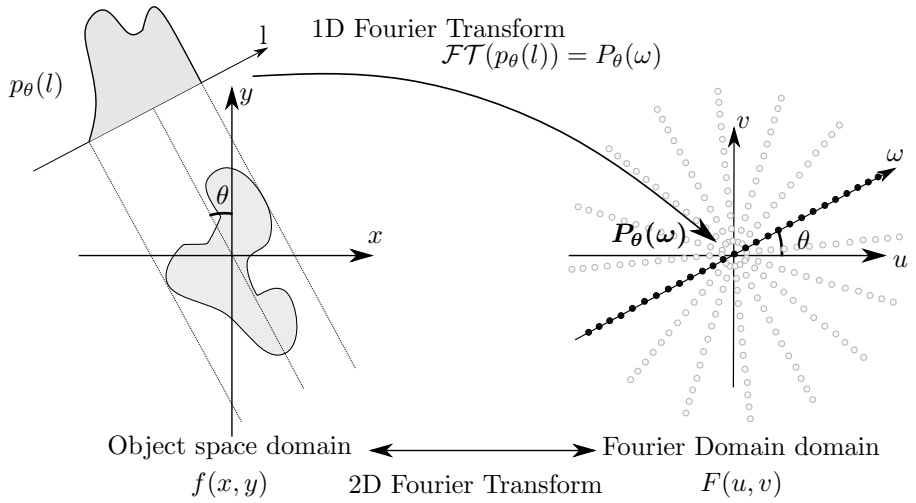

Figure 1.9: The Fourier Slice Theorem

Fourier Transform on $F(u, v)$. In practice however, the number of projections is always finite causing $F(u, v)$ to be known only along a finite number of radial lines as shown by the grey circles in Fig. 1.10. To perform the inverse Fourier transform on the Fourier data by the Fast Fourier Transform (FFT) algorithm [29], the datapoints should be positioned on a regular grid, shown by the squares in Fig. 1.10. Therefore, to reconstruct the data, interpolation in the Fourier space is first required. Since the measured data points are positioned on radial lines, the density of the radial points gets sparser for higher frequencies. This implies an increase in the interpolation error for higher frequencies and reconstructions made with the interpolated inverse FFT will be degraded and blurry. Although this reconstruction method is not the preferred choice, other reconstruction algorithms, like the Filtered Back Projection discussed in the next section, are built upon the Fourier Slice Theorem.

1.3.1.4 Filtered Back Projection for parallel beam

To overcome the problems of the Fourier Slice Theorem, the Filtered Back Projection (FBP) algorithm is introduced [27, 28] . This algorithm incorporates an extra filtering operation and replaces the inverse Fourier Transform by the previously introduced simple back projection. To derive the FBP algorithm, one starts from the inverse Fourier Transform, but instead of using the squared coordinate system (u, v), a polar coordinate system (q, θ) is considered implying the following

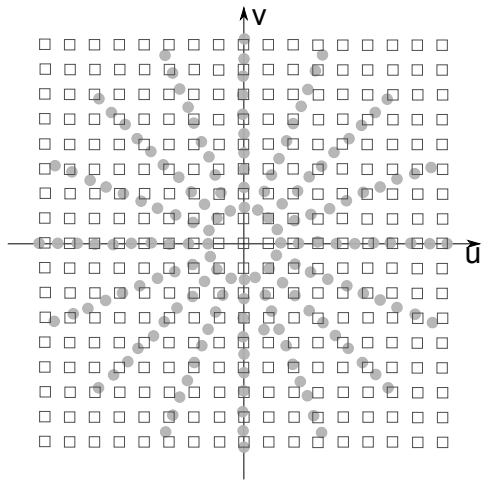

Figure 1.10: Sampling of the Fourier space. Grey dots: radial sampling obtained by a FFT of the projection data. Squares: regular sampling needed for inverse FFT.

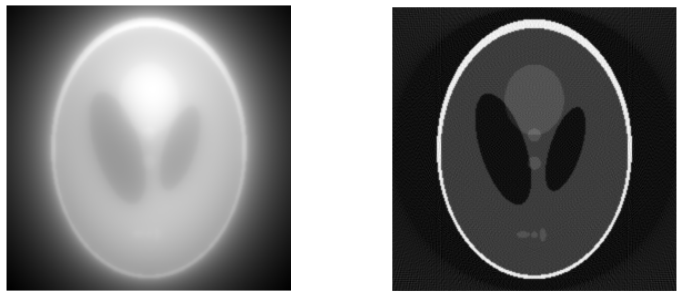

(a) Simple Back Projection **(b)** Filtered Back Projection

Figure 1.11: Two different back projection algorithms.

conversions:

$$u = q\cos\theta, \tag{1.14}$$

$$v = q\sin\theta, \tag{1.15}$$

$$dudv = qdqd\theta. \tag{1.16}$$

The reconstruction formula then becomes:

$$f(x,y) = \int_0^{2\pi} \int_0^{\infty} F(q,\theta) e^{i2\pi q(x\cos\theta + y\sin\theta)} qdqd\theta. \tag{1.17}$$

Since $F(q,\theta+\pi) = F(-q,\theta)$, the equation can be rewritten as:

$$f(x,y) = \int_0^{\pi} \int_{-\infty}^{\infty} F(q,\theta)|q| e^{i2\pi q(x\cos\theta + y\sin\theta)} dqd\theta. \tag{1.18}$$

In a final step, the two-dimensional Fourier transform can be replaced by the Fourier transform of the projection data as stated by the Fourier Slice Theorem (Eq. 1.13).

$$f(x,y) = \int_0^{\pi} \left[\int_{-\infty}^{\infty} P_\theta(q)|q| e^{i2\pi q(x\cos\theta + y\sin\theta)} dq \right] d\theta. \tag{1.19}$$

Eq. 1.19 is the reconstruction equation for the Filtered Back Projection algorithm. As can be derived from the equation, the reconstruction algorithm consists of four steps, which are visually illustrated in Fig. 1.12:

1. The one-dimensional Fourier transform of the projection data is taken to obtain $P_\theta(q)$.

2. The Fourier transformed projection data is filtered with the ramp filter $|q|$. The filter is a high-pass filter which compensates for the lower sampling of the data in the high frequencies. This way, the blurring is minimised and the contrasts are accentuated.

3. The inverse Fourier transform of the filtered projection data is taken.

4. For a pixel (x,y), the projection data at $l = x\cos\theta + y\sin\theta$ for all projection angles θ is summed to obtain the reconstruction value $f(x,y)$. The is done by back projecting the projection data along the lines $l = x\cos\theta + y\sin\theta$ as explained in Section 1.3.1.2.

The FBP can both be applied in the Fourier domain and in the spatial domain as shown in Fig. 1.12. In the latter, the filtering is done by a convolution of

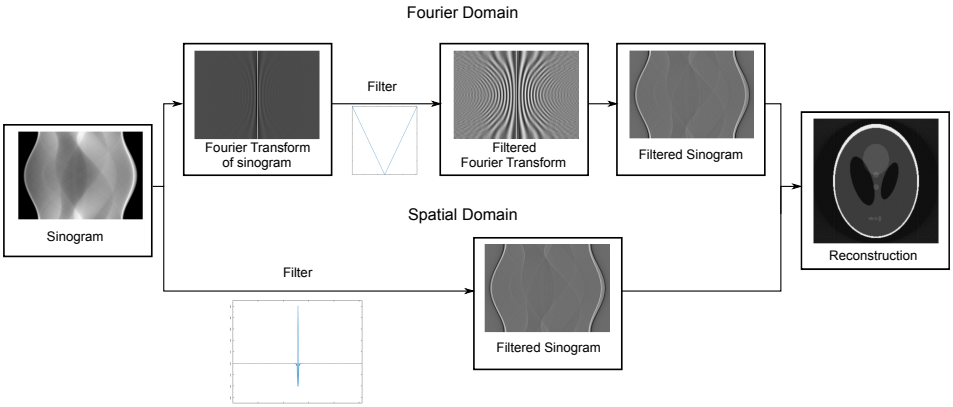

Figure 1.12: A reconstruction scheme for the FBP algorithm, applied in both the Fourier and the Spatial Domain

the projection data with the inverse Fourier transform of the ramp filter. The reconstruction algorithm then becomes:

$$f(x,y) = \int_0^{\pi} \left[\int_{-\infty}^{\infty} p_\theta(l) g(x\cos\theta + y\sin\theta - l) dl \right] d\theta, \tag{1.20}$$

where $g(x\cos\theta + y\sin\theta - l)$ in the spatial domain is the inverse Fourier transform of the ramp filter $|q|$ in the Fourier domain. In practical implementations of the FBP, the algorithm is often calculated on all coordinate pixels at the same time. Hence, the FBP is a very fast reconstruction algorithm. This is the main advantage of the technique and therefore, it is widely used in practice. Another advantage is that the algorithm is mathematically correct. If an infinite number of projections could be taken and the size of a detector pixel could be infinitesimal, then the exact object could be reconstructed. In practice, the number of projections is finite and a detector pixel has a certain size. Therefore, the reconstruction formula should be discretized. Fortunately, this has little impact on the reconstruction quality. The FBP algorithm is a good choice to reconstruct images if the following conditions apply to the situation:

- The number of projections is directly related to the sampling of the frequency space. When the sampling is too low, artefacts appear in the reconstructions in the form of streaks and stripes as shown in Fig. 1.13a. To obtain high quality reconstructions with the FBP algorithm, the number of projections should be sufficiently high.
- It is important that the projections sample the whole angular range of θ:

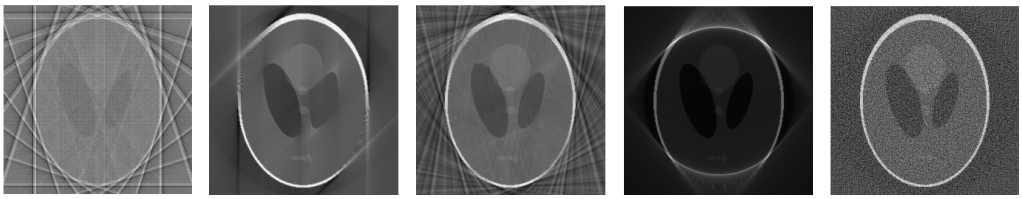

(a) **(b)** **(c)** **(d)** **(e)**

Figure 1.13: Artefacts that appear in the FBP reconstruction image under non-ideal circumstances: **(a)** Limited number of projection **(b)** Missing wedge artefacts **(c)** Non-equally sampled projections **(d)** Truncation artefacts and **(e)** Noisy projection data.

$[0, \pi[$. If the angular range is smaller than π, part of the Fourier space is not sampled. This results in *missing wedge artefacts* in the reconstructions (Fig. 1.13b).

- The projections should be equally sampled over the range $[0, \pi[$. When the sampling is nonuniformly distributed, some parts of the Fourier space are more densely sampled than others. This also leads to artefacts in the reconstructions which are demonstrated in Fig. 1.13c.
- The object that is scanned should be completely in the field of view of the source and detector. When part of the object is not irradiated in a projection, the final reconstruction image will suffer from *truncation artefacts* (Fig. 1.13d).
- The signal-to-noise ratio of the acquired scans should be very high. The FBP is very susceptible to noise in the projection data. Noisy projection data result typically in noisy reconstruction images (Fig. 1.13e).

A disadvantage of the FBP and analytical reconstruction methods in general is that they are not flexible. It is very difficult to impose prior knowledge on the algorithm. In experimental scans, where prior knowledge can improve the reconstructions, the FBP is therefore rarely the best choice.

On a side note, the FBP can also be rewritten to create the Hilbert transform based FBP. To do so, one rewrites the ramp filter $|q|$ as $q\ \mathrm{sign}(q)$ where

$$\mathrm{sign}(q) = \begin{cases} 1 & \text{if } q > 0. \\ 0 & \text{if } q = 0. \\ -1 & \text{if } q < 0. \end{cases} \tag{1.21}$$

The inner integral of Eq. 1.19 can then be multiplied by $(2\pi^2 i/2\pi^2 i)$ and rewritten as

$$h_\theta(l) = \frac{1}{2\pi^2}\int_{-\infty}^{\infty} i2\pi q P_\theta(q)\left(\frac{\pi}{i}\text{sign}(q)\right)e^{i2\pi q(x\cos\theta + y\sin\theta)}dq. \tag{1.22}$$

In the space domain, Eq. 1.22 is equal to the convolution of the inverse Fourier transform of $(i2\pi q P_\theta(q))$ and the inverse Fourier transform of $(\frac{\pi}{i}\text{sign}(q))$. These inverse Fourier transforms are:

$$2\pi i q P_\theta(q) \xrightarrow{\mathcal{F}^{-1}} \frac{dp_\theta(l)}{dl}, \tag{1.23}$$

$$\frac{\pi}{i}\text{sign}(q) \xrightarrow{\mathcal{F}^{-1}} \frac{1}{l}. \tag{1.24}$$

Eq. 1.22 can then be rewritten in the space domain as:

$$h_\theta(l) = \frac{1}{2\pi^2}\left(\frac{1}{l} * \frac{dp_\theta(l)}{dl}\right), \tag{1.25}$$

$$= \frac{1}{2\pi^2}\int_{-\infty}^{\infty}\frac{1}{l-t}\frac{dp_\theta(t)}{dt}dt, \tag{1.26}$$

$$= \frac{1}{2\pi}\mathcal{H}\left\{\frac{dp_\theta(l)}{dl}\right\}. \tag{1.27}$$

Eq. 1.27 is the Hilbert transform of the derivative of the projection data. Inserting this equation in Eq. 1.20 gives the following reconstruction formula:

$$f(x,y) = \frac{1}{2\pi^2}\int_0^\pi\int_{-\infty}^{\infty}\frac{1}{l-t}\frac{dp_\theta(t)}{dt}dtd\theta = \frac{1}{2\pi}\int_0^\pi \mathcal{H}\left\{\frac{dp_\theta(l)}{dl}\right\}d\theta, \tag{1.28}$$

where $l = x\cos\theta + y\sin\theta$. This is the reconstruction formula for the Hilbert transform based FBP algorithm for parallel beam.

1.3.1.5 Filtered Back Projection algorithms for fan beam

The FBP algorithms described in the previous section, as well as the Fourier Slice Theorem, are only applicable to parallel beam data. For lab-based X-ray sources, a fan beam geometry is more realistic as 2D variant. To make reconstructions based on a fan beam geometry, the algorithms should be adapted. Since a part of this thesis is focussed on fan beam reconstruction algorithms, three FBP-like reconstruction algorithms for fan beam projection data are discussed in this section.

Rebinned FBP for fan beam In the first algorithm, the FBP is not directly applied on the measured projection data. Here, the projection data is converted

into parallel beam data. This is a process called *rebinning* and can be done by linear interpolation. After the rebinning, the parallel beam FBP can be applied on the rebinned projection data.

FBP algorithm for fan-beam data To perform the FBP on fan-beam data, a coordinate transformation should be applied. Assume that $p_\beta(s)$ is the measured projection data with β the angle between the central ray and the y-axis and s the coordinate along the detector axis. The parallel beam coordinates (l, θ) can then be expressed in terms of the fan-beam coordinates (s, β).

$$l = \frac{sD}{\sqrt{D^2 + s^2}}, \qquad \theta = \beta + \arctan(\frac{\mathrm{s}}{\mathrm{D}}). \tag{1.29}$$

Here, without loss of generality, a virtual detector in the origin is assumed and D is the distance from the source to the origin. The infinitesimal surface element then becomes:

$$dld\theta = \left(\frac{D}{\sqrt{s^2 + D^2}}\right)^3 dsd\beta. \tag{1.30}$$

Substituting this in Eq. 1.20 gives:

$$\begin{aligned} f(x,y) &= \frac{1}{2}\int_{-\arctan(\frac{s}{D^2})}^{2\pi-\arctan(\frac{s}{D^2})}\int_{-\infty}^{\infty} p_\beta(s) \times \left(\frac{D}{\sqrt{s^2+D^2}}\right)^3 \cdot \\ &\quad g(x\cos(\beta + \arctan(\frac{s}{D})) + y\sin(\beta + \arctan(\frac{s}{D})) - \frac{sD}{\sqrt{D^2+s^2}})dsd\beta. \end{aligned} \tag{1.31}$$

Eq. 1.31 can be simplified to Eq. 1.32. The steps to obtain the new equation can be found in [28].

$$f(x,y) = \frac{1}{2}\int_0^{2\pi}\int_{-\infty}^{\infty} p_\beta(s)\frac{s^2+D^2}{(D - x\sin\beta + y\cos\beta)^2} g(s'-s)\left(\frac{D}{\sqrt{s^2+D^2}}\right)^3 dsd\beta, \tag{1.32}$$

$$= \frac{1}{2}\int_0^{2\pi}\frac{1}{U^2}\int_{-\infty}^{\infty}\left(p_\beta(s)\frac{D}{\sqrt{s^2+D^2}}\right) g(s'-s)dsd\beta. \tag{1.33}$$

Here, s' is the detector pixel corresponding to the projection of pixel coordinate (x, y) at angle β and $U = {}^{D}/_{D - x\sin\beta + y\cos\beta}$. In conclusion, to perform the FBP on fan-beam projection data, three steps should be completed:

1. For each fan-beam projection $p_\beta(s)$, the corresponding modified projection

$p'_\beta(s)$ should be generated according to:

$$p'_\beta(s) = p_\beta(s)\frac{D}{\sqrt{s^2+D^2}}. \tag{1.34}$$

2. To generate the filtered projection, the modified projection is filtered by the inverse Fourier Transform of the ramp filter.

3. A weighted back projection with weight $1/U^2$ is performed along the fan-beam. The sum of the weighted back projections from all projection angles is the reconstruction image.

Hilbert transform based FBP algorithm for fan-beam data Also the Hilbert transform based FBP can be converted to a Hilbert transform based FBP reconstruction algorithm for fan-beam data as described in [30]. Using the same coordinates as in the FBP, the reconstruction equation for fan-beam data with a flat panel detector is given by:

$$f(x,y) = \frac{1}{4\pi}\int_0^{2\pi}\left[\left(\frac{\partial}{\partial s'}p_H(s',\beta)\frac{D^2+s'^2}{D} + \frac{\partial}{\partial\beta}p_H(s',\beta)\right)\times\frac{D^2+s'^2}{D^2}\right]d\theta, \tag{1.35}$$

where s' is the detector pixel corresponding to the projection of pixel coordinate (x,y) at angle β and $p_H(s',\beta)$ is the Hilbert transformed projection data [31]:

$$p_H(s',\beta) = \frac{D^2+s'^2}{\pi}\int_{-\infty}^{\infty}\frac{p_\beta(s)ds}{(s'-s)\sqrt{D^2+s^2}}. \tag{1.36}$$

Fig. 1.14 shows fan beam reconstructions of the Shepp-Logan phantom made with the different reconstruction algorithms discussed here. Both the rebinned FBP and the Hilbert transform based FBP suffer from interpolation artefacts. A fourth Heuristic Hilbert transform FBP is added. This algorithms does not suffer from interpolation artefacts since it avoids the interpolation in the algorithm. More information on the heuristic approach will be given in Chapter 3.

1.3.1.6 3D reconstruction methods

In the previous sections, 2D analytical reconstruction methods are discussed. An important next step is the extension towards 3D. For parallel beam data, the Radon transform and Fourier Slice Theorem are extensible to 3D and therefore a 3D Filtered Back Projection algorithm is available. For a circular cone beam geometry, the most common reconstruction algorithm is the *Feldkamp-Davis-Kress*

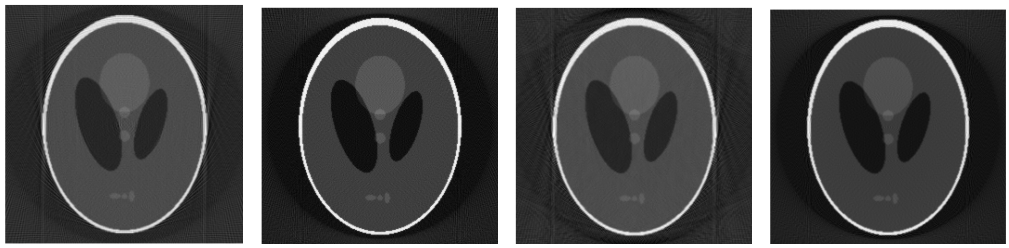

(a) (b) (c) (d)

Figure 1.14: Reconstructions of the Shepp-Logan phantom made with different fan beam reconstruction algorithms: **(a)** Rebinned FBP **(b)** FBP for fan beam **(c)** Hilbert transform based FBP **(d)** Heuristic Hilbert transform FBP

(FDK) algorithm[32]. This is an approximation of the exact reconstruction problem since the complete set of Radon data is not available in a circular cone beam geometry. As long as the angle aperture of the X-ray beam is small, the method yields acceptible results. Several variations of the algorithm exist. For helical cone beam CT, the complete set of Radon data is available which allows more accurate reconstruction algorithms. Several reconstruction algorithms are proposed by Kudo[33], Proksa[34] and Katsevich [35].

1.3.1.7 Prior knowledge based analytical reconstruction methods

Although incorporating prior knowledge into an analytical reconstruction algorithm is not straightforward, recent developments have succeeded to do so. Pelt et al [36, 37] introduced in 2013 the Neural Network based FBP algorithm. In this algorithm, several FBP reconstructions are combined. Their filters are trained in advance by a neural network. The NN-FBP algorithm is the basis for the inline NN-hFBP algorithm introduced in Chapter 3. In another algorithm, also by Pelt, the filter of FBP is constructed in such a way that the final reconstruction image approximates a SIRT reconstruction [38].

1.3.2 Algebraic reconstruction methods

Algebraic reconstruction methods are divided into two groups: Landweber methods and Krylov subspace methods. In this section, examples of both groups are explained. First, in Section 1.3.2.1, the discrete projection model used in algebraic reconstruction methods is discussed. Then a Landweber reconstruction method, the Simultaneous Iterative Reconstruction Technique is described in Sec-

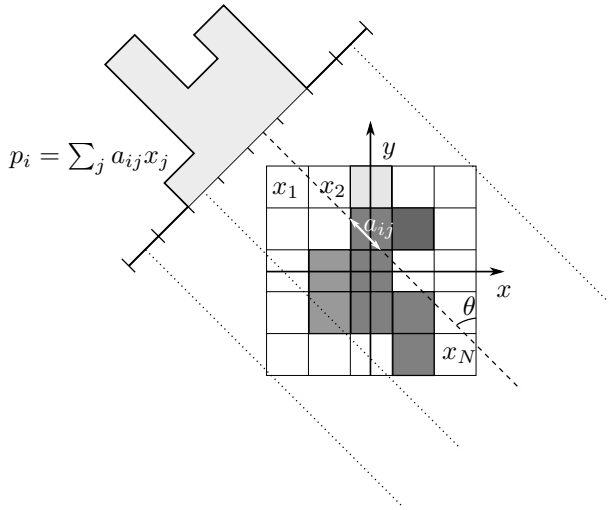

Figure 1.15: The Discrete Projection Model

tion 1.3.2.2 and a Krylov subspace based reconstruction method, the Conjugate Gradient Least Squares (CGLS) in Section 1.3.2.3. This subsection ends with some algebraic reconstruction methods that are based on prior knowledge. Common about algebraic reconstruction methods is that it is possible to exploit prior knowledge in the form of some constraints. Moreover, the methods are very flexible, allowing scan geometries that deviate from the conventional circular or helical scan geometry. The drawback of these methods is that they often come with a high computation cost.

1.3.2.1 Discrete projection model

In algebraic reconstruction methods, the reconstructed image is often represented on a grid by a certain number of pixels or voxels N with a non-zero volume and the projection data is represented by a number of pixels M with a certain width and height. A discretized version of the Radon Transform can then be obtained:

$$\begin{array}{rcl} p_i & = & \displaystyle\sum_{j=1}^{N} a_{i,j} x_j, \\ \updownarrow & & \updownarrow \ \updownarrow \\ p_\beta(s) = & & \mathcal{R}\{f(x,y))\}, \end{array} \tag{1.37}$$

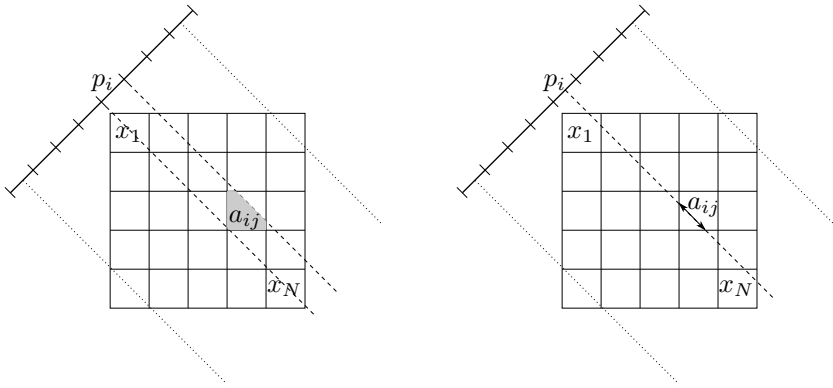

(a) Line Kernel **(b)** Strip Kernel

Figure 1.16: Illustration of two kernels that can be used to calculate the projection data in the discrete projection model

where $a_{i,j}$ is the contribution of the pixel or voxel x_j to the detector pixel p_i. An illustration of this projection model is shown in Fig. 1.15. More general, the projection data as well as the reconstruction data are represented as columnvectors $\mathbf{p} = (\mathbf{p_i}) \in \mathbb{R}^{\mathbf{M}\times\mathbf{1}}$ and $\mathbf{x} = (\mathbf{x_i}) \in \mathbb{R}^{\mathbf{N}\times\mathbf{1}}$ respectively and a *system matrix* $\mathbf{A} = (a_{i,j}) \in \mathbb{R}^{N\times M}$ contains the contributions of all the voxels to the projection data. The acquisition process can therefore be modelled as a system of linear equations written in matrix form:

$$\mathbf{p} = \mathbf{A}\mathbf{x}. \tag{1.38}$$

The system matrix $\mathbf{A}$ is a sparse matrix and it is almost singular. The matrix can be calculated in several ways. In a strip-kernel projection model, shown in Fig. 1.16a, the weight $a_{i,j}$ is calculated as the area of pixel j illuminated by ray i divided by the total area of pixel j. Its value is always between 0 and 1. A less computationally expensive model is a line-kernel where the weight is determined by the length of a single line passing though pixel j [39]. This kernel is shown in Fig. 1.16b. A third way to model the system matrix is by a linear kernel, known as Joseph's method [40]. In Joseph's method, the weights are calculated by linear interpolating between the two nearest pixels of the intersection of the ray and the row or column. The reconstruction image x does not necessarily need to be a pixel based function. It can also be defined as a set of radial basis functions such as the modified Kaiser-Bessel window [41].

In computed tomography, one's goal is to retrieve $\mathbf{x}$, knowing $\mathbf{p}$ and $\mathbf{A}$. However, the inverse of $\mathbf{A}$ almost never exists and the system of equations is polluted with noise and discretization effects. Therefore, in algebraic reconstruction algorithms,

the reconstruction image is often optimized by minimizing the *projection distance* $\|\mathbf{Ax}-\mathbf{p}\|$ for some norm $\|\cdot\|$. Various iterative methods exist that try to solve this minimization problem. One of them is the Simultaneous Iterative Reconstruction Technique (SIRT), which will be discussed in the next section.

1.3.2.2 Simultaneous Iterative Reconstruction Technique (SIRT)

The SIRT algorithm iteratively updates an initial reconstruction according to the following update step [28, 42]:

$$\boldsymbol{x}^{(k+1)} = \boldsymbol{x}^{(k)} + \boldsymbol{C}\boldsymbol{A}^T\boldsymbol{R}(\boldsymbol{p} - \boldsymbol{A}\boldsymbol{x}^{(k)}). \tag{1.39}$$

Let us look at the different parts of the equation individually. Assume $\boldsymbol{x}^{(0)} = \mathbf{0}$ is the initial estimate of the reconstruction and k is the number of iterations.

1. In the first step of the algorithm, a forward projection $\boldsymbol{A}\boldsymbol{x}^{(k)}$ is taken of the current estimate of the reconstruction.
2. Secondly, the projection difference is calculated: $\boldsymbol{r}^{(k)} = \boldsymbol{p} - \boldsymbol{A}\boldsymbol{x}^{(k)}$.
3. Then, an update value is obtained by weighting the projection difference with the inverse row sums, back projecting or 'smearing out' this weighted projection difference on the reconstruction grid and finally weighting the update value with the inverse column sums.

   $$\boldsymbol{u}^{(k)} = \boldsymbol{C}\boldsymbol{A}^T\boldsymbol{R}(\boldsymbol{p} - \boldsymbol{A}\boldsymbol{x}^{(k)}). \tag{1.40}$$

   $\boldsymbol{R}$ and $\boldsymbol{C}$ are diagonal matrices containing the inverse row sums and column sums of the matrix $\boldsymbol{A}$, i.e. $r_{ii} = {}^1\!/_{\sum_j a_{ij}}$ and $c_{jj} = {}^1\!/_{\sum_i a_{ij}}$.
4. Finaly the update step is added to the reconstruction of the previous iteration to obtain the current reconstruction image: $\boldsymbol{x}^{(k+1)} = \boldsymbol{x}^{(k)} + \boldsymbol{u}^{(k)}$.

The stopping criteria for the algorithm is often either a pre-set number of iterations or a threshold value for the projection difference. A schematic of the different SIRT steps is given in Fig. 1.17. The full update step of SIRT for each iteration and each component is given by:

$$x_j^{(k+1)} = x_j^{(k)} + \frac{1}{\sum_{i=1}^{M} a_{ij}} \sum_{i=1}^{M} \left(\frac{a_{ij}(p_i - \sum_{h=1}^{N} a_{ih} x_h^{(k)})}{\sum_{h=1}^{N} a_{ih}} \right). \tag{1.41}$$

It can be proven that SIRT converges and that its reconstruction is the optimal solution for the weighted least-squares optimization problem:

$$\arg\min_{\boldsymbol{x}} \|\boldsymbol{A}\boldsymbol{x} - \boldsymbol{p}\|_{\boldsymbol{R}}, \tag{1.42}$$

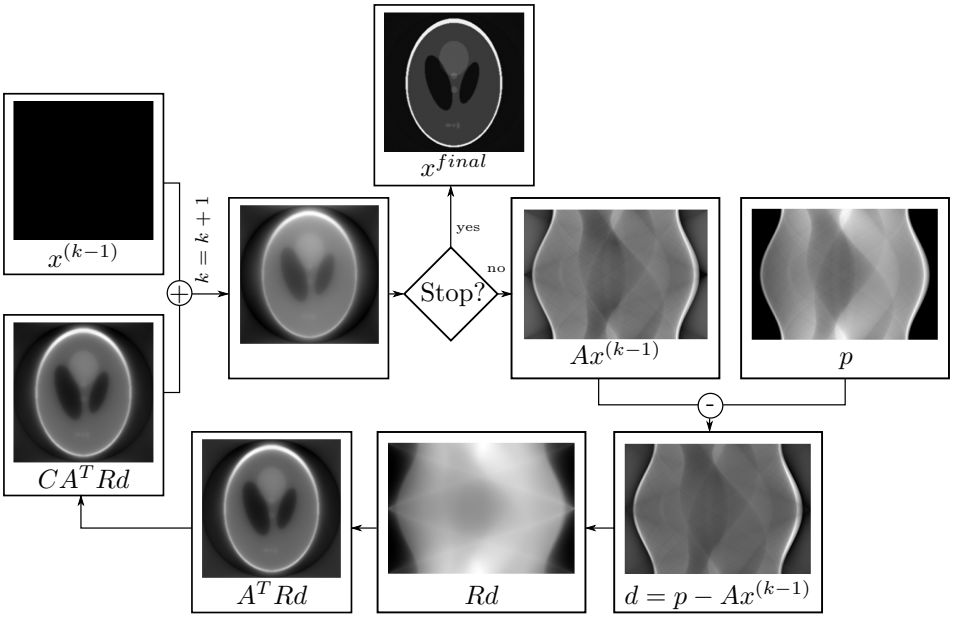

Figure 1.17: A reconstruction scheme for the SIRT algorithm.

where $\|\boldsymbol{Ax} - \boldsymbol{p}\|_{\boldsymbol{R}} = (\boldsymbol{Ax} - \boldsymbol{p})^T \boldsymbol{R}(\boldsymbol{Ax} - \boldsymbol{p})$.

In each SIRT iteration, all projection data from each projection direction is taken into account. Two other reconstruction algorithms, the *algebraic reconstruction technique (ART)* [43] and the *Simultaneous Algebraic Reconstruction Technique (SART)* [44] follow a similar reconstruction scheme as SIRT, but do not incorporate all projection data for each iteration. In ART only one single projection value is processed during an iteration and in SART, all projection data from one projection direction is used. ART typically needs less iterations over the complete projection data than SIRT to converge to a solution, but the algorithm is less stable with respect to noise. SART tries to profit from both ART and SIRT: obtaining a stable optimal solution with fewer iterations. The order in which the projection data is processed in ART and SART has however an important influence on the final reconstruction quality [45].

1.3.2.3 Conjugate Gradient Least Squares (CGLS)

Conjugate Gradient Least Squares (CGLS) [46] is a Krylov Subspace iterative reconstruction method. It performs an iterative Conjugate Gradient (CG) algorithm

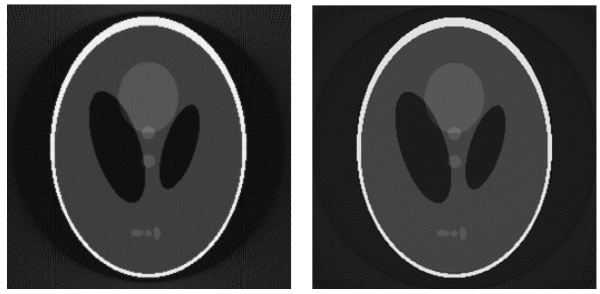

(a) (b)

Figure 1.18: A (a) SIRT and (b) CG reconstruction of the Shepp-Logan phantom made with 200 and 30 iterations respectively over 180 degrees.

to solve the least squares problem

$$x^* = arg\min_x(\|\boldsymbol{A^T A x - A^T p}\|_2^2). \tag{1.43}$$

The method converges to a possible solution much faster than SIRT. Assume $\boldsymbol{r}^0 = \boldsymbol{p}^0$, $\boldsymbol{z}^0 = \boldsymbol{A}^T\boldsymbol{p}$ and $\boldsymbol{x}^0 = \boldsymbol{A}^T\boldsymbol{p}$, the algorithm then exists of three steps that are executed in each iteration:

$$\boldsymbol{r}^{(k+1)} = \boldsymbol{r}^{(k)} - \frac{\|\boldsymbol{z}^{(k)}\|_2}{\|\boldsymbol{A x}^{(k)}\|_2}\boldsymbol{A x}^{(k)}, \tag{1.44}$$

$$\boldsymbol{z}^{(k+1)} = \boldsymbol{A}^T\boldsymbol{r}^{(k+1)}, \tag{1.45}$$

$$\boldsymbol{x}^{(k+1)} = \boldsymbol{z}^{(k+1)} + \frac{\|\boldsymbol{z}^{(k+1)}\|_2}{\|\boldsymbol{z}^{(k)}\|_2}\boldsymbol{x}^{(k)}. \tag{1.46}$$

A comparison of a SIRT reconstruction with 200 iterations and a CGLS reconstruction with 30 iterations of the Shepp-Logan phantom is shown in Fig. 1.18.

1.3.2.4 Prior knowledge-based algebraic reconstruction methods

Prior knowledge can be incorporated in a reconstruction algorithm to improve the final reconstructed image. One way of incorporating prior knowledge is by means of a regularization term R in the optimization problem and a regularization parameter $\lambda > 0$ that controls the strength of the regularization.

$$x^* = arg\min_x(\|\boldsymbol{A x - p}\| + \lambda R(x)). \tag{1.47}$$

Typically, prior knowledge imposed by the regularization term is a smoothness [47, 48], total variation [49], non-negativity [48] or non-local means [50] constraint. Another way to incorporate prior knowledge in the reconstruction is by applying an advanced reconstruction algorithm that is designed only for specific applications. An advanced algorithm in the field of discrete tomography is the *Discrete Algebraic Reconstruction Technique (DART)* [51], which deals with the reconstruction of samples that exist of only a few discrete grey levels. When conventional reconstructions are tempered by metal artefacts, special algorithms like the *Normalized Metal Artefact Reduction (NMAR)*[52] algorithm exist to reduce the artefacts caused by the metal. And in dynamic CT, where object motion is present during the scans, specific algorithms exist like the MoVIT algorithm [53]. Some other examples are algorithms for porous samples [54] and for Region of Interest (ROI) [55] tomography. In the latter, a useful approach is to adapt the projection model to a continuous gantry rotation [56].

1.3.3 Statistical reconstruction methods

Statistical reconstruction algorithms try to estimate the solution that maximizes the likelihood of observing the measured projections, while taking into account the statistical processes at the source, object and detector. It is the best choice in case of a low photon count and a high amount of noise. Statistical reconstruction algorithms are also good in reducing beam hardening artefacts since they take the polychromaticity of the source into account. In general, the data is often modelled by a Poisson distribution and several reconstruction algorithms exist like the maximum likelihood expectation maximization (ML-EM) algorithm [57], the ordered subset convex algorithm, [58, 59] and the iterative coordinate descent algorithm [60]. A drawback of these methods is that the polychromatic spectrum of the source is assumed to be prior knowledge and long computation times are needed.

1.4 Applications of transmission X-ray CT

In this section, an overview is given of the different fields in which CT has applications.

- **Medical Imaging** A CT scanner is best known in a medical context. For years, CT scanners have been used to imagine various parts of the human body. To aid the medical diagnosis, abdominal [61], dental [62], cerebral [63], pulmonary [64] and cardiac [65] imaging amongst others are performed. To improve the contrast in the image, contrast fluids are sometimes used [66].

Apart from helping to obtain a diagnosis, X-ray imaging can also be used to guide surgery [67] or as a radiation therapy [68].

- **Biomedical Imaging** A μ-CT scanner for small animal scanning is used in biomedical research to test the effect of various drugs and diseases on rats and mice [69, 70, 71]. In this scanners a trade-off should be made between the spatial resolution, the radiation dose and the time between consecutive scans.

- **Material Science** To inspect the properties of materials, not only μ-CT systems are used, but materials are often inspected with an electron microscope [72, 73] or at a synchrotron facility. Due to this imaging modalities, much process is made in the discovery, study and design of materials [74].

- **Inspection** Inspecting the interior of objects is an important part of X-ray tomography. Two important applications are food inspection [23, 75, 76] and luggage inspection [77, 78]. In the first, the quality of food is inspected before it is sold to assure delivery of good quality products. In the latter, baggage is scanned at the airport for example to check for dangerous goods. Furthermore, also metrology is a type of inspection where the sizes of materials are measured with CT to check the manufacturing process [79, 80].

- **Others** On a much larger scale, CT is used to reconstruct waves of earthquakes [81] or the corona of the sun [82].

References

[1] W. C. Röntgen, "Über eine neue art von strahlen.," *Sonderdruck aus den Sitzungsberichten der Wuzburger Physik.-medic.Gesellschaft*, 1896.

[2] O. Glasser, *Wilhelm Conrad Röntgen and the early history of the roentgen rays.* Norman Publishing, 1993.

[3] B. Kevles, *Naked To The Bone:Medical Imaging In The Twentieth Century.* Rutgers University Press, 1997.

[4] J. Radon, "Über die Bestimmung von Funktionen durch ihre Integralwerte längs gewisser Mannigfaltigkeiten.," *Berichte über die Verhandlungen der Königlich-Sächsischen Akademie der Wissenschaften zu Leipzig, Mathematisch-Physische Klasse*, no. 69, pp. 262–227, 1917.

[5] D. Pickens, R. Price, J. A. Patton, J. Erickson, F. Rollo, and A. Brill, "Focal-Plane Tomography Image Reconstruction," *IEEE Transactions on Nuclear Science*, vol. 27, no. 1, pp. 489–492, 1980.

[6] A. Cormack, "Representation of a Function by Its Line Integrals, with Some Radiological Applications," *Journal of Applied Physics*, vol. 34, no. 2722, 1963.

[7] A. Cormack, "Representation of a Function by Its Line Integrals, with Some Radiological Applications. II," *Journal of Applied Physics*, vol. 35, no. 2902, 1964.

[8] P. Wells, "Sir Godfrey Newbold Hounsfield KT CBE. 28 August 1919 12 August 2004 Elected F.R.S. 1975," *Biographical Memoirs of Fellows of the Royal Society*, vol. 51, pp. 221–235, 2005.

[9] J. Prince and J. Links, *Medical Imaging Signals and Systems*. Pearson Prentice Hall, 2006.

[10] W. Hendee and E. Ritenour, *Medical Imaging Physics*. Wiley-Liss, 2002.

[11] A. Balerna and S. Mobilio, *Introduction to Synchrotron Radiation*, vol. 3, ch. 1, pp. 3–28. Springer, 2015.

[12] W. Coolidge, "Vacuum-tube," 05 1913.

[13] D. Grider, A. Wright, and P. Ausburn, "Electron beam melting in microfocus x-ray tubes," *J. Phys. D:Appl. Phys.*, vol. 19, pp. 2281–2292, 1986.

[14] O. Hemberg, M. Otendal, and H. Hertz, "Liquid-metal-jet anode electron-impact X-ray source," *Applied Physics Letters*, vol. 83, no. 7, pp. 1483–1485, 2003.

[15] M. Otendal, T. Tuohimaa, U. Vogt, and H. Hertz, "A 9 keV electron-impact liquid-gallium-jet X-ray source," *Rev. Sci. Instrum.*, vol. 79, p. 016102, 2008.

[16] R. Tucoulou, G. Martinez-Criado, P. Bleuet, I. Kieffer, P. Cloetens, S. Labouré, T. Martin, C. Guilloud, and J. Susini, "High-resolution angular beam stability monitoring at a nanofocusing beamline," *J. Synchrotron Radiat.*, vol. 15, pp. 392–398, 2008.

[17] J. Hubbell, "Electron-positron pair production by photons: A historical overview," *Radiation Physics and Chemistry*, vol. 75, no. 6, pp. 614–623, 2006.

[18] S. Benjamin, "Phosphor plate radiography: an integral component of the filmless practice.," *Dent Today*, vol. 29, no. 11, p. 89, 2010.

[19] M. Yaffe and J. Rowlands, "X-ray detectors for digital radiography," *Physics in Medicine & Biology*, vol. 42, no. 1, 1997.

[20] H. Chotas, J. Dobbins, and C. Ravin, "Principles of Digital Radiography with Large-Area, Electronically Readable Detectors: A Review of the Basics," *Radiology*, vol. 210, no. 3, pp. 595–599, 1998.

[21] E. Lee and H. Kim, "Early Fatigue Failures of Cemented, Forged Cobalt-Chromium Femoral Stems at the Neck-Shoulder Junction," *The journal of Arthroplasty*, vol. 16, no. 2, pp. 236–238, 2001.

[22] A. Nayfeh, T. Kassim, N. Addasi, F. Alghoula, C. Holewinski, and Z. Depew, "A challenging Case of Acute Mercury Toxicity," *Case Reports in Medicine*, vol. 2018, 2018.

[23] R. P. Haff and N. Toyofuku, "X-ray detection of defects and contaminants in the food industry," *Sensing and Instrumentation for Food Quality and Safety*, vol. 2, no. 4, pp. 262–273, 2008.

[24] D. Schumacher, K. Antin, U. Zscherpel, and P. Vilaca, "Application of Different X-ray Techniques to Improve In-Service Carbon Fiber Reinforced Rope Inspection," *J Nondestruct Eval*, vol. 36, no. 62, 2017.

[25] J. Radon, "On the determination of functions from their integral values along certain manifolds," *IEEE Trans. Med. Imag.*, vol. 5, pp. 170–176, 1986.

[26] L. Shepp and B. Logan, "The Fourier reconstruction of a head section," *IEEE Transactions on Nuclear Science*, vol. 21, pp. 21–43, 1974.

[27] A. Kak and M. Slaney, *Principles of Computerized Tomographic Imaging*. IEEE Press, 1988.

[28] T. Buzug, *Computed Tomography: From Photon Statistics to Modersn Cone-Beam CT*. Springer-Verslag Berlin Heidelberg, 2008.

[29] M. Heideman, D. Johnson, and C. Burrus, "Gauss and the history of the fast fourier transform," *ASSP Magazine, IEEE,*, vol. 1, pp. 14–21, 1984.

[30] A. Narasimhadhan and K. Rajgopal, "FDK-Type algorithms with No Backprojection Weight for Circular and Helical Scan CT," *International Journal of Biomedical Imaging*, vol. 2012, 2012.

[31] J. You, G. Zeng, and Z. Liang, "FBP Algorithms for Attenuated Fan-Beam Projections," *Inverse Problems*, vol. 21, no. 5, 2005.

[32] L. Feldkamp, L. Davis, and J. Kress, "Practical cone-beam algorithm," *Journal of Optical Society of America*, vol. 1, pp. 612–619, 1984.

[33] H. Kudo, T. Rodet, F. Noo, and M. Defrise, "Exact and approximate algorithms for helical cone-beam ct," *Physics in Medicine and Biology*, vol. 49, no. 13, pp. 2913–2931, 2004.

[34] R. Proksa, T. Köhler, M. Grass, and J. Timmer, "The n-Pi-method for helical cone-beam CT," *IEEE Trans Med Imaging*, vol. 19, no. 9, pp. 848–63, 2000.

[35] A. Katsevich, "Analysis of an exact inversion algorithm for spiral cone-beam ct," *Physics in Medicine and Biology*, vol. 43, no. 15, pp. 2583–2597, 2002.

[36] D. M. Pelt, J. Sijbers, and K. J. Batenburg, "Fast tomographic reconstruction from highly limited data using artificial neural networks," in *1st International Conference on Tomography of Materials and Structures*, pp. 109–112, 2013.

[37] D. M. Pelt and K. J. Batenburg, "Fast Tomographic Reconstruction from Limited Data Using Artificial Neural Networks," *IEEE Trans Image Process*, vol. 22, no. 12, pp. 5238–5251, 2013.

[38] D. M. Pelt and K. J. Batenburg, "Accurately approximating algebraic tomographic reconstruction by filtered backprojection," in *Proceedings of International Meeting on Fully Three-Dimensional Image Reconstruction in Radiology and Nuclear Medicine*, pp. 158–161, 2015.

[39] R. Siddon, "Fast calculation of the exact radiological path for a three-dimensional CT array," *Medical Physics*, vol. 12, no. 2, pp. 252–255, 1985.

[40] P. Joseph, "An improved algorithm for reprojecting rays through pixel images," *IEEE Transactions on Medical Imaging*, vol. 1, no. 3, pp. 192–196, 1982.

[41] R. Lewitt, "Alternatives to voxels for image representation in iterative reconstruction algorithms," *Physics in Medicine and Biology*, vol. 37, no. 3, pp. 705–716, 1992.

[42] J. Gregor and T. Benson, "Computational analysis and improvement of SIRT," *IEEE Trans. Med. Imaging*, vol. 27, pp. 918–924, 2008.

[43] R. Gordon, R. Bender, and G. Herman, "Algebraic Reconstruction Techniques (ART) for three-dimensional electron microscopy and X-ray photography," *Journal of Theoretical Biology*, vol. 29, no. 3, pp. 471–481, 1970.

[44] A. Andersen and A. Kak, "Simultaneous algebraic reconstruction technique (SART): a superior implementation of the ART algorithm," *Ultrasonic Imaging*, vol. 6, no. 1, pp. 81–94, 1984.

[45] H. Guan and R. Gordon, "Computed tomography using algebraic reconstruction techniques (ARTs) with different projection access schemes: a comparison study under practical situations," *Physics in Medicine and Biology*, vol. 41, no. 9, p. 1727, 1996.

[46] C. Paige and M. Saunders, "LSQR: An algorithm for sparse linear equations and sparse least squares," *ACM Transactions on Mathematical Software*, vol. 8, pp. 43–71, 1982.

[47] J. Tang, B. Nett, and G. Chen, "Performance comparison between total variation (TV)-based compressed sensing and statistical iterative reconstruction algorithms," *Physics in Medicine and Biology*, vol. 54, no. 19, p. 5781, 2009.

[48] X. Zhang, J. Wang, and L. Xing, "Metal artifact reduction in X-ray computed tomography (CT) by constrained optimization," *Medical Physics*, vol. 38, no. 2, pp. 701–711, 2011.

[49] T. Wang, K. Nakamoto, H. Zhang, and H. Liu, "Reweighted Anisotropic Total Variation Minimization for Limited-Angle CT Reconstruction," *IEEE Transactions on Nuclear Science*, vol. 64, no. 10, pp. 2742–2760, 2017.

[50] Y. Zhang, H. Lu, J. Rong, J. Meng, J. Shang, P. Ren, and J. Zhang, "Adaptive non-local means on local principle neighborhood for noise/artifacts reduction in low-dose CT images.," *Medical Physics*, vol. 44, no. 9, pp. e230–e241, 2017.

[51] K. Batenburg and J. Sijbers, "DART: A practical reconstruction algorithm for discrete tomography.," *IEEE Transactions on Image Processing*, vol. 20, no. 9, pp. 2542–2553, 2011.

[52] E. Meyer, R. Raupach, M. Lell, B. Schmidt, and M. Kachelriess, "Normalized metal artifact reduction (NMAR) in computed tomography," *Medical Physics*, vol. 37, no. 10, pp. 5482–93, 2010.

[53] V. Van Nieuwenhove, J. De Beenhouwer, J. Vlassenbroeck, M. Brennan, and J. Sijbers, "MoVIT: A tomographic reconstruction framework for 4D-CT," *Optics Express*, vol. 25, no. 16, pp. 19236–19250, 2017.

[54] G. Van Eyndhoven, M. Kurttepeli, C. Van Oers, P. Cool, S. Bals, K. Batenburg, and J. Sijbers, "Pore Reconstruction and Segmentation (PORES) method for improved porosity quantification of nanoporous materials," *Ultramicroscopy*, vol. 148, pp. 10–19, 2015.

[55] E. Sidky, D. Draemer, E. Roth, C. Ullberg, I. Reiser, and X. Pan, "Analysis of iterative region-of-interest image reconstruction for X-ray computed tomography," *Journal of Medical Imaging*, vol. 1, no. 3, p. 031007, 2014.

[56] J. Cant, W. Palenstijn, G. Behiels, and J. Sijbers, "Modeling blurring effects due to continuous gantry rotation: application to region of interest tomography," *Medical Physics*, vol. 42, no. 5, pp. 2709–2717, 2015.

[57] K. Lange and R. Carson, "EM reconstruction algorithms for emission and transmission tomography," *J. Comput. Assist. Tomogr.*, vol. 8, pp. 306–16, 1984.

[58] C. Kamphuis and F. Beekman, "Accelerated iterative transmission CT reconstruction using an orderen subsets convex algorithm," *IEEE Trans Med Imaging*, vol. 17, pp. 1101–5, 1998.

[59] F. Beekman and C. Kamphuis, "Ordered subset reconstruction for x-ray CT," *Phys Med Biol*, vol. 46, pp. 2835–44, 2001.

[60] C. Bouman and K. Sauer, "A unified approach to statistical tomography using coordinate descent optimization," *IEEE Trans Image Process*, vol. 5, pp. 480–92, 1996.

[61] S. Jackman, S. Potter, F. Regan, and T. Jarrett, "Plain abdominal X-ray versus computerized tomography screeing: sensitivity for stone localization after nonenhanced spiral computerized tomography," *The Journal of Urology*, vol. 164, pp. 308–310, 2000.

[62] J. Na'am, "Accuracy of Panoramic Dental X-ray Imaging in Detection of Proximal Caries with Multiple Morpological Gradient (mMG) Method ," *International Journal on Informatics Visualization*, vol. 1, no. 1, pp. 5–11, 2017.

[63] X. Liu, L. Chen, W. Qi, Y. Jiang, Y. Liu, M. Zhang, and N. Hong, "Thin-slice brain CT with iterative model reconstruction algorithm for small lacunar lesions detection," *Medicine*, vol. 96, no. 51, p. e9412, 2017.

[64] H. Kappauf and G. Esser, "Metachronous Spontaneous Remission of Melanoma Lung Metastasis and Mediastinal Lymph Node Metastases," *Oncol Res Treat*, vol. 41, no. 3, pp. 135–138, 2018.

[65] M. J. Budoff and J. S. Shinbane, *Cardiac CT imaging: diagnosis of cardiovascular disease*. Springer International Publishing, 2016.

[66] P. Dahlman, E. Semenas, E. Brekkan, A. Bergman, and A. Magnusson, "Detection and characterisation of renal lesions by multiphasic helical CT," *Acta Radiologica*, vol. 41, pp. 361–366, 2000.

[67] T. Peters, "Image-guided surgery: from X-rays to virtual reality," *Comput Methods Biomech Biomed Engin*, vol. 4, no. 1, pp. 27–57, 2000.

[68] H. Chen, G. Wang, Y. Chuang, Z. Zhen, X. Chen, P. Biddinger, Z. Hao, F. Liu, B. Shen, Z. Pan, and J. Xie, "Nanoscintillator-Mediated X-ray Inducible Photodynamic Therapy for In Vivo Cancer Treatment," *Nano Lett.*, vol. 15, no. 4, pp. 2249–2256, 2015.

[69] N. Ford, L. McCaig, A. Jeklin, J. Lewis, R. Veldhuizen, D. Holdsworth, and M. Drangova, "A respiratory-gated micro-CT co,parison of respiratory patterns in free-breathing and mechanically ventilated rats," *Physiological Reports*, vol. 5, no. e13074, 2017.

[70] J. Ashton, N. Befera, D. Clark, Y. Qi, L. Mao, H. Rockman, G. Allan Johnson, and C. Badea, "Anatomical and functional imaging of myocardial infarction in mice using micro-CT and eXIA 160 contrast agent," *Contrast Media & Molecular imaging*, vol. 9, no. 2, pp. 161–168, 2014.

[71] H. Dähring, J. Grandke, U. Teichgräber, and I. Hilger, "Improved Hyperthermia Treatment of Tumors Under Consideration of Magnetic Nanoparticle Distribution Using Micro-CT Imaging," *Molecular Imaging and Biology*, vol. 17, no. 6, pp. 763–769, 2015.

[72] P. Ercius, O. Alaidi, M. Rames, and G. Ren, "Electron Tomography: A Three-Dimensional Analytic Tool for Hard and Soft Materials Research," *Adv Mater*, vol. 27, no. 38, pp. 5638–5663, 2016.

[73] P. Midgley and R. Dunin-Borkowski, "Electron tomography and holography in materials science," *Nature Materials*, vol. 8, pp. 271–280, 2009.

[74] J. Banhart, *Advanced tomographic methods in materials research and engineering*. Oxford University Press New York, 2008.

[75] M. Van Dael, S. Lebotsa, E. Herremans, P. Verboven, J. Sijbers, U. Opara, P. Cronje, and B. Nicolaï, "A segmentation and classification algorithm, for online detection of internal disorders in citrus using X-ray radiographs," *Postharvest Biol Technol*, vol. 112, pp. 205–14, 2016.

[76] N. Kotwaliwale, K. Singh, A. Kalne, N. Narayan Jha, N. Seth, and A. Kar, "X-ray imaging methods for internal quality evaluation of agricultural produce," *Journal of Food Science and Technology*, vol. 51, no. 1, pp. 1–15, 2014.

[77] I. Uroukov and R. Speller, "A preliminary approach to intelligent X-ray imaging for baggage inspection at airports," *Signal Process*, vol. 4, pp. 1–11, 2015.

[78] P. Jin, E. Haneda, K. Sauer, and C. A. Bouman, "A model-based 3D multi-slice helical CT reconstruction algorithm for transportation security application," in *Second International Conference on Image Formation in X-Ray Computed Tomography, Salt Lake City, Utah, USA*, 2012.

[79] J. Warnet, V. Titarenko, E. Kiraci, A. Attridge, W. Lionheart, P. Withers, and M. Willems, "Towards in-process X-ray CT for dimensional metrology," *Measurement Science and Technology*, vol. 27, no. 3, p. 035401, 2016.

[80] J. Kruth, M. Bartscher, S. Carmignato, R. Schmitt, L. De Chiffre, and A. Weckenmann, "Computed tomography for dimensional metrology," *CIRP Annals - Manufacturing Technology*, vol. 60, no. 2, pp. 821–842, 2011.

[81] G. Nolet, *Seismic tomography: zith applications in global seismology and exploration geophysics*, vol. 5. Springer Science & Business Media, 2012.

[82] M. Butala, R. Hewett, R. Frazin, and F. Kamalabadi, "Dynamic three-dimensional tomography of the solar corona," *Solar Physics*, vol. 262, no. 2, pp. 495–509, 2010.

2

Phase Contrast X-ray Imaging

Contents

In the previous chapter, a brief introduction to transmission X-ray imaging was given. As discussed, X-rays can be used to inspect the spatial distribution of materials inside an object in a non-destructive way by acquiring several projections from various projection directions, and combining them into one image by the use of a reconstruction algorithm. A major disadvantage of transmission X-ray image is however that the variations in the linear attenuation coefficients of soft tissues are very small. As a result, soft tissues and other materials with similar linear attenuation coefficients cannot be well separated in the reconstruction. In recent years, a new type of X-ray imaging, namely Phase Contrast Computed Tomography (PCCT) has been developed. In PCCT, not only the linear attenuation coefficient caused by the decrease in intensity of the X-rays is reconstructed, but also the phase shift induced when an X-ray beam passes through material. This phase shift is linked to the real part of the refractive index of a material and is much more sensitive than the linear attenuation coefficient. Therefore, it allows to distinguish materials that are not distinguishable in transmission CT. Furthermore, PCCT also provides information on the scattering that occurs inside a sample.
In this chapter, a brief overview of PCCT will be given. In Section 2.1, different imaging methods are discussed that all provide phase contrast data to the user. Then, in Section 2.2, one of these imaging methods is studied more into detail. Finally in the last section, PCCT tomographic reconstruction methods are discussed.

2.1 Phase Contrast Imaging Methods

In this section, a closer look is taken at the five major imaging modalities that are commonly used to obtain information about the phase-shift of the X-rays induced by the sample.

2.1.1 Crystal Interferometry

Bonse and Hart [1, 2] published the design of the first three-crystal X-ray interferometer in 1965. In this interferometer, three beam splitting crystals are aligned parallel to eachother. Fig. 2.1a shows a schematic of the interferometer. The first crystal splits the beam in two coherent X-ray beams. The second crystal causes the beams to converge again. One of the two beams then passes through a sample while the other one remains unchanged. The two beams come together at the third crystal where an interference pattern arises. The pattern is measured at a detector behind the third crystal. With the interferometer, both an absorption and a phase signal can be measured. Particular about the crystal interferometer is the direct

measurement of the phase, opposed to the derivative measurements in the other modalities. Later in 2003, Momose [3] showed the possibility of tomography with this setup. The largest constraints of the method are its spatial resolution, the need for a very stable setup and the high flux dependency. The low spatial resolution is caused by the blurring of the beam in the last crystal [4]. To obtain an interference pattern at the third crystal, the difference in path length between the two beams should be smaller than the wavelength of the X-rays. Therefore the alignment of the crystals should be very precise. To achieve the required precision, the beam splitter crystals are often cut out of one big crystal. This, however, clearly limits the field of view and the size of the sample that can be scanned[5]. Furthermore, the crystals filter a large part of the radiation, which means that a long exposure time or a high photon flux is necessary to acquire images with a sufficient SNR. For this reason, crystal interferometers are often used at a synchrotron source where this condition is met.

2.1.2 Analyzer based Imaging

In analyzer based imaging (ABI) or diffraction enhanced imaging (DEI) [6, 7, 8], a parallel X-ray beam is generated by a monochromator. This X-ray beam passes through a sample and hits an analyzer crystal which acts as an angular filter by reflecting part of the beam onto a detector (Fig. 2.1b). Only the X-rays with an incident angle for which the Bragg diffraction condition [9] is fulfilled are reflected on the detector. By rotating the crystal, X-rays from a range of incident angles are measured. Starting from several images obtained with different rotation angles of the crystal, a rocking curve can be constructed. A rocking curve describes the relation between the intensity of the reflected rays and the incident angles. Placing a sample in the setup will cause a shift in the rocking curve, from which the first derivative of the phase can be derived, whereas a dark-field image can be constructed from the variations in the shape of the rocking curve [10, 11]. ABI has a high phase sensitivity and it requires good stability of the crystals, although the reconstruction quality depends less on the stability of the crystal than in crystal interferometry. The technique can be used for tomography, but only the component of the phase parallel to the tomographic axis is detected. Due to its high phase sensitivity, ABI is especially of interest for soft tissue imaging and is already used for example in mammography for detection of microcalcifications [12].

2.1.3 Propagation based Imaging

The simplest kind of phase contrast imaging was invented by Snigirev in [13] and is called propagation based imaging. This method relies on the appearance of Fresnel fringes in the diffraction pattern due to free space propagation of the wave after

passing through the sample. Therefore, no extra hardware is necessary to obtain information about the phase of the object. The only requirement is an increase in the distance between the object and the detector. The pattern of the fringes that appear at the detector is related to the Laplacian of the phase [14]. By obtaining images at several object-detector distances, the phase can be derived. [15]. A schematic of the setup with a moving detector is given in Fig. 2.1c. Limitations of the method are that a high spatial coherence of the beam is necessary and that the detector needs to have a high resolution to detect subtle changes in the interference pattern [16]. Unfortunately, a high resolution detector usually only has a small field of view. The method is good at enhancing boundaries and therefore suited for imaging of fibers or foams [15], but less suitable for soft tissue imaging or imaging of highly scattering samples. It is furthermore only possible to retrieve a phase and absorption contrast image from the detector and no information is present on the scattering.

2.1.4 Edge Illumination based Imaging

Edge Illumination (EI) based Imaging was developed at the Elettra synchrotron by Olivo et al. [17] by illuminating only the edge of a detector pixel. EI aims to reproduce the high phase sensitivity of ABI, but without the crystal [18]. At UCL, the feasibility of EI for polychromatic and divergent X-ray beams acquired from a lab-based X-ray source was demonstrated by using two masks, one before the object and one before the detector (Fig. 2.1d). As a consequence, only an edge of the detector is illuminated when no sample is present. An illumination curve describes the relation between the measured intensity at the detector and the relative positions of the two masks [19]. When an object is placed in the sample, deviations of this curve are recorded, from which the first derivative of the phase can be derived. A major advantage is that the phase can be retrieved from only one projection, so that scanning is no longer required and tomography can be done with the setup [20, 21]. The method has several more advantages like a reduced exposure time, a reduced radiation dose and robustness against environmental vibrations. Good results are for instance obtained for imaging of biological tissue [22].

2.1.5 Grating based Imaging

The last type of phase contrast imaging is Grating based imaging (GBI) [23, 24]. In GBI, the first derivative of the phase is measured by the use of two gratings. The first grating, the beam splitter grating, causes interference downstream of the splitter known as the Talbot Effect [25]. When a sample is placed in the scanner, the interference pattern shifts. By subsequently shifting the second grating in

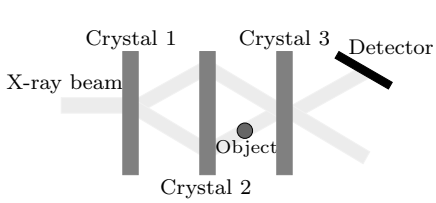

(a) Crystal Interferometer

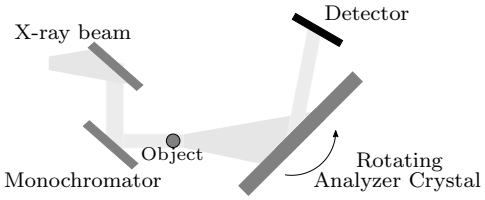

(b) Analyzer based imaging setup

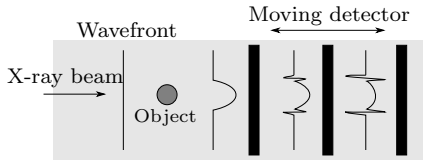

(c) Propagation based imaging setup

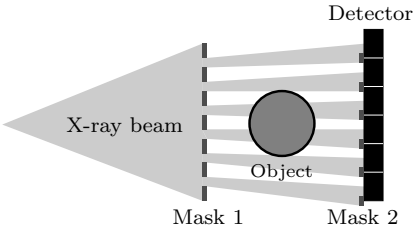

(d) Edge Illumination based setup

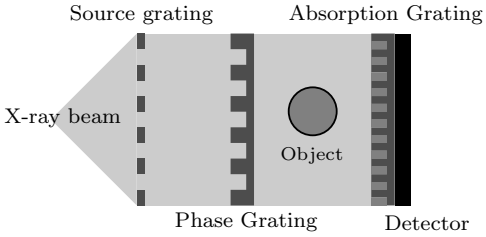

(e) Grating based Interferometer

Figure 2.1: Several Phase Contrast Imaging modalities

several positions, the interference pattern is sampled and the derivative of the phase can be derived. Furthermore, the method also provides information on the absorption and scattering inside the sample [26] and tomography can be performed [27, 28]. To obtain a spatially coherent X-ray beam, a third grating is often placed after the source as shown in Fig. 2.1e. In this thesis, PCCT is performed with GBI. Hence, the technique is discussed in detail in the remainder of this chapter.

2.2 Grating based Interferometer

The algorithms for PCCT that are developed in Chapter 5 and Chapter 6 of this dissertation are all validated on phase data acquired with a Talbot-Lau Grating based Interferometer (TLGI). Therefore, GBI is discussed more into detail in this section. Before going into detail on the principle of the TLGI, an important material property, the refractive index, is discussed in Section 2.2.1. In the refractive index, both the absorption of X-rays and the phase shift imposed to the X-rays induced by a material is contained. Then the Talbot effect is explained in Section 2.2.2 as a building block of the Talbot Lau Grating Interferometer of Section 2.2.3. The section ends with a description of the different signals that can be derived from the measured interference pattern.

2.2.1 Refractive Index

When X-rays pass trough an object, several types of interactions occur as described in the previous chapter. The intensity and type of interactions depend both on the type of material and on the type of X-rays and is captured by the complex *refractive index*:

$$n = (1 - \delta) + i\beta. \tag{2.1}$$

The refractive index consists of a real part $(1-\delta)$ and an imaginary part β. These two parts will be looked at separately. In order to do so, the wave properties of X-rays are studied. An X-ray beam can be described by a plane electromagnetic wave. When k is the wave number, with $k = 2\pi/\lambda$ and λ is the wavelength of the X-rays, a wave travelling in the y-direction can be described as:

$$E = E_0 e^{i(nky-\omega t)} = E_0 e^{i((2\pi ny)/\lambda-\omega t)} = E_0 e^{i((2\pi((1-\delta)+i\beta)y)/\lambda-\omega t)}, \tag{2.2}$$

$$= E_0 e^{-2\pi y\beta/\lambda} e^{i(2\pi y(1-\delta)/\lambda-\omega t)}. \tag{2.3}$$

The amplitude of the wave follows an exponential decay. In Fig. 2.2, the difference between the amplitude before and after the object is given by $\Delta|E| = E_0(1 - e^{-2\pi y\beta/\lambda})$. When the X-ray beam now passes through different materials with

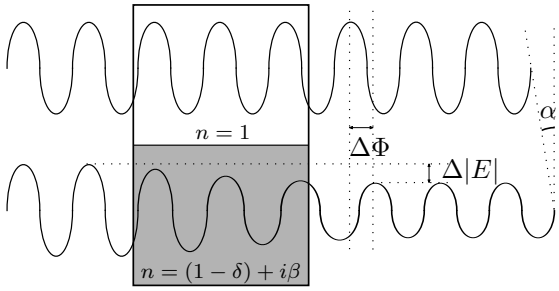

Figure 2.2: Influence of a material with refractive index n on a wave that passes through.

different refractive indices, the amplitude of the wave is given by:

$$|E| = E_0 e^{-\int k\beta(y)dy}. \tag{2.4}$$

Since the intensity of a wave is proportional to the square of the amplitude, the intensity of the beam is equal to:

$$I = I_0 e^{-\int 2k\beta(y)dy}. \tag{2.5}$$

Substituting the linear absorption coefficient $\mu = 2k\beta$ in Eq. 2.5 gives the Lambert-Beer law described in Section 1.2.2.

In this chapter, more attention is given to the real part of the refractive index δ, since it is a measure for the phase shift that an X-ray beam undergoes when it passes through a medium. The phase shift appears because the wavelength of X-rays inside a material changes depending on the refractive index of that material. The phase shift is given by $\Delta\Phi = 2\pi L\delta/\lambda$, where L is the length of the path over which the phase shift occurs. When the X-ray beam passes through different materials with different refractive indices, a more general equation can be derived:

$$\Delta\Phi = k \int \delta(x, y)dy. \tag{2.6}$$

The phase shift is indicated in Fig. 2.2. The shift in phase also causes a shift in the direction of the x-rays. This angular shift is proportional to the first derivative of the phase in the direction opposite to the propagation direction [29]:

$$\alpha(x) = \frac{\partial}{\partial x} \int \delta(x, y)dy. \tag{2.7}$$

In PCCT, a multiple of the angular shift is measured at the detector.

In Als-Nielsen & McMorrow [30] a relationship between the real and imaginary part of the refractive index is described:

$$\frac{\delta}{\beta} = \frac{\sigma_p}{2\sigma_a}, \tag{2.8}$$

where σ_p and σ_a are the absorption and phase-shift cross sections, respectively. An argument in favour of phase contrast imaging is that this ratio is in the range of $10^2 - 10^4$ [31], which means that the probability of a phase shift in the X-ray beam is much higher than the probability of absorption of X-rays. The ratio typically decreases with an increasing atomic number. Certainly for soft tissue, that mainly consists of materials with a low atomic number, phase contrast imaging can thus provide much more insight in the material than conventional transmission X-ray imaging.

2.2.2 Talbot Effect

To measure the angular shift and intensity loss caused by a sample, the TLGI relies on the properties of wave propagation. In free space, the propagation of a wave front in the near-field or Fresnel regime can be calculated by the multiplication of the Fourier transform of the wave front and a propagator function. Hence, due to the propagation of the wave, an interference pattern in constructed. Talbot discovered in 1836 [25] that a periodic wavefront, obtained by illuminating a grating, repeats itself at certain distances. Rayleigh [32] proved that this phenomenon was a consequence of diffraction interference. An extensive study of the properties of Fresnel diffraction behind a periodic object was done by Cowley and Moodie [33]. The distance over which the wave front is repeated is called the Talbot distance defined as:

$$d_T = \frac{2p^2}{\lambda}, \tag{2.9}$$

where p is the period of the wave front and λ is the wavelength of the incoming wave. At certain fractions of this Talbot distance, the pattern of the wave front is also repeated but with only a fraction of the initial period. The idea behind the TGBI is built on this Talbot effect.

2.2.3 Talbot Lau Grating Based Interferometer

With a TLGI [34, 24], the intensity decay of the X-rays as well as the phase shift and the scattering inside a sample are detected by a set-up consisting of a temporally coherent source, a detector and 2 gratings. The first grating, G_1 is a phase shifting gradient where part of the X-rays are transmitted while on the other part, a phase shift π is imposed. Behind this grating, a periodic wave front

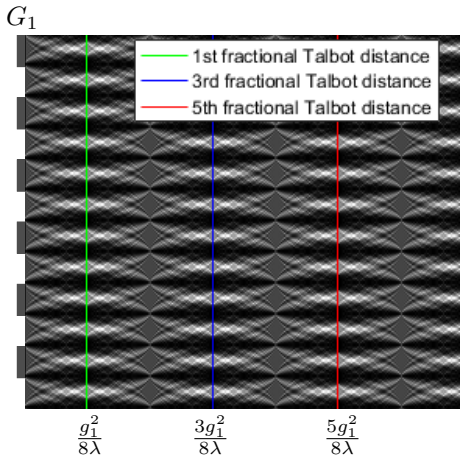

Figure 2.3: The Talbot effect at fractional Talbot distances.[1]

is created, which is a prerequisite for the Talbot effect to occur as seen in the previous section. To induce the phase shift π, the depth of the grating should be designed based on the energy of the incoming X-rays. The period of the grating should depend on the distance L from the source to the first grating and on the distance d between the two gratings. The gratings used in this work all have a duty cycle of 0.5, meaning that half of the signal undergoes a phase shift. After the grating, a Talbot carpet will be constructed with a scaled repetition of the wave front at uneven fractional Talbot distances. Here, the intensity variations are maximal and the period of the wave front is half the original period. The fractional Talbot distances are defined as:

$$d_T^{(f)} = f\frac{g_1^2}{8\lambda}, \tag{2.10}$$

where g_1 is the period of the first grating, λ is the wavelength of the X-rays and f is the uneven fraction $f \in 1, 3, 5, ...$ Fig. 2.3 shows a Talbot carpet with the first three uneven fractional Talbot distances.

To detect the interference pattern at one of the fractional Talbot distances, theoretically, a very high resolution detector should be used. This is however not feasible in practice. Therefore, an absorption grating G_2 is placed before the detector with a period equal to half the period of the first grating. As a result, the period of the grating matches the period of the wave front at that location. The grating absorbs half of the interference pattern, while the other half is transmitted towards a detector with a lower spatial resolution. The interference

[1] Image of the Talbot Carpet made by J. Sanctorum

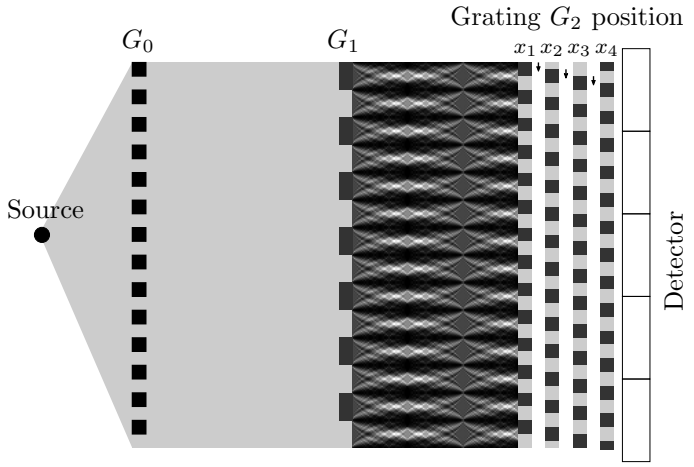

Figure 2.4: The Talbot Lau Grating based Interferometer. [2]

pattern is then detected by acquiring several X-ray images at the same projection direction where the absorption grating has undergone a small shift x_i for every image. By combining the information of all the images, the interference pattern can be constructed as will be discussed in Section 2.2.4. Fig. 2.4 gives a schematic of a Talbot-Lau grating based interferometer with different positions x_i of the absorption grating. The idea behind GBI is now that when an object is placed before grating G_1 or between gratings G_1 and G_2, the interference pattern at the absorption grating will change. By recording the interference pattern with and without object at various projection directions, the differences can be studied and a tomographic image of the object can be reconstructed.

To use the grating interferometer as described above, two important requirements hold for the X-ray beam: the X-rays should not diverge and the beam should have a sustainable transverse coherence [35]. Divergence is a problem that arises both in a lab-based set-up and to a lesser extent also at the synchrotron. As discussed before, an X-ray tube emits X-rays in the form of a cone beam. To account for the divergence, the magnification caused by the fan from the source to the detector should be taken into account:

$$M = \frac{L + d}{d}. \tag{2.11}$$

Here, L is again the distance from the source to the first grating and d is the distance between the two gratings. Both the fractional Talbot distance and the

[2] Image of the Talbot Carpet made by J. Sanctorum

period of the second grating should then be altered to:

$$d_T^{(f)*} = M \cdot d_T^{(f)} = \frac{L}{L - d_T^{(f)}} d_T^{(f)}, \tag{2.12}$$

$$g_2^* = M \cdot \frac{g_1}{2} = \frac{L + d_T^{(f)}}{2L} g_1. \tag{2.13}$$

At a synchrotron, the cone angle and therefore also the magnification are often very small but taking them into account can still improve the reconstruction. Regarding the second requirement, transverse coherence of the beam is necessary to create the expected interference pattern. At the synchrotron, this requirement is met, but for lab-based X-ray sources, the coherence puts a limit on the size of the source. One of the disadvantages of small X-ray sources is that they have a low flux. Therefore, another solution is found where a third grating G_0 is placed right behind the source as shown in Fig. 2.4. The period g_0 of the source grid should be:

$$g_0 = \frac{L}{d_T^{(f)}} g_2, \tag{2.14}$$

so that the interference patterns of two neighbouring source slits overlap at the absorption grating, which will increase the total signal intensity.

2.2.4 Measured Signals

In the previous section, we explained that the interference pattern at the detector is measured by taking multiple X-ray projections, each with a shifted absorption grating. This way, the intensity of the interference pattern in every projection can be written as [35]:

$$I(p_x, p_y, x_g) = \sum_{n=0}^{\infty} a_n(p_x, p_y) \cos\left(\frac{2\pi n x_g}{g_2} - \phi_n(p_x, p_y)\right), \tag{2.15}$$

where (p_x, p_y) is a pixel on the detector, x_g is the position of the absorption grating, a_n are the coefficients of the amplitude and ϕ_n are the phase coefficients. The amplitude and phase coefficients of the intensity curves can either be obtained by cosine fitting with least squares or by Fourier analysis. The latter is much faster and often only requires the first order expansion:

$$I(p_x, p_y, x_g) = a_0(p_x, p_y) + a_1(p_x, p_y) \cos(\frac{2\pi x_g}{g_2} - \phi_1(p_x, p_y)). \tag{2.16}$$

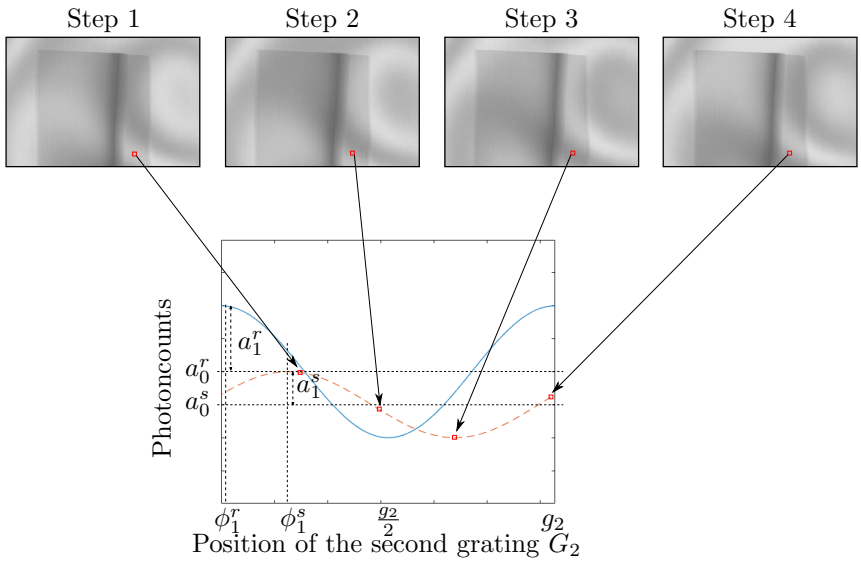

Figure 2.5: Intensity curves of a pixel obtained with the reference scan (blue line) and with the object scan (red line).

In this intensity curve, a_0 describes the average intensity of the interference pattern, a_1 describes the amplitude of the oscillation and ϕ_1 the (shifted) position of the pattern. To interpret a_0,a_1 and ϕ_1 when an object is scanned with a TLGI, a reference signal should be recorded as well. This way, the average intensity, the oscillation amplitude and the position of the pattern can be compared to their reference values to understand the influence of the scanned sample on the X-rays. The parameters are referred to as a_0^s, a_1^s, ϕ_1^s for the scans with sample and a_0^r, a_1^r, ϕ_1^r for the reference scans. The intensity curves of one pixel of the reference and the object scan is shown in Fig. 2.5. From the obtained parameters, three images can be created: *an absorption contrast image, a differential phase contrast image and a dark field contrast image.*

Absorption contrast image

The absorption contrast (AC) image can be formed with the average intensities of the intensity curves. It corresponds to the intensity decay measured in transmission X-ray imaging. The transmission of the X-rays in a pixel (p_x, p_y) is given by:

$$T(p_x, p_y) = \frac{a_0^s}{a_0^r}. \tag{2.17}$$

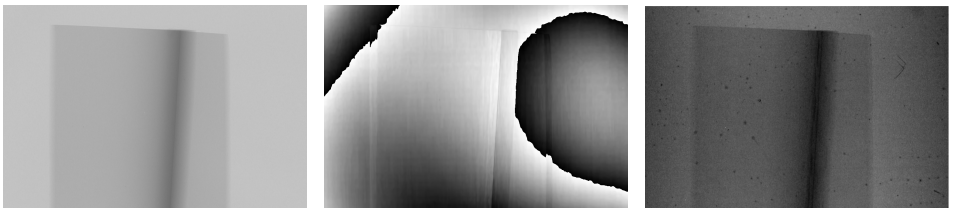

(a) Absorption Image **(b)** Differential Phase Image **(c)** Dark Field Image

Figure 2.6: An absorption contrast, differential phase contrast and dark field contrast image of a CFRP laminate T-piece obtained with the information enclosed in the measured intensity curves at the detector.

The transmission is related to the linear attenuation coefficient μ and the imaginary part of the refractive index β as follows:

$$-\log(T(x)) = \int \mu(x,y)dy = \int 2k\beta(x,y)dy. \tag{2.18}$$

An absorption contrast image from a scan of a CFRP laminate T-piece is shown in Fig. 2.6a.

Differential phase contrast image

The transverse shift of the interference pattern is given by:

$$S(p_x,p_y) = \phi_1(p_x,p_y)\frac{g_2}{2\pi}. \tag{2.19}$$

Since the angular shift $\alpha(p_x,p_y)$ is equal to $S(p_x,p_y)/d_T$ and is defined as in Eq. 2.7, the derivative of the phase Φ of the pattern is given by:

$$\frac{\partial\Phi(p_x,p_y)}{\partial x} = k\alpha(p_x,p_y) = k\frac{g_2}{2\pi d_T}\left(\phi_1^s - \phi_1^r\right). \tag{2.20}$$

An extra integration step is needed to obtain the actual phase shift caused by the sample. In relation to the refractive index, we also recall that:

$$\Phi(p_x,p_y) = \int k\delta(x,y)dy. \tag{2.21}$$

Fig. 2.6b gives an example of a differential phase contrast (DPC) image derived from the measured interference pattern. In the figure, dark regions appear in the

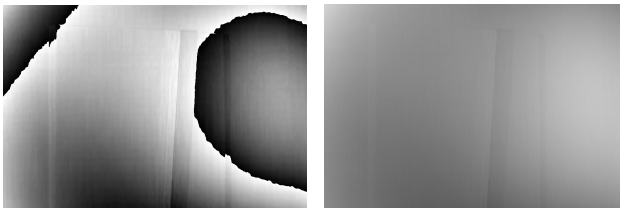

(a) **(b)**

Figure 2.7: **(a)** Wrapped differential phase image and **(b)** Unwrapped differential phase image

left upper corner and at the right hand side. These regions are caused by phase wrapping. The differential phase signal is wrapped in the interval $[0, 2\pi]$, which causes sudden jumps between 0 and 2π at the borders. To retrieve the original differential phase, a phase unwrapping algorithm, like the ones proposed by Van der Jeught [36] or Blinder [37] can be applied on the data. Fig. 2.7 shows the wrapped DPC image as well as the DPC after phase unwrapping.

Dark field contrast image

A third image that can be obtained is a dark field contrast (DFC) image. In this image, the incoherent scattering due to the object, also known as the visibility, is visualized. In Eq. 2.16, a_1 gives the amplitude of the oscillation. When incoherent scattering occurs, this amplitude is reduced and the interference pattern is smeared out. The visibility is then defined as

$$V(p_x, p_y) = \frac{a_1^s / a_0^s}{a_1^r / a_0^r}. \tag{2.22}$$

Consequently, the value will be reduced when incoherent scattering occurs. A DFC image is given in Fig. 2.6c.

2.3 Tomographic Reconstructions

In the previous section, three images were derived from three different signals: the absorption contrast image, the differential phase contrast image and the dark field contrast image. The images can now be used to generate tomographic reconstructions. For the AC image, the process on how to obtain the tomographic reconstructions and several reconstruction algorithms were already discussed in

the previous chapter and will therefore not be repeated here. An example of a 2D reconstruction of the AC data of a CFRP laminate T-piece is shown in Fig. 2.8a. In Section 2.3.1, a FBP like algorithm is discussed for the reconstruction of phase shifts inside a material based on DPC data. Furthermore, the scattering throughout the material can be visualised in a DFC reconstruction image by making some assumptions on the scattering model, which will be explained in Section 2.3.2.

2.3.1 Differential phase data

If the total phase shift could directly be measured by the projection data, the phase shift caused by each voxel of the reconstruction could be obtained with similar techniques as the linear attenuation coefficient. However, with the TLGI, the derivative of the phase shift is measured. The most straightforward way to reconstruct the actual phase shift is by integration of the measured data. This integration will undoubtedly introduce errors in the phase data since the constant of integration is missing. A better way to reconstruct DPC data is to adapt the reconstruction scheme. The FBP is an algorithm where this can simply be done. Recall that for the FBP reconstruction, the projection data is Fourier transformed and then filtered with a Ram-Lak filter before the inverse Fourier transform is applied and the projection data is backprojected. Luckily, the Fourier transform of a derivative of a function has a very fortunate form:

$$\mathcal{FT}\{\frac{df(x)}{dx}\} = 2\pi iqF(q), \tag{2.23}$$

where $F(q)$ is the Fourier transform of $f(x)$. To compensate for the extra factor $2\pi iq$, the Ram-Lak filter can be replaced by an imaginary filter where the denominator is equal to:

$$H(q) = \frac{|q|}{2\pi iq}. \tag{2.24}$$

Multiplication of the Fourier transform of the derivative of the phase shift with this filter will then be the same as filtering the Fourier transform of the phase shift with the Ram-Lak filter. The imaginary filter was first introduced by Pfeiffer in [28].

As seen before, the transverse phase shift that is measured at the detector is related to the angular shift by $\alpha_\theta(p_x, p_y) = S(p_x, p_y)/d_T$, with $S(p_x, p_y)$ the transverse shift and d_T the distance between the two gratings. Since the angular shift is equal to the derivative with respect to x of the integration of the contributions of the real parts δ of the refractive index in every detector pixel along the projection line, the angular shift is the signal that we start from to reconstruct the real part of the refractive index. The 2D FBP reconstruction of the differential phase contrast

data then exists of four steps:

1. The Fourier transform of the measured angular shift $\alpha(x)$ is calculated:

$$A(q,\theta) = \int \alpha(x,\theta) e^{-i2\pi xq} dx = 2\pi i q D(q,\theta), \tag{2.25}$$

   where A is the Fourier transform of α and D is the Fourier transform of δ.

2. In a second step, the Fourier transformed angular shift is filtered by the imaginary filter:

$$F(q,\theta) = A(q,\theta)H(q) = 2\pi i q D(q,\theta)\frac{|q|}{2\pi i q} = |q|D(q,\theta). \tag{2.26}$$

3. Then the inverse Fourier transform of the data is taken:

$$f(x,\theta) = \int_{-\infty}^{\infty} F(q,\theta) e^{2\pi i x q} dq. \tag{2.27}$$

4. Finally, the data is back projected onto the reconstruction grid:

$$\delta(x,y) = \int_0^{\pi} f(x\cos\theta + y\sin\theta, \theta) d\theta. \tag{2.28}$$

An FBP reconstruction of the DPC data of a CFRP laminate T-piece of Fig. 2.6 is shown in Fig. 2.8b. Iterative reconstruction algorithms like Conjugate Gradient also succeed in reconstructing DPC data. Therefore, the system matrix A should be multiplied by an extra matrix D, which models the differentiation. More details are given in Chapter 6.

2.3.2 Dark field data

To perform tomography with DFC data, the small angle scattering inside a material should be modelled. A very simple model that appears to work well assumes that when an X-ray beam passes through a material, the X-rays are scattered in an angular distribution and while passing through the material, the scattering distributions are accumulated. The angular probability distribution of the small angle scattering in that model is assumed to be Gaussian [38, 39]:

$$A(\theta) = \frac{1}{\sigma\sqrt{2\pi}} \exp\left(-\frac{\theta^2}{2\sigma^2}\right). \tag{2.29}$$

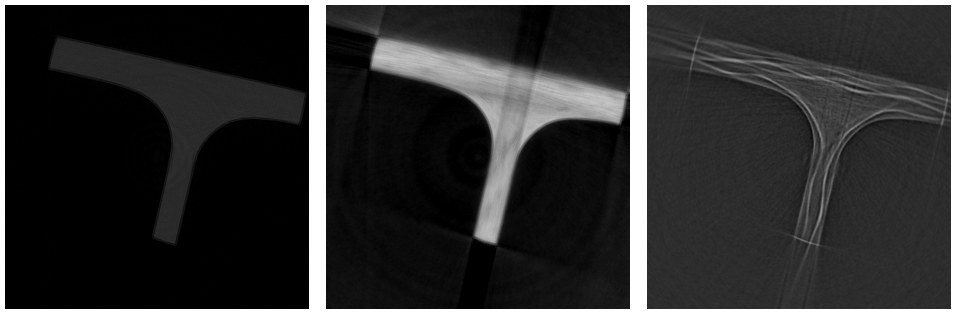

(a) Absorption Reconstruction **(b)** Phase Reconstruction **(c)** Dark Field Reconstruction

Figure 2.8: The three reconstruction images that can be obtained from the measured projection data.

Here σ is the total scattering width, composed of the scattering width of the angular distribution function at each pixel that the ray passes through.

$$\sigma = \sqrt{\sigma_1^2 + \sigma_2^2 + ... + \sigma_N^2}. \tag{2.30}$$

The intensity of the beam is then a convolution of the intensity pattern of Eq. 2.16 and the angular scattering distribution propagated over a distance l from the sample to the analyzer grating G_2 and can be described as:

$$I^s(x) = a_0^r + a_1^r \exp\left(\frac{-2\pi^2}{g_2^2}\sigma^2 l^2\right) \cos\left(\frac{2\pi x}{g_2} - \phi_1\right), \tag{2.31}$$

assuming the absorption contrast is zero. The amplitude of the modulation is now multiplied with an exponential term. Consequently, the visibility can be formulated as:

$$V = \frac{a_1^s a_0^r}{a_1^r a_0^s} = \exp\left(\frac{-2\pi^2}{g_2^2}\sigma^2 l^2\right). \tag{2.32}$$

To be able to apply linear tomographic reconstruction methods, the linear diffusion coefficient ϵ is now introduced. This coefficient describes the small angle scattering width per unit of length and is material dependent. The scattering width along a beam path can then be calculated by integration of the linear diffusion coefficients:

$$\sigma^2 = \int \epsilon(y) dy. \tag{2.33}$$

Rewriting the visibility gives:

$$V(x) = \exp\left(\frac{-2\pi^2 l^2}{g_2^2}\int \epsilon(x,y)dy\right). \tag{2.34}$$

In tomography, the goal is now to reconstruct this linear diffusion coefficient ϵ for each reconstruction voxel. Therefore, the integration of the coefficients over the beam path can be written as:

$$\int \epsilon(x,y)dy = \frac{-g_2^2}{2\pi^2 l^2}\log V(x). \tag{2.35}$$

There is a high similarity between this linear diffusion coefficient and the linear attenuation coefficient. As a result, the reconstruction algorithms for absorption data can also be applied to dark field data provided that the right hand side of Eq. 2.35 is used as projection data. A reconstruction of the linear diffusion coefficient of a CFRP laminate T-piece is shown in Fig. 2.8c.

2.4 Conclusion

In this chapter, a brief introduction on PCCT with a TLGI was given. It was shown that acquisition geometry of a TLGI allows to retrieve information on the real and imaginary part of the refractive index as well as on the small angle scattering inside the sample, which is a great advantage compared to transmission CT. By making some assumptions on the scattering profile, the reconstruction algorithms of Section 1.3 can be used to visualize the small angle scattering distribution and small adaptations to the analytical reconstruction algorithm FBP allow to create DPC tomographic reconstructions.

References

[1] U. Bonse and M. Hart, "An X-ray interferometer," *Applied Physics Letters*, vol. 6, no. 8, p. 155, 1965.

[2] U. Bonse and M. Hart, "An X-ray interferometer with long separated interfering beam paths," *Applied Physics Letters*, vol. 7, no. 4, p. 99, 1965.

[3] A. Momose, "Phase-sensitive imaging and phase tomography using X-ray interferometers," *Optics Express*, vol. 11, no. 19, pp. 2303–2314, 2003.

[4] I. Koyama, H. Yoshikawa, and A. Momose, "Simulation study of phase-contrast X-ray imaging with a triple Laue-case and a triple Bragg-case interferometer," *J. Phys. IV France*, vol. 104, pp. 563–566, 2003.

[5] A. Momose, T. Takeda, A. Yoneyama, I. Koyama, and Y. Itai, "Phase-Contrast X-Ray Imaging Using an X-ray Interferometer for Biological Imaging," *Analytical sciences*, vol. 17, pp. i527–i530, 2001.

[6] K. Goetz, M. Kalashnikov, Y. Mikhailov, G. Sklizkov, S. Fedotov, E. Foerster, and P. Zaumseil, "Measurements of the parameters of shell targets for laser thermonuclear fusion using an X-ray schlieren method," *Soviet Journal of Quantum Electronics*, vol. 9, no. 5, p. 607, 1979.

[7] V. Ingal and E. Beliaevskaya, "X-ray plane-wave topography observation of the phase contrast from a non-crystalline object," *J. Phys. D Appl. Phys.*, vol. 28, pp. 2314–2317, 1995.

[8] T. Davis, D. Gao, T. Gureyev, A. Stevenson, and S. Wilkins, "Phase-contrast imaging of weakly absorbing materials using hard X-rays," *Nature*, vol. 373, pp. 595–598, 1995.

[9] W. H. Bragg and W. L. Bragg, "The reflection of X-rays by crystals," in *Proceedings of the Royal Society A mathematical, physical and engineering sciences*, no. 605, pp. 428–438, 1913.

[10] Z. Zhong, W. Thomlinson, D. Chapman, and D. Sayers, "Implementation of diffraction-enhanced imaging experiments: at the NSLS and APS," *Nucl. Instr. Meth. A*, vol. 450, pp. 556–567, 2000.

[11] M. Wernick, O. Wirjadi, D. Chapman, Z. Zhong, N. Galatsanos, Y. Yang, J. Brankov, O. Oltulu, M. Anastasio, and C. Muehleman, "Multiple-image radiography," *Physics in Medicine and Biology*, vol. 48, pp. 3875–3895, 2003.

[12] J. Keyriläinen, A. Bravin, M. Fernández, M. Tenhunen, P. Virkkunen, and P. Suortti, "Phase-contrast X-ray imaging of breast," *Acta Radiologica*, vol. 51, no. 8, pp. 866–884, 2010.

[13] A. Snigirev and I. Snigireva, "On the possibilities of X-ray phase contrast microimaging by coherent high-energy synchrotron radiation," *Review of Scientific Instruments*, vol. 66, p. 5486, 1995.

[14] P. Cloetens, M. Patyron-Salomé, J. Y. Buffierè, G. Peix, J. Baruchel, F. Peyrin, and M. Schlenker, "Observation of microstructure and damage in materials by phase sensitive radiography and tomography," *Journal of Applied Physics*, vol. 81, no. 9, pp. 5878–5886, 1997.

[15] P. Cloetens, W. Ludwig, J. Bachel, D. Van Dyck, J. Van Landuyt, J. Guigay, and M. Schlenker, "Holotomography: Quantitative phase tomography with micrometer resolution using hard synchrotron radiation X-rays," *Appl. Phys. Lett*, vol. 75, no. 19, pp. 2912–2914, 1999.

[16] T. Gureyev, S. Mayo, D. Myers, Y. Nesterets, D. Paganin, A. Pogany, A. Stevenson, and S. Wilkins, "Refracting Rontgens rays: Propagation-based X-ray phase contrast for biomedical imaging," *Journal of Applied Physics*, vol. 105, no. 10, 2009.

[17] A. Olivo, F. Arfelli, G. Cantatore, R. Longo, R. Menk, S. Pani, M. Prest, P. Poropat, L. Rigon, G. Tromba, E. Vallazza, and E. Castelli, "An innovative digital imaging set-up allowing a low-dose approach to phase contrast applications in the medical field," *Medical Physics*, vol. 28, no. 8, pp. 1610–9, 2001.

[18] P. Munro, C. Hagen, M. Szafraniec, and A. Olivo, "A simplified approach to quantitative coded aperture X-ray phase imaging," *Optics Express*, vol. 21, no. 9, pp. 11187–11201, 2013.

[19] A. Olivo and R. Speller, "A coded-aperture technique allowing X-ray phase contrast imaging with conventional sources," *Applied Physics Letters*, vol. 91, no. 7, p. 074106, 2007.

[20] C. Hagen, M. Endrizzi, P. Diemoz, and A. Olivo, "Revers projection retrieval in edge illumination x-ray phase contrast computed tomogrpahy," *Journal of Physics D: Applied Physics*, vol. 49, no. 25, p. 255501, 2016.

[21] P. Diemoz, F. Vittoria, C. Hagen, M. Endrizzi, P. Coan, E. Brun, U. Wagner, C. Rau, I. Robinson, A. Bravin, and A. Olivo, "Single-image phase retrieval using an edge illumination X-ray phase contrast imaging setup," *J. Synchrotron Radiat.*, vol. 22, no. 4, pp. 1072–1077, 2015.

[22] C. Hagen, P. Maghsoudlou, G. Totonelli, P. Diemoz, M. Endrizzi, L. Rigon, R. Menk, F. Arfelli, D. Dreossi, E. Brun, P. Coan, A. Bravin, P. De Coppi, and A. Olivo, "High contrast microstructural visualization of natural acellular matrices by means of phase-based X-ray tomography," *Scientific Reports*, vol. 5, no. 18156, 2015.

[23] C. David, B. Nöhammer, H. Solak, and E. Ziegler, "Differential X-ray phase contrast imaging using a shearing interferometer," *Appl. Phys. Lett.*, vol. 81, no. 17, pp. 3287–3289, 2002.

[24] F. Pfeiffer, T. Weitkamp, O. Bunk, and C. David, "Phase retrieval and differential phase-contrast imaging with low-brilliance X-ray sources," *Nat. Phys.*, vol. 2, pp. 258–261, 2006.

[25] H. Talbot, "Facts relating to optical science," *Phil. Mag.*, vol. 9, p. 401, 1836.

[26] F. Pfeiffer, M. Bech, O. Bunk, T. Donath, B. Henrich, P. Kraft, and C. David, "X-ray dark-field and phase-contrast imaging using a grating interferometer," *Journal of Applied Physics*, vol. 105, p. 102006, 2009.

[27] A. Momose, W. Yashiro, Y. Takeda, Y. Suzuki, and T. Hattori, "Phase tomography by x-ray Talbot interferometry for biological imaging," *Jpn. J. Appl. Phys.*, vol. 45, no. 6A, pp. 5254–5262, 2006.

[28] F. Pfeiffer, C. Kottler, O. Bunk, and C. David, "Hard X-ray phase tomography with low-brilliance sources," *Phys. Rev. Lett.*, vol. 98, p. 108105, 2007.

[29] T. Jensen, *Refraction and scattering based X-ray imaging*. PhD thesis, University of Copenhagen Faculty of Science, 2010.

[30] J. Als-Nielsen and D. McMorrow, *Elements of Modern X-Ray Physics Second Edition*. Wiley, 2011.

[31] B. Henke, E. Gullikson, and J. Davis, "X-ray interactions: photoabsorption, scattering, transmission, and reflection at E=50-30,000 eV, Z = 1-92," *Atomic data and nuclear data tables*, vol. 54, pp. 181–342, 1993.

[32] L. Rayleigh, "On copying diffraction-gratings, and on some phenomena connected therewith," *The London, Edinburgh, and Dublin Philosophical Magazine and Journal of Science*, vol. 5, pp. 196–205, 1881.

[33] J. Cowley and A. Moodie, "The Scattering of Electrons by Atoms and Crystals I. A New Theoretical Approach," *Acta Cryst.*, vol. 10, p. 609, 1957.

[34] T. Weitkamp, A. Diaz, C. David, F. Pfeiffer, M. Stampanoni, P. Cloetens, and E. Ziegler, "X-ray imaging with a grating interferometer," *Optics express*, vol. 13, no. 16, pp. 6296–6304, 2005.

[35] M. Bech, *X-ray imaging with a grating interferometer*. PhD thesis, University of Copenhagen Faculty of Science, 2009.

[36] S. Van der Jeught, J. Sijbers, and J. Dirckx, "Fast Fourier-Based Phase Unwrappig on the Graphics Processing Unit in Real-Time Imaging Applications," *J. Imaging*, vol. 1, pp. 31–44, 2015.

[37] D. Blinder, H. Ottevaere, A. Munteanu, and P. Schelkens, "Efficient multiscale phase unwrapping methodology with modulo wavelet transform," *Optics Express*, vol. 24, no. 20, pp. 23094–23108, 2016.

[38] Z. Wang, K. Kang, Z. Huang, and Z. Chen, "Quantitative grating-based X-ray dark-field computed tomography," *Appl. Phys. Lett.*, vol. 95, no. 9, 2009.

[39] M. Bech, O. Bunk, T. Donath, R. Feidenhansl, C. David, and F. Pfeiffer, "Quanitative x-ray dark-field computed tomography," *Physics in Medicine & Biology*, vol. 55, no. 18, pp. 5529–5539, 2010.

Part II

Inline X-ray Inspection

3

NN-hFBP for fast inline X-ray inspection

Contents

This chapter has been published as:
E.Janssens, J. De Beenhouwer, M. Van Dael, T. De Schryver, L. Van Hoorebeke, P. Verboven, B. Nicolaï and J. Sijbers *"Neural network Hilbert transform based filtered backprojection for fast inline X-ray inspection"*, Measurement Science and Technology, vol. 29, no. 3, pp. 034012, 2018.

3.1 Introduction

In industry, there is a great demand for fast X-ray inspection and quality control. To make X-ray inspection time efficient, an inline X-ray system is often preferred. Ideally, it should allow individual inspection of every single sample, while preserving a sufficiently high throughput. Inline inspection techniques are already used in different industries, such as agriculture [1, 2], powder metallurgy [3], log scanning [4], dynamic processes [5], metrology [6], and baggage inspection [7].

The fastest and easiest way of inspecting objects inline with X-rays is radiography. To acquire a radiograph, a side-view arrangement is employed with a source and detector on opposite sides of the conveyor belt. Based on the radiograph, interior features of a sample, like dense materials or foreign objects, can be detected [8, 9] or components can be inspected [3]. A high efficiency and a relatively inexpensive infrastructure are the main advantages of X-ray radiography. However, plain radiography comes with a substantial disadvantage: due to the accumulation of the attenuation coefficients along the direction of the projection, depth information is lost and possible defects cannot be spatially resolved in 3D. Moreover, defects may render invisible, hidden behind or in front of materials with a higher attenuation coefficient.

The need for 3D information can be met by using CT. CT is widely used in the field of offline inspection and dimensional metrology [10, 11, 12, 13]. However, full rotation of the object between a fixed source and detector is not possible in an inline setup and full rotation of the source and detector around the object is difficult or even impossible to realise in an inline setup when reconstruction speed and geometrical constraints are an issue. Furthermore, these conventional CT systems come with a high infrastructure cost (>500k euro [14]).

A more cost-friendly X-ray setup that still allows fast and spatially resolved imaging is a side-view arrangement consisting of a fixed cone beam source and a detector moving along with the object, while the object traverses through to the X-ray beam (Fig. 3.2). From the (limited) angular range from which projections are acquired, image reconstruction is possible. However, these images will typically suffer from smearing artefacts due to the missing wedge. Several attempts have been made to reduce these artefacts with iterative reconstruction. Sidky et al., for example, derived a volume image reconstruction technique for a finite straight-line source trajectory [15]. Zhang et al. [16] performed a feasibility study for X-ray tomography in a straight-line trajectory scan based on a total variation iterative procedure. The same group introduced an image reconstruction technique based on total variation minimization and alternating directions to reconstruct images in a linear scan [17]. Despite the improved image quality that can be obtained with these techniques, their usefulness is limited for fast inspection due to the long

computation time of iterative reconstruction methods.

Recently, we introduced an alternative solution to the angular range problem by adding a rotation of the sample around an axis perpendicular to the conveyor belt [18, 19, 20], which largely solves missing wedge artefacts. Nevertheless, even in this scanning geometry the number of projections must be kept small to keep the reconstruction time limited, which may lead to undersampling artefacts. Therefore, in this work, we propose a new type of fast fan beam reconstruction algorithm, analogous to the parallel beam neural network approach of [21, 22]. Our algorithm is based on the Hilbert transform FBP (hFBP) [23] for which the filter is trained by a neural network (NN-hFBP). An advantage of the method is that the NN-hFBP reconstructions can be computed directly from fan-beam data, without the need for rebinning. The algorithm is validated using both simulated and experimental inline scans of agricultural products. It will be shown that the NN-hFBP allows for fast and high quality reconstructions of images in an inline environment from a limited number of projections.

3.2 Methods

In this section, the proposed NN-hFBP algorithm is introduced. The algorithm is based on two existing algorithms: the NN-FBP and the hFBP. The NN-FBP introduced by Pelt et al. [21, 22] creates an image by combining multiple FBP reconstructions, each obtained with a different filter. These filters are trained beforehand in a neural network based on an existing training dataset. High quality images can be reconstructed in a very short time with the NN-FBP. However, the method is only applicable to parallel beam data, which restricts its application for X-ray imaging mainly to synchrotron beamlines. For most X-ray sources, the X-rays are emitted in a cone beam. When only considering the central slice of a cone beam dataset, a fan beam dataset can be obtained. Although rebinning from fan to parallel beam would allow direct application of NN-FBP, it slows down the reconstruction and often introduces interpolation artifacts. Therefore, we chose to adapt the NN-FBP algorithm for direct application to fan beam data. To do this, the hFBP [23] was used instead of the conventional FBP. In the hFBP algorithm, the differential of the Hilbert transform of the projection data is backprojected onto the reconstruction plane to create the reconstructed image. In this paper, the hFBP is first adapted for an inline acquisition geometry [18, 19, 20] in section 3.2.1. Next, an introduction into neural networks as well as a description of the NN-FBP are given in section 3.2.2. Finally, position- and angle independent filters are derived in section 3.2.3, to form the NN-hFBP reconstruction. A schematic of the structure is shown in Fig. 3.1.

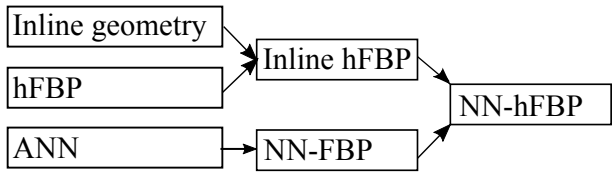

Figure 3.1: Schematic of the structure describing how the NN-hFBP is formed in this paper.

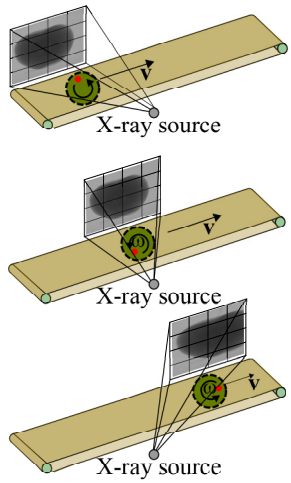

Figure 3.2: Inline inspection with a flat panel detector that moves along with the object while it transverses and rotates.

3.2.1 Inline Hilbert transform based FBP

The inline acquisition geometry that we will work with consists of an object that rotates and translates on a conveyor belt while passing a fixed source and detector system. The detector can either be steady at a fixed position opposite to the source or it can move along with the object over a certain distance. The disadvantage of a fixed detector is its limited field of view, forcing objects to rotate faster to obtain projections from a large angular range. On the other hand, a moving detector should return to its starting position after every sample, therefore slowing down the inspection process and inducing mechanical difficulties. Without loss of generality, we chose the acquisition geometry with a moving detector as shown in Fig. 3.2 for the remainder of the paper.

To adapt the hFBP algorithm so that it can be used for an inline inspection geometry, we start from the Hilbert transform based reconstruction algorithm for parallel beam data. Here, the Hilbert transform is applied on the detector

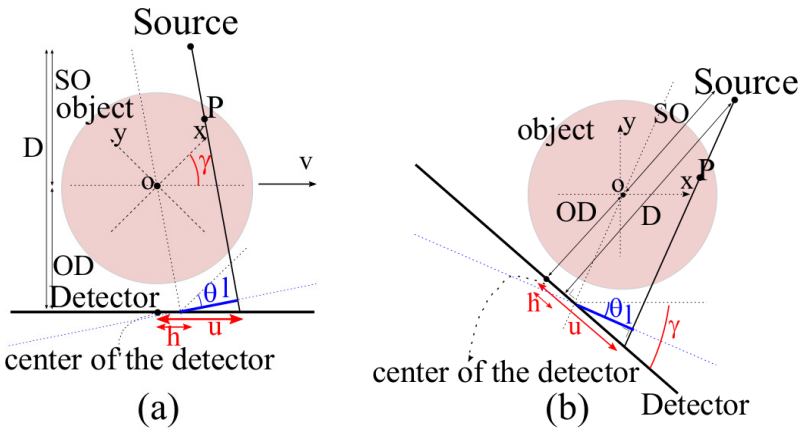

Figure 3.3: Acquisition geometry for inline inspection. (a) Point of view of the fixed source and a rotating and translating object, (b) Point of view of a fixed object and a rotating source and detector.

coordinate. The parallel beam reconstruction formula is given by [23]:

$$f(r,\phi) = \frac{1}{8\pi}\int_0^{2\pi} \frac{\partial p_{\mathrm{H}}(l,\theta)}{\partial l}\mathrm{d}\theta, \tag{3.1}$$

where p_H is the Hilbert transformed projection data, f is the reconstructed image, (r,ϕ) are polar coordinates, and (l,θ) represent the parameters of a parallel beam geometry: the detector pixel and the projection angle, respectively. Our inline acquisition geometry is characterized by the detector pixel u, the translation distance h between the source and the center of the object and the rotation angle γ of the object (cfr Fig. 3.3). Fig. 3.3a shows a projection in the geometry from the point of view of a fixed source and rotating and translating object, while Fig. 3.3b shows the same projection from the point of view of a fixed object where the source and detector are rotating around the object. In Fig. 3.3, D is the distance between the source and the plane of the detector, OD is the distance from the detector to the origin, SO the distance between the origin and a plane through the source parallel to the detector and P a pixel that we want to reconstruct. It is important to notice that the translation distance h is positive when the object is in front of the central position and negative behind the central position.

If the rotation speed ω of the object, expressed in rad/m, is constant, the object's rotation angle γ can be written in terms of this rotation speed and the

translation distance h so that only two independent parameters remain:

$$\gamma = -h \cdot \omega. \tag{3.2}$$

Note that the rotation angle γ is zero when the object is at the central position. Our new reconstruction formula for inline data will be derived from Eq. 3.1. Therefore, we must express Eq. 3.1 in terms of parameters h and u instead of l and θ. To do this, l and θ are first written in terms of u and h:

$$l = \frac{uSO + hOD}{\sqrt{D^2 + (u-h)^2}}, \tag{3.3}$$

$$\theta = -h\omega + \arctan\frac{u-h}{D}. \tag{3.4}$$

To simplify the notation of the upcoming equations, we now introduce a variable $t = u - h$. The Hilbert transform for inline data can now be defined similarly to the Hilbert transform of fan-beam data with a flat panel detector described in [24]. Only in the inline setup, the object is not positioned in the center of the beam. Therefore, we replace the detector pixel u with t, which results in the following Hilbert transform for inline data:

$$p_{\mathrm{H}}^{\mathrm{inl}}(u_i, h_j) = \frac{\sqrt{t_{i,j}^2 + D^2}}{\pi} \int \frac{p^{\mathrm{inl}}(u_i - \tau, h_j)\mathrm{d}\tau}{\tau\sqrt{(t_{i,j} - \tau)^2 + D^2}}, \tag{3.5}$$

where p^{inl} is the inline projection data, $p_{\mathrm{H}}^{\mathrm{inl}}$ is the Hilbert transformed inline projection data, and $t_{i,j} = u_i - h_j$, then Eq. 3.6 holds:

$$p_{\mathrm{H}}^{\mathrm{inl}}(u, h) = p_{\mathrm{H}}\left(\frac{uSO + hOD}{\sqrt{D^2 + t^2}}, -h\omega + \arctan\frac{t}{D}\right). \tag{3.6}$$

A proof, similar to appendix A in [24] for Eq. 3.6 can easily be derived.
To create the reconstruction formula for inline data, Eq. 3.6 is used to adapt equation Eq. 3.1. To express the derivative of the parallel Hilbert transform in terms of the derivatives of the inline Hilbert transform, first the partial derivatives of $p_{\mathrm{H}}^{\mathrm{inl}}$ with respect to u and h are calculated based on Eq. 3.6:

$$\frac{\partial p_{\mathrm{H}}^{\mathrm{inl}}}{\partial u}(u, h) = \frac{D^2 SO - Dht}{\sqrt{(D^2 + t^2)^3}} \frac{\partial p_{\mathrm{H}}(l, \theta)}{\partial l} + \frac{D}{D^2 + t^2} \frac{\partial p_{\mathrm{H}}(l, \theta)}{\partial \theta}, \tag{3.7}$$

$$\frac{\partial p_{\mathrm{H}}^{\mathrm{inl}}}{\partial h}(u, h) = \frac{D^2 OD + Dut}{\sqrt{(D^2 + t^2)^3}} \frac{\partial p_{\mathrm{H}}(l, \theta)}{\partial l} - \left(\omega + \frac{D}{D^2 + t^2}\right) \frac{\partial p_{\mathrm{H}}(l, \theta)}{\partial \theta}. \tag{3.8}$$

This system of equations can now be solved for $\partial p_{\mathrm{H}}(l,\theta)/\partial l$:

$$\frac{\partial p_{\mathrm{H}}(l,\theta)}{\partial l} = \frac{\sqrt{D^2+t^2}}{D+\omega(DSO-ht)}\left[\frac{\partial p_{\mathrm{H}}^{\mathrm{inl}}}{\partial h}(u,h) + \frac{\omega(D^2+t^2)+D}{D}\frac{\partial p_{\mathrm{H}}^{\mathrm{inl}}}{\partial u}(u,h)\right], \tag{3.9}$$

$$= p_{\mathrm{F}_0}^{\mathrm{inl}}(u,h). \tag{3.10}$$

The reconstruction formula for inline data can now be derived from Eq. 3.1 by inserting Eq. 3.9 in Eq. 3.1. This results in the hFBP reconstruction algorithm for fan-beam data in an inline environment where the object rotates with a constant speed ω:

$$\begin{aligned} f(r,\phi) &= \frac{1}{8\pi}\int_0^{2\pi}\frac{\partial p_H}{\partial l}d\theta, \\ &= \frac{1}{8\pi}\int_0^{2\pi}\frac{\sqrt{D^2+t^2}}{D+\omega(DSO-ht)}\left[\frac{\partial p_{\mathrm{H}}^{\mathrm{inl}}}{\partial h}(u,h) + \frac{\omega(D^2+t^2)+D}{D}\frac{\partial p_{\mathrm{H}}^{\mathrm{inl}}}{\partial u}(u,h)\right]\mathrm{d}\theta. \end{aligned} \tag{3.11}$$

Here, f is the reconstructed image and u corresponds to the detector pixel where the ray through (r,ϕ) hits the detector at displacement h and $t = u - h$. To compute the integral, the projection data is interpolated in u and h to obtain data corresponding to the desired parallel beam θ values. Therefore, Eq. 3.3 and Eq. 3.4 should be converted to expressions for u and h. To do this, the $\arctan(\frac{u-h}{D})$ was approximated by $\frac{u-h}{D}$ since $\frac{u-h}{D}$ was small. After discretization of Eq. 3.11, the discrete reconstruction algorithm for inline inspection with a constant rotation speed consists of 4 steps and is described in 3.4.
In the case of equiangular data acquisition, the rotation speed of the object is dependent on its position on the conveyor belt. The rotation angle γ can then be written as:

$$\gamma = \Gamma\frac{\arctan\left(\frac{-h}{SO}\right)-\arctan\left(\frac{-h_{\mathrm{st}}}{SO}\right)}{\arctan\left(\frac{-h_{\mathrm{e}}}{SO}\right)-\arctan\left(\frac{-h_{\mathrm{st}}}{SO}\right)} - \gamma_{\min}, \tag{3.12}$$

$$= \omega'\left(\arctan\left(\frac{-h}{SO}\right) - a\right) - \gamma_{\min}. \tag{3.13}$$

Here, Γ is the total angular range over which the object will rotate, $\gamma_{\min}$ is the angle over which the object rotates from the first projection until the central position and ω' and a are constants defined as: $\omega' = \frac{\Gamma}{\arctan\left(\frac{-h_{\mathrm{e}}}{SO}\right)-\arctan\left(\frac{-h_{\mathrm{st}}}{SO}\right)}$ and $a = \arctan\left(\frac{-h_{\mathrm{st}}}{SO}\right)$ with h_{e} the last h-value and h_{st} the first h-value. The positions h_i on the conveyor belt at which projections are taken are distributed in such a way that, without rotation of the object, the projections would be acquired

equiangularly:

$$h_i = SO \cdot \tan\left(\alpha_{\min} + (i-1) \cdot \Delta\alpha\right). \tag{3.14}$$

In Eq. 3.14, $\alpha_{\min} = \arctan(\frac{-h_{\text{st}}}{SO})$ and $\Delta\alpha$ is the angle between two successive projections. The partial derivative with respect to l of the Hilbert transformed parallel projection data, similar to Eq. 3.9 or step 2 of the reconstruction algorithm then becomes:

$$p_{\text{F}_0}^{\text{inl}}(u_i, h_j) = \frac{\sqrt{D^2 + t_{i,j}^2}}{D(SO^2 + h_j^2) + \omega SO(DSO - h_j t_{i,j})} \cdot \left[(SO^2 + h_j^2) \frac{\partial p_{\text{H}}^{\text{inl}}(u_i, h_j)}{\partial h} + \frac{(D(SO^2 + h_j^2) + \omega SO(D^2 + t_{i,j}^2))}{D} \frac{\partial p_{\text{H}}^{\text{inl}}(u_i, h_j)}{\partial u} \right]. \tag{3.15}$$

3.2.2 Neural Network based FBP

In this section, a brief introduction into artificial neural networks is given, after which the NN-FBP of Pelt et al. is discussed concisely.

3.2.2.1 Artificial Neural Networks

Artificial Neural Networks (ANN) are mathematical models with a learning capacity inspired by the human brain. They are used to approximate a certain unknown function $f : \mathbb{R}^n \to \mathbb{R}^m$ in different application domains like prediction [25], classification [26], object detection [27] and identification [28]. One type of neural network is the multilayer perceptron (MLP) [29, 30]. Here, we define a perceptron consisting of 3 different layers as shown in Fig. 3.4: an input layer with n nodes for an input $\boldsymbol{x} \in \mathbb{R}^n$, a layer of N hidden nodes and an output layer with m output nodes generating output $\boldsymbol{z} \in \mathbb{R}^m$. The MLP is fully connected: every input node is connected to every hidden node with weight matrix $\boldsymbol{W} \in \mathbb{R}^{n \times N}$ and every hidden node is connected to all the output nodes with weight matrix $\boldsymbol{Q} \in \mathbb{R}^{m \times N}$. To allow the ANN to describe non-linear functions, two activation functions $\sigma(.)$ and $\sigma_0(.)$ are incorporated. They are applied to every hidden node and output node, respectively. In this work, the sigmoid function is used for both activation functions. The decision boundary of this sigmoid function is centered around 0. By subtracting biases $\boldsymbol{b_0}$ and b_i from every hidden node and output node before applying the activation function, this decision boundary can be changed, which allows to approximate many more functions [30]. The output of the network can

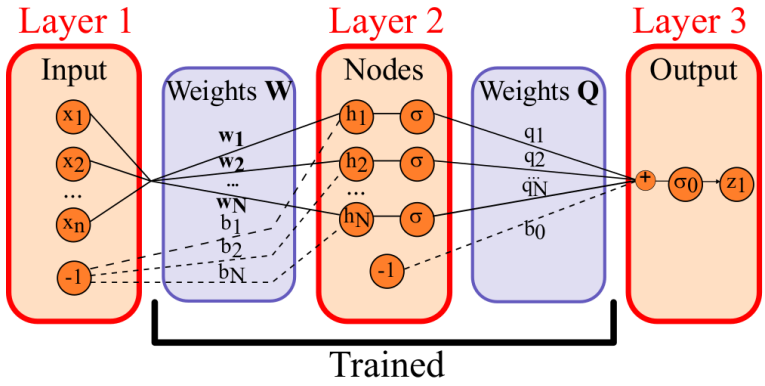

Figure 3.4: A multilayer perceptron consisting of three layers with one output node
Every input node is connected to every hidden node with weight matrix $\boldsymbol{W}$ and every hidden node is connected to the output node with weight matrix $\boldsymbol{Q}$. On every hidden and output node, an activation function is applied and biases are subtracted.

then be written as:

$$\boldsymbol{z}_{\boldsymbol{Q},\mathbf{W},\boldsymbol{b},\boldsymbol{b}_0}(\boldsymbol{x}) = \sigma_0 \left(\sum_{i=1}^{N} \boldsymbol{q_i} \sigma \left(\boldsymbol{w_i}^T \boldsymbol{x} - b_i \right) - \boldsymbol{b}_0 \right). \tag{3.16}$$

Here, $\boldsymbol{q_i}$ and $\boldsymbol{w_i}$ are the columns of the weight matrices $\boldsymbol{Q}$ and $\boldsymbol{W}$, respectively.

To use the network to approximate an unknown non-linear function f given a certain input $\boldsymbol{x}$, the weights $\boldsymbol{w_i}$ and $\boldsymbol{q_i}$ and biases $\boldsymbol{b}$ and $\boldsymbol{b_0}$ of the network must be trained. To this end, the network is trained in a supervised way, which requires a training and validation dataset. For these two sets, both the inputs $\boldsymbol{x}_k$ and the corresponding correct outputs $\boldsymbol{y}_k$ should be available. The network then trains the weights and biases by minimizing the sum of the squared errors between the correct outputs $\boldsymbol{y}_k$ of the training dataset and the outputs obtained by the network $\boldsymbol{z}_k$ using the Levenberg-Marquardt algorithm (LMA) [31]. Algorithm 1 [22] describes the different steps performed to train the neural network.

Algorithm 1: Training

1. Create training and validation dataset
2. Initialize parameters $\boldsymbol{W}$ and $\boldsymbol{Q}$, $\boldsymbol{b}$ and $\boldsymbol{b_0}$ of the network.
3. Iterate

   (a) Perform one LMA iteration on the training dataset
   (b) Calculate the squared error of the validation dataset
   (c) If the validation error does not improve for N_{stop} iterations, stop iterating
4. Return parameters $\boldsymbol{W}$ and $\boldsymbol{Q}$, $\boldsymbol{b}$ and $\boldsymbol{b_0}$ with the lowest validation error

---

Choosing the number of hidden nodes N in a multilayer perceptron is a difficult task. If N is chosen too small, the network will not be able to approximate the required function correctly, which is called underfitting. For a large N, on the other hand, the network will be more prone to overfitting to the training data. The validation set is used to prevent the network from the latter. Several factors influence the choice of N: the number of inputs and outputs, the training algorithm, the architecture of the network, the training set, the noise in the data, and the type of activation functions. Throughout the years, much research is done to determine the best choice of hidden nodes in an ANN. The most basic methods follow one of three thumb rules: N should be between the size of the input layer and the size of the output layer, N should be 2/3th of the sum of the sizes of the input and output layer and the number of hidden nodes should be less than twice the size of the input layer [32, 33]. More advanced methods are described in [33], in which Gnana Sheela and Deepa made a thorough review of the main research in this domain for the last twenty years. In this review, the selection of the number of hidden nodes is done by minimizing the error between the true output and the network output. In our work, not only the validation error should be minimized but also the calculation time from input to output is an important parameter to take into account. Therefore, a balance should be found between these two values and for every specific application, this balance should be evaluated.

An example for which the neural network can be used to approximate a function is the reconstruction of an image based on X-ray projection data. Several methods have been proposed to use an ANN for image reconstruction with X-rays. The easiest way is to give the projection data as an input to the neural network and the reconstruction image pixels as the output. This is done by Paschalis et al. in [34], but it results in a neural network with many input and output nodes where a very large dataset is required to train the network. Cierniak [35, 36, 37] uses another type of neural network, a Hopfield neural network, to reconstruct images based on the projection data. Here, the number of neurons in each layer is equal to the number of reconstructed pixels, so that the network easily becomes very large with increasing image sizes. Another method is applied in [38, 39] where the image pixel positions are the input of the neural network and the output is the

value of the reconstructed image at that pixel. The networks are trained based on the difference between the projection data of the reconstructed image and the original projection data. It can be used in cases where no training data is available. The major drawback is, however, that the network is image specific, so for every reconstruction image, the network should be reset.

3.2.2.2 NN-FBP

Pelt et al. [21, 22] combined the multilayer perceptron and the FBP algorithm to introduce the Neural Network Filtered Back Projection (NN-FBP) algorithm for parallel beam data. This algorithm enables fast reconstruction of 2D images from a set of parallel beam X-ray projections. Instead of reconstructing the whole image as an output, the network is trained to reconstruct only 1 pixel value (i.e., only 1 output node). Since the FBP is shift invariant, the input is created by first shifting the projection data, then summing it over all projection angles and reflecting the final result. Multiplication of this input with a filter is then actually the same as a filtered backprojection which reconstructs only 1 pixel. The network trains different filters, contained in the columns of the weight matrix $\boldsymbol{W}$ of the multilayer perceptron, as well as the weights q_i and biases $\boldsymbol{b}$ and b_0. To create a final reconstruction image, the NN-FBP performs several FBP reconstructions, each with a different filter from matrix $\boldsymbol{W}$, applies a non-linear activation function on each of them, and combines them according to the weights q_i of the network. The final reconstruction image is then obtained after applying the second activation function. Algorithm 2 [22] describes the NN-FBP reconstruction algorithm stepwise.

Algorithm 2: NN-FBP

1. Train the network for $\boldsymbol{W}$, $\boldsymbol{Q}$, $\boldsymbol{b}$ and b_0.
2. Perform N FBP reconstructions, each with a different filter (the columns of matrix $\boldsymbol{W}$) trained by the ANN.
3. Subtract a bias b_i from every image and apply an activation function $\sigma(.)$ on every pixel.
4. Add the different FBP reconstructed images pixel by pixel with weights q_i of the ANN.
5. Subtract a bias b_0 from the combined image and apply the same activation function $\sigma(.)$ to obtain the final reconstructed image.

3.2.3 NN-hFBP

The inline hFBP reconstruction of section 3.2.1 can now be combined with the NN-FBP of Pelt et al. to provide fast, high quality reconstructions for fan-beam data in an inline environment. This is, however, only possible when the hFBP is written as the product of a certain input with a position and angle independent filter. In 3.4, it is shown that the inline hFBP can be written as the sum of two terms with each term the convolution of a datavector (I_1 and I_2) of size n (the number of detector pixels) and a filter (f_1 and f_2):

$$f(r,\phi) = \sum_{\tau} f_1(\tau) I_1(u-\tau) + f_2(\tau) I_2(u-\tau), \tag{3.17}$$

where u represents the detector pixel where the ray through (r,ϕ) hits the detector. Since the neural network performs a convolution of an input with a filter, this means that the hFBP can be implemented in a neural network to create the NN-hFBP. To do this, first the correct datavectors I_1 and I_2 should be generated based on the acquired projection data to train the filters (see 3.4). For every detector pixel, two datavectors are generated which are stored in one input vector of size $2n$ so that the total length of the input of the neural network is twice the size of the detector. Once these datavectors are obtained, instead of using the normal filters of the hFBP (described in Eq. 3.25 and Eq. 3.26), the network is trained so that the weight matrices $W_1 \in \mathbb{R}^{n\times N}$ and $W_2 \in \mathbb{R}^{n\times N}$ between the $2n$ input nodes and the N hidden nodes of the multilayer perceptron define new filters $\boldsymbol{w_{1i}} \in \mathbb{R}^n$ and $\boldsymbol{w_{2i}} \in \mathbb{R}^{\boldsymbol{n}}$ for the hFBP reconstructions, which are the columns of the weight matrices W_1 and W_2 (replacing the filters f_1 and f_2). This means that after training the network, several hFBP reconstructions can be computed with these new filters instead of the filters of Eq. 3.25 and Eq. 3.26. Finally, the reconstructions are combined using the activation functions σ and σ_0 (in our case sigmoid functions), the trained weights $\boldsymbol{q} \in \mathbb{R}^N$, and the biases $\boldsymbol{b} \in \mathbb{R}^N$ and b_0 of the neural network, as shown in Fig. 3.5. The final reconstruction formula then becomes:

$$f(r,\phi) = \sigma_0\left(\sum_{k=0}^{N-1} q_k \sigma\Big(\sum_{\tau}(\boldsymbol{w_{1k}}(\tau) I_1(u-\tau) + \boldsymbol{w_{2k}}(\tau) I_2(u-\tau)) - b_k\Big) - b_0\right), \tag{3.18}$$

where $\boldsymbol{w_{1k}}$ and $\boldsymbol{w_{2k}}$ are the filters trained by the neural network.

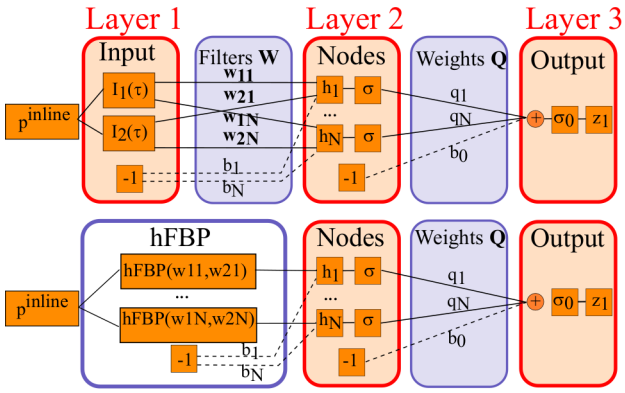

Figure 3.5: Scheme of the NN-hFBP reconstruction: For training, inputs I_1 and I_2 are created from the projection data with which the filters $\mathbf{w_{1i}}$ and $\mathbf{w_{2i}}$ are trained in the top row. For reconstruction, the filters $\mathbf{w_{1i}}$ and $\mathbf{w_{2i}}$ are combined and used as the new filters to perform several hFBP reconstructions in the second row.

3.3 Experiments and Results

In this section, the performance of the NN-hFBP algorithm is evaluated with both simulated and real inline data. First, using simulation experiments, the acquisition settings and NN-hFBP network parameters are optimized for maximal image quality. In particular, the influence of equiangular versus non-equiangular sampling, the rotation speed of the sample and the number of hidden nodes of the network was studied in terms of image quality. Secondly, the reconstruction quality of the (optimized) NN-hFBP was compared to that of the conventional reconstruction algorithms FBP and SIRT with 500 iterations. Finally, the performance and image quality of NN-hFBP versus conventional reconstruction algorithms were evaluated using real data experiments. The evaluation of the image quality was done by 4 different evaluation methods:

The Root Mean Squared Error (RMSE) evaluates the reconstructed image pixelwise and combines the pixelwise differences into one final RMSE value. The RMSE is defined as

$$\mathrm{RMSE} = \sqrt{\frac{\sum_{i=1..M}(rec(i) - GT(i))^2}{M}}, \tag{3.19}$$

where rec is the reconstructed image, GT is the ground truth image and M is the number of pixels in the image. The RMSE measure was used twice: once when evaluating on the whole image (global RMSE) and once when

evaluating only on the apple, bell pepper or walnut region (local RMSE).

The Most Apparent Distortion (MAD) compares two images based on a combination of the detection-based strategy and the appearance-based strategy of the human visual system (HVS). The detection-based strategy describes the phenomenon when the distortions in an image are near-threshold so that the HVS tends to look past the image to the distortions. The appearance-based strategy describes the phenomenon when the distortions are most apparent so that the HVS tends to look past the distortions to see the image. The distortions from the first strategy are calculated based on local luminance and contrast masking, the second type of distortions are calculated by looking at the changes in the local statistics of spatial-frequency components. Combining these two measures results in a MAD value, which should be as low as possible [40].

The Feature Similarity Index (FSIM) takes into account that the HVS understands an image based on its low-level features. The two features that are exploited here are the phase congruency and the image gradient magnitude. Combining these features results in a value between 0 and 1, where the FSIM is 1 if the two images are identical [41].

For all experiments, reconstructions were made using the ASTRA Toolbox [42, 43, 44] where all forward and backprojections were calculated on an NVIDIA GeForce GTX 580 GPU.

3.3.1 Simulation Experiment

To evaluate the performance of the NN-hFBP algorithm on simulation data, inline experiments were simulated that mimic the behavior of a real inline scan. X-ray CT scans of apples and bell peppers were used as test samples, for which the detection of small structural changes such as holes or browning are of interest. Inline CT data were created starting from conventional circular CT scans of apples and bell peppers from respectively 470 and 632 equiangular projections of 1024×1024 pixels. From these scans, inline scans were simulated by reorganizing corresponding rays. Such simulated inline projection data naturally accounts for a realistic polychromatic source as well as realistic noise behaviour.

Specifications of the geometry are given in 3.1. The translation distance is expressed as the distance in mm compared to the central position on the conveyor belt opposite to the source. For the experiments, four types of apples and one type of bell pepper were used. The number and types of apples and bell peppers used for training, validation and testing in the different experiments is shown in 3.2.

Table 3.1: Specifications scanning geometry.

	Simulations	Real Data
Detector pixels	1148	1146
Detector pixel size	127μm	127μm
Translation distance [mm]	[-250, 250]	[-250, 250]
Object Detector distance	84.500mm	84.527mm
Source Object distance	900mm	563mm
Downsampling	4	2
Image pixels	256×256	400×400
Image pixel size	400μm	200μm

Table 3.2: Datasets.

	Training Set	Validation Set	Test Set
Braeburn 1	8	4	4
Braeburn 2	20	7	10
Jonagored	10	6	7
Jonagold	15	6	10
Bell Pepper	15	5	10

For each experiment, 10 instances of every network were trained by randomly selecting different sets of pixels of the same image data. Each ANN was trained based on 100.000 random pixels for training and validated with 10.000 random pixels. For each of the four apple types, 100 slices of the training datasets were used for training and 10 slices of the validation datasets for validation. In case of the bell peppers, only the central slice of each bell pepper was used for training and validation since the scan quality was not good enough to make fan-beam reconstructions of non-central slices. For the bell peppers, the ANN was trained based on 15 training images and 5 validation images. The reconstruction quality was tested on 50 images for the apple datasets and on 10 images for the bell peppers.

Before describing the first experiment, we note that the hFBP and the NN-hFBP both require an interpolation step. This step causes higher reconstruction times and introduces blurring in the reconstruction in few-view acquisitions. Therefore, in this paper, we propose a heuristic approach where we omit the interpolation step and directly backproject the data along the inline fan-beam projection geometry. This means that for every pixel in the reconstruction grid, data from slightly different parallel projection angles θ is summed up. Although this is an approximation, avoiding the interpolation step makes the reconstruction much faster with only a slight loss of reconstruction quality. The effects of interpolation

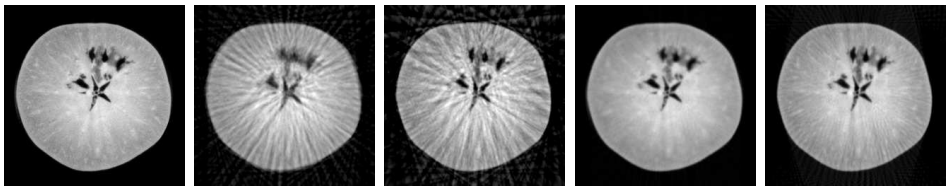

(a) (b) (c) (d) (e)

Figure 3.6: Comparison of the interpolation and the heuristic method. (a) ground truth image, (b) hFBP reconstruction with interpolation from 32 projections over 2π, (c) heuristic hFBP reconstruction from 32 projections, (d) hFBP reconstruction with interpolation from 128 projections, (e) heuristic hFBP reconstruction from 128 projections.

on the hFBP and the NN-hFBP reconstruction quality can be seen in Fig. 3.6b and Fig. 3.7b, respectively on two inline scanned apples with ground truth images in Fig. 3.6a and Fig. 3.7a. To avoid the blurring and to further reduce the computation time, we propose to omit the interpolation step and directly backproject the data along the inline fan-beam projection geometry. In Fig. 3.6, NN-hFBP is compared to hFBP with interpolation and the heuristic hFBP reconstruction for 32 and 128 projection angles. The hFBP with interpolation provides good image quality when a sufficiently high (in this case 128) number of projections are available, but blurring artifacts appear when only a small number of projections are present. With the heuristic approach, the holes are less blurred than with the interpolation approach for 32 projections. For 128 projections, streaking artefacts appear in the heuristic reconstructions, but the reconstruction is less blurred and the holes and brown spots are still clearly visible. In Fig. 3.7, a similar comparison is made between an inline NN-hFBP reconstruction with interpolation and a heuristic inline NN-hFBP reconstruction for 32 and 128 projection angles. With the heuristic approach, streak artefacts appear again at the outside of the apple, but the small holes are detected with 32 projections, which is not the case for the conventional NN-hFBP method. Fig. 3.6 and Fig. 3.7 clearly indicate that a choice should be made between blurring or streaks in the reconstructions made with only few projections. Based on the capacity of the heuristic NN-hFBP to better detect the holes with less blurriness for a small number of projections and the faster reconstruction time, we decided to use the heuristic approach in the rest of this paper.

In the first experiment, we optimize the acquisition and network parameters to evaluate the reconstruction quality of the NN-hFBP. Important parameters for data acquisition are the rotation speed and rotation direction of the objects. Therefore, in this experiment, we first evaluate the reconstruction quality (in terms of the global RMSE) of the NN-hFBP of the Braeburn 1 apples as a function of

(a) (b) (c) (d) (e)

Figure 3.7: Comparison of the interpolation and the heuristic method in a neural network. (a) ground truth image, (b) NN-hFBP reconstruction with interpolation from 32 projections over 2π, (c) heuristic NN-hFBP reconstruction from 32 projections, (d) NN-hFBP reconstruction with interpolation from 128 projections, (e) heuristic NN-hFBP reconstruction from 128 projections.

the rotation speed when 128 projections are acquired equiangularly (cfr: Fig. 3.8). The rotation speed is expressed in terms of the angular range Γ over which the apple has rotated from the first projection to the last projection and ranges between $-\pi$ and π. The corresponding reconstructed images are shown in Fig. 3.9. From the graph and the images, it is immediately clear that rotation substantially improves the reconstruction quality. Without rotating the object, substantial limited wedge artefacts appear. Furthermore, there is an obvious difference between a counterclockwise and clockwise rotation. When the object rotates counterclockwise at a slow rotation speed, the different intrinsic projection angles at which the projections are required without rotation are counteracted by the rotation so that the reconstruction is similar to no rotation. A clockwise rotation however allows to substantially increase the angular range, resulting in a higher reconstruction quality.

Secondly, we inspect the influence of two different types of sampling of the projections on the final reconstruction quality. Unless prior knowledge is available about the object to be inspected, equiangular sampling is expected to be optimal. On the other hand, a constant rotation speed and equidistantly acquired projections may have a practical advantage. Hence, we investigate the difference between the reconstruction quality of the NN-hFBP for Braeburn 2 apples that rotate with a constant rotation speed (non-equiangular projections) versus apples that rotate with a varying rotation speed so that the acquired projections are equiangular. The results in terms of the global RMSE as a function of the number of projections, both with equiangular (EA) and non-equiangular (NEA) projections, are compared in Fig. 3.10. It can be seen that the reconstruction quality is very similar. Hence, in this acquisition setup, there is not a large gain by acquiring the projections equiangularly. This is a desired characteristic since it facilitates the data acquisition. Projections can then be taken at equidistant positions and the

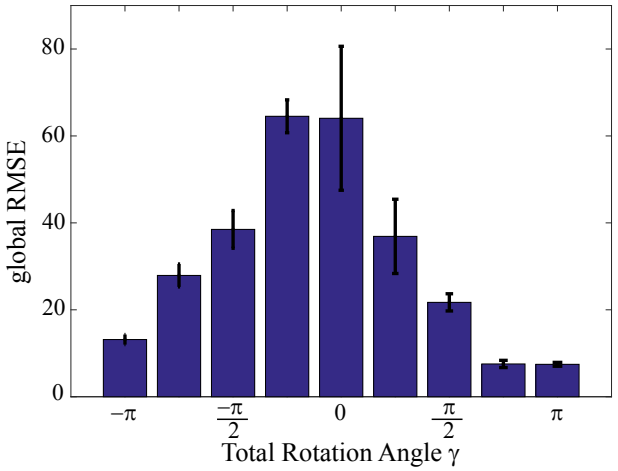

Figure 3.8: The global RMSE of the NN-hFBP reconstruction for different angular ranges.
The x-axis gives the total angular range Γ over which the apple has rotated.

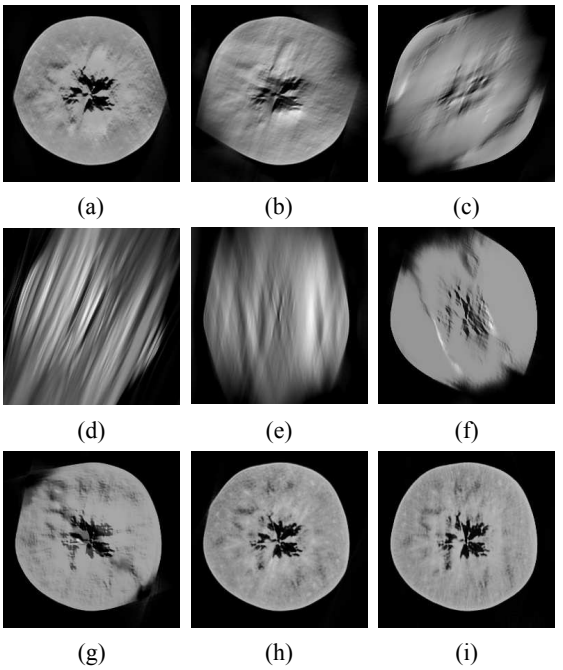

Figure 3.9: Reconstruction images of the apples made with the NN-hFBP for angular ranges Γ equal to (a) $-\pi$, (b) $-3\pi/4$, (c) $-\pi/2$, (d) $-\pi/4$, (e) 0, (f) $\pi/4$, (g) $\pi/2$, (h) $3\pi/4$, (i) π

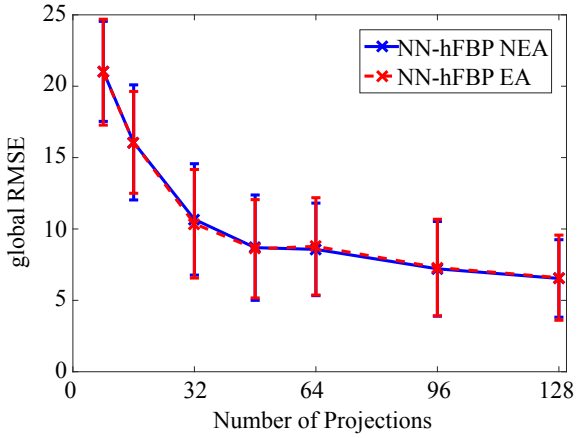

Figure 3.10: Global RMSE for non-equiangular and equiangular NN-hFBP reconstructions in function of the number of projections.

rotational speed of the apple can be kept constant.

Finally, we optimize the number of hidden nodes and thus the number of hFBP reconstructions that are combined in the neural network as it represents a trade-off between reconstruction quality and speed. We therefore examine the influence of the number of hidden nodes N of the ANN on the reconstruction quality of the NN-hFBP evaluated on Jonagored apples with a constant rotation speed and $N = 1, 2, 4$ and 8. Fig. 3.11a shows the RMSE over the whole image and Fig. 3.11b the reconstruction time in function of the number of projections. The four graphs represent the cases of 1,2,4 and 8 hidden nodes. From the graphs, one can see that increasing the number of hidden nodes improves the reconstruction quality. However, it also increases the reconstruction time. For 32 and 128 projections, the reconstructed images are shown in Fig. 3.12. To balance the reconstruction quality and reconstruction time, we have chosen to use 4 hidden nodes, aiming to optimize the reconstruction quality while preserving a reconstruction time of less than 100ms for 128 projections.

From the three experiments, optimal conditions can be derived for the NN-hFBP reconstructions. Now, the reconstruction quality of the NN-hFBP is compared to the quality of the conventional algorithms SIRT and FBP. Results of a comparison with hFBP were omitted, as NN-hFBP clearly outperforms hFBP in terms of reconstruction quality. Fig. 3.13 shows the reconstruction quality of FBP, SIRT and the NN-hFBP as a function of the number of projections in terms of the global RMSE (a), the local RMSE (b), MAD (c) and FSIM (d). As is clear from the plots, the reconstruction quality of NN-hFBP is significantly better than

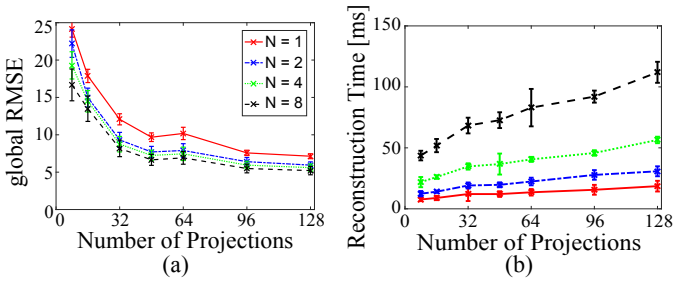

Figure 3.11: Evaluation of the reconstruction quality in terms of the global RMSE (a) and reconstruction time (b) of the NN-hFBP evaluated on Jonagored apples based on 1, 2, 4 and 8 hidden nodes for different number of projections.

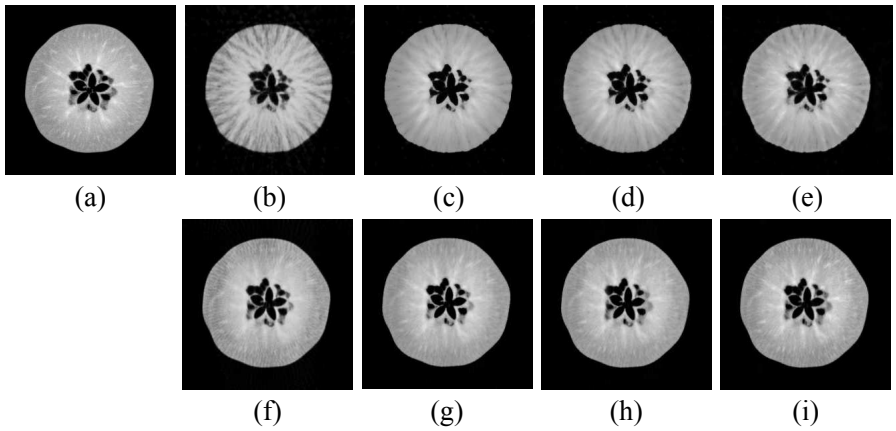

Figure 3.12: (a) ground truth image of a Jonagored slice, (b-e) NN-hFBP reconstructions of 32 projections with 1 (b), 2 (c), 4 (d) and 8 (e) hidden nodes, (f-i) NN-hFBP reconstructions of 128 projections with 1 (f), 2 (g), 4 (h) and 8 (i) hidden nodes.

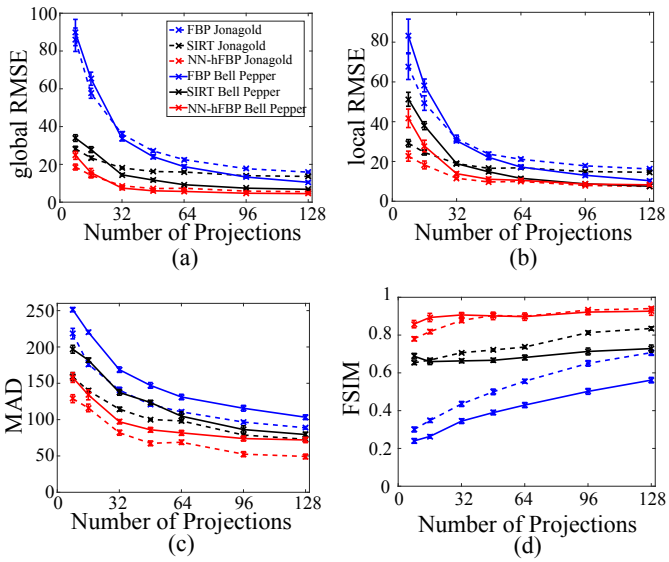

Figure 3.13: Evaluation of the reconstruction quality for FBP, SIRT and NN-hFBP in terms of the global RMSE (a), local RMSE (b), MAD (c) and FSIM (d), both for Jonagold apples and bell peppers.

that of FBP and SIRT for all number of projections, both for the Jonagold apples and the bell peppers. In particular, the quality of the NN-hFBP reconstructions in terms of the FSIM is much better than that of FBP and SIRT. This might be because the NN-hFBP is capable of clearly detecting the shape of the object and important features like holes and the core of the apple even with a very small number of projections, in contrast to FBP and SIRT.

A comparison of the reconstructed Jonagold and bell pepper slices from 32 projections with the different methods is shown in Fig. 3.14. One can clearly see that the NN-hFBP outperforms the other reconstruction algorithms since much more noise is present in the FBP reconstruction (signal-to-noise ratio of 13.44 vs 4.91 for bell peppers and 9.72 vs 4.80 for apples) and the SIRT reconstruction is slightly blurred. Example images for comparing the reconstruction quality of the NN-hFBP with different numbers of projections are shown in Fig. 3.15 for 16, 32, 64 and 128 projections. On the images made with 16 projections, many artifacts appear which make the detection of undesired regions impossible. The black regions at the outside of the apple might suggest that there are holes as well. Also for the bell pepper, not much information can be obtained with 16 projections. However, from the images obtained with 64 projections, the holes are clearly visible in the reconstruction. Despite the radial lines at the outside

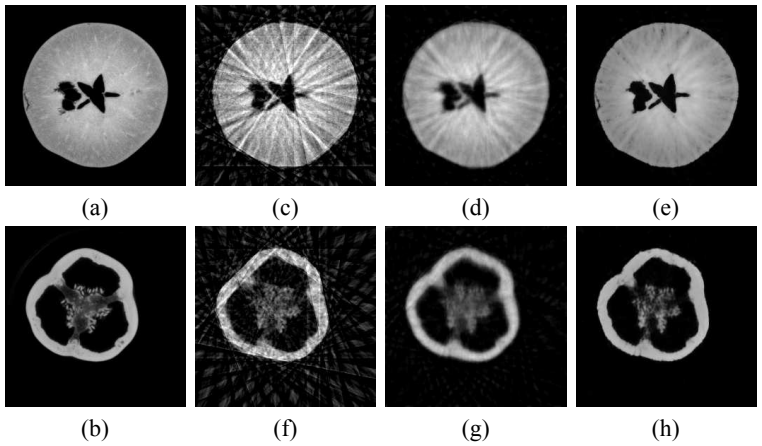

Figure 3.14: Ground truth images of an apple slice (a) and a bell pepper slice (b) and their reconstructions for 32 projections made with FBP (c and f), SIRT (d and g) and NN-hFBP (e and h).

of the apple, this image can certainly be used for the detection of holes. Further increasing the number of projections naturally leads to a better reconstruction quality. Fig. 3.16 shows the reconstruction times of FBP with and without the rebinning time, SIRT and NN-hFBP. NN-hFBP is 16 to 28 times faster than SIRT and 3 to 9 times faster than FBP with rebinning time but slower than FBP without the rebinning. Therefore it can be concluded that the long reconstruction time of FBP is caused by rebinning from a fan-beam to a parallel-beam geometry. The overhead time due to the rebinning step scales linearly with the number of projections. Furthermore, the training time of the NN-hFBP has not been taken into account since the NN-hFBP will mainly be used for inspection of a large number of samples, for which the training phase can be done in advance. Once the network is trained, similar samples can be scanned very fast.

3.3.2 Real Data Experiment

To test the performance on real X-ray data, a mock-up was built for an inline scanning environment where the sample rotates and translates at the same time, closely mimicking an inline environment with a conveyor belt [20]. Specifications of the scanning geometry are given in 3.1. The positions at which projections were taken on the conveyor belt ranged from -250 mm to 250 mm relative to the central ray and intermittent projections were acquired at positions so that the angles were equiangularly distributed.
With this mock-up, five walnuts were scanned. For each walnut, 512 projections

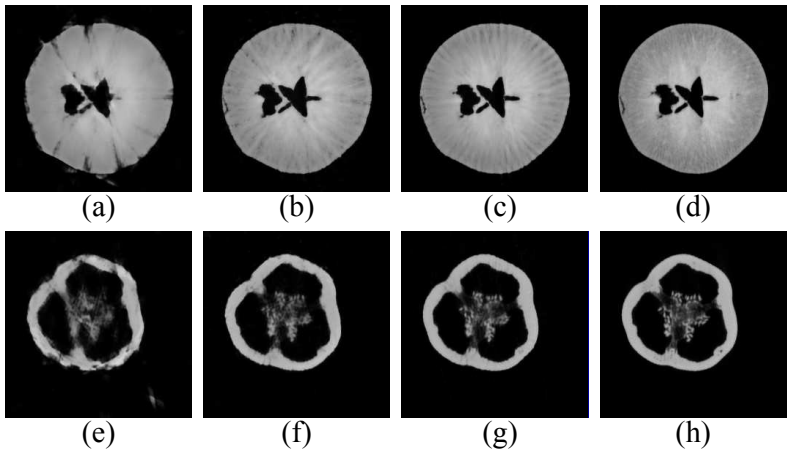

Figure 3.15: NN-hFBP reconstructions of the apple and bell pepper slices of Fig. 3.14 for 16 (a and e), 32 (b and f), 64 (c and g) and 128 (d and h) projections.

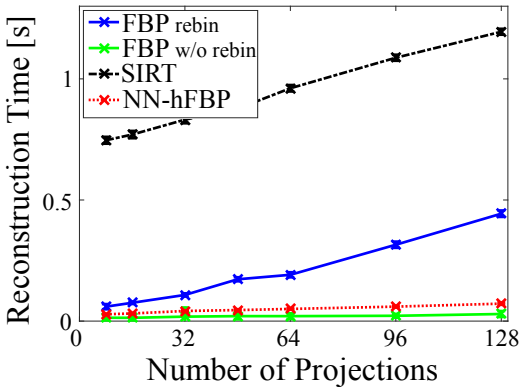

Figure 3.16: Reconstruction times of FBP (with and without rebinning time included), SIRT and NN-hFBP for apples with 256×256 reconstruction pixels.

were taken. Based on the 512 projections, 400×400 pixel reconstructions of 30 slices around the central slices were made with the SIRT algorithm. The reconstructed images were used to train the NN-hFBP. The network was trained with 300.000 pixels chosen from 90 images obtained from three training walnuts. Validation was done on 10.000 pixels of 30 images. The results were obtained from 10 images of the last remaining walnut dataset. A subset of the available projections was used and the reconstruction quality of FBP, SIRT and NN-hFBP as a function of the number of projections was compared.
Fig. 3.17 shows the quality of the FBP, SIRT and NN-hFBP reconstructions based on the real data acquired from the walnuts, in terms of the RMSE (a,b), MAD (c) and FSIM (d). As can be observed from these plots, the NN-hFBP outperforms the FBP method, independent of the number of projections. For less than 48 projections, the SIRT algorithms creates however better reconstructions than the NN-hFBP. This might be due to the limited training data available. The reconstruction quality of the NN-hFBP is highly dependent on the amount and quality of the training data. Fig. 3.18 shows the reconstruction time of FBP with and without rebinning time, SIRT and NN-hFBP. Here, we see again that the NN-hFBP algorithm is faster than FBP with rebinning but slower than FBP without rebinning. Despite its lower reconstruction quality than SIRT for a low number of projections, it is still much faster than SIRT. It is therefore better suited for implementation in an inline environment where speed is critical. Fig. 3.19 shows the reconstructed walnut slices from 32 and 128 projections with the different reconstruction algorithms. The NN-hFBP manages to remove the background artifacts and increase the signal-to-noise ratio of the reconstructions (2.65, 4.25 and 4.87 for reconstructions made with 32 projections with FBP, SIRT and NN-hFBP, respectively) while preserving the important features of the walnuts.

3.4 Conclusion

The NN-hFBP introduced in this work is a fast reconstruction method suitable to inline inspection where only a limited number of projections are available. Our method works directly on the fan-beam data, without the need for rebinning to parallel beam data. Simulation and real data studies showed that NN-hFBP outperforms the conventional FBP with respect to image quality. NN-hFBP is an order of magnitude faster than SIRT and for at least 48 projections, it also outperforms the SIRT algorithm in terms of reconstruction quality. The reconstruction time is approximately 200 ms for a reconstruction of 400×400 pixels from 128 projections when the forward and backprojection are calculated on an NVIDIA GeForce GTX 580 GPU with the ASTRA Toolbox.

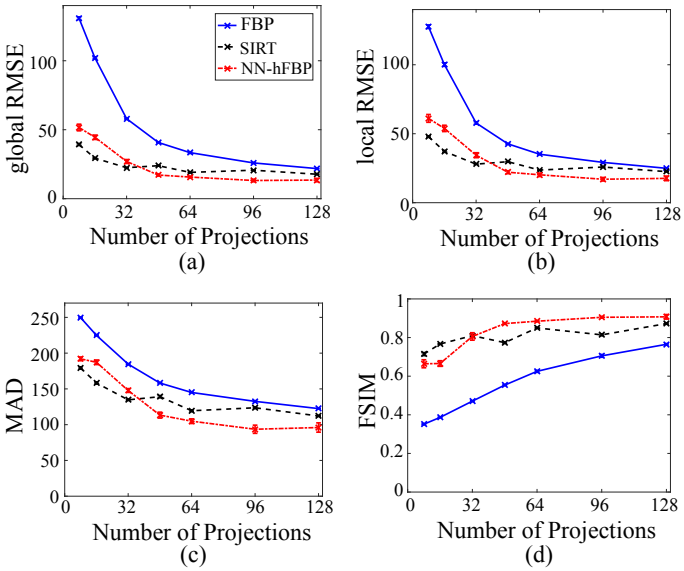

Figure 3.17: Evaluation of the FBP, SIRT and NN-hFBP reconstruction algorithms for walnuts with the (a) global RMSE, (b) local RMSE, (c) MAD and (d) FSIM.

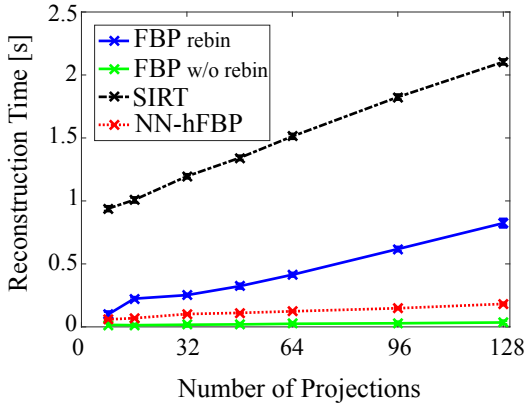

Figure 3.18: Reconstruction times of FBP (with and without rebinning time included), SIRT and NN-hFBP for walnuts with 400×400 reconstruction pixels.

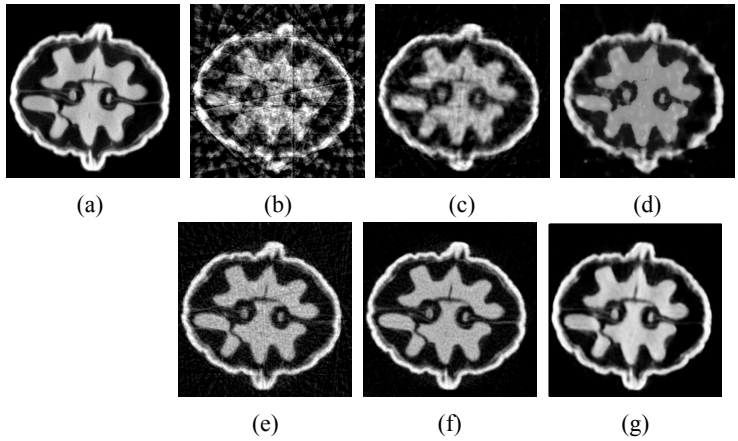

Figure 3.19: Ground truth image (a) of a walnut and reconstructions made with FBP (b), SIRT (c) and NN-hFBP (d) from 32 projections and FBP (e), SIRT (f) and NN-hFBP (g) from 128 projections.

Appendix A: hFBP algorithm for inline inspection with a constant rotation speed

1. **Discrete Hilbert Transform**

$$p_{\mathrm{H}}^{\mathrm{inl}}(u_i, h_j) = \frac{\Delta_u \sqrt{t_{i,j}^2 + D^2}}{\pi} \sum_{\tau} \frac{p^{\mathrm{inl}}(u_i - \tau, h_j)}{\tau \sqrt{(t_{i,j} - \tau)^2 + D^2}}. \tag{3.20}$$

2. **Differential by central difference**

$$p_{\mathrm{F}_0}^{\mathrm{inl}}(u_i, h_j) = \frac{\sqrt{D^2 + t_{i,j}^2}}{D + \omega(DSO - h_j t_{i,j})} \left(\frac{p_{\mathrm{H}}^{\mathrm{inl}}(u_i, h_{j+1}) - p_{\mathrm{H}}^{\mathrm{inl}}(u_i, h_{j-1})}{2\Delta_h} \right) + \frac{\sqrt{D^2 + t_{i,j}^2}(D + \omega(D^2 + t_{i,j}^2))}{D^2 + \omega D(DSO - h_j t_{i,j})} \left(\frac{p_{\mathrm{H}}^{\mathrm{inl}}(u_{i+1}, h_j) - p_{\mathrm{H}}^{\mathrm{inl}}(u_{i-1}, h_j)}{2\Delta_u} \right). \tag{3.21}$$

where Δ_h is the sampling grid interval with respect to h and Δ_u the sampling grid interval with respect to u.

3. **Interpolation** of u and h

4. **Backprojection**
   The values at pixels (x, y) with polar coordinates (r, ϕ) are then reconstructed by:
   $$f(x,y) = \frac{\Delta_h}{8\pi} \sum_m p^{\text{inl}}_{\text{F}_0}(u_m, h_m), \tag{3.22}$$
   where u_m is the detector coordinate at projection h_m where the ray through pixel (x, y) hits the detector.

Appendix B: Reformulation of the hFBP

In this appendix, we will reformulate the reconstruction formula for an inline hFBP reconstruction Eq. 3.11 so that it fits the form of Eq. 3.17:

$$f(r,\phi) = \sum_\tau f_1(\tau) I_1(u-\tau) + f_2(\tau) I_2(u-\tau). \tag{3.23}$$

Then it will be possible to use the hFBP in a neural network to create the NN-hFBP. To start with, after discretization, the reconstruction formula of the hFBP for inline inspection with a constant rotation speed Eq. 3.11 can be written in full as:

$$\begin{aligned} f(r,\phi) = \frac{\Delta_h}{16\pi} \sum_{h_j \in H} \sqrt{D^2 + t_j^2} \cdot \Bigg[\left(\frac{(D + \omega(D^2 + t_j^2))}{D + \omega(DSO - h_j t_j)} \right) \frac{1}{D\Delta_u} \cdot \\ \sum_\tau \left(\frac{\sqrt{(t_j^{+\Delta_u})^2 + D^2}\, p^{\text{inl}}(u + \Delta_u - \tau, h_j)}{\tau \sqrt{(t_j^{+\Delta_u} - \tau)^2 + D^2}} - \frac{\sqrt{(t_j^{-\Delta_u})^2 + D^2}\, p^{\text{inl}}(u - \Delta_u - \tau, h_j)}{\tau \sqrt{(t_j^{-\Delta_u} - \tau)^2 + D^2}} \right) \\ + \frac{1}{D + \omega(D \cdot SO - h_j t_j)} \frac{1}{\Delta_h} \\ \sum_\tau \left(\frac{\sqrt{t_{j+1}^2 + D^2}\, p^{\text{inl}}(u - \tau, h_{j+1})}{\tau \sqrt{(t_{j+1} - \tau)^2 + D^2}} - \frac{\sqrt{t_{j-1}^2 + D^2}\, p^{\text{inl}}(u - \tau, h_{j-1})}{\tau \sqrt{(t_{j-1} - \tau)^2 + D^2}} \right) \Bigg]. \end{aligned} \tag{3.24}$$

where H is the set of all displacement values h, $t_j = u - h_j$, $t_j^{-\Delta_u} = u - \Delta_u - h_j$ and $t_j^{+\Delta_u} = u + \Delta_u - h_j$. To implement this reconstruction method into the NN-FBP,

Eq. 3.24 is reformulated into Eq. 3.23 so that the first matrix multiplication of the ANN, the input nodes I_1 and I_2 times the weights $\boldsymbol{w_{1i}}$ and $\boldsymbol{w_{2i}}$ of Fig. 3.5, can be replaced by an hFBP reconstruction. In the NN-FBP, the same filters are used to reconstruct every pixel, independent of the angular position of the projection. Therefore, from the two terms in Eq. 3.24, two position and angle independent filters are derived:

$$f_1(\tau) = \frac{\Delta_h}{16\pi\tau D\Delta_u}, \tag{3.25}$$

$$f_2(\tau) = \frac{\Delta_h}{16\pi\tau\Delta_h}. \tag{3.26}$$

The remaining input of the neural network is then defined by two datavectors of size N:

$$I_1(u-\tau) = \sum_{h_j \in H} \left(\frac{a(j)p^{\mathrm{inl}}(u+\Delta_u-\tau, h_j)}{\sqrt{(t_j'^{+\Delta_u}-\tau)^2+D^2}} - \frac{b(j)p^{\mathrm{inl}}(u-\Delta_u-\tau, h_j)}{\sqrt{(t_j^{-\Delta_u}-\tau)^2+D^2}} \right), \tag{3.27}$$

$$I_2(u-\tau) = \sum_{h_j \in H} \left(\frac{c(j)p^{\mathrm{inl}}(u-\tau, h_{j+1})}{\sqrt{(t_{j+1}-\tau)^2+D^2}} - \frac{d(j)p^{\mathrm{inl}}(u-\tau, h_{j-1})}{\sqrt{(t_{j-1}-\tau)^2+D^2}}) \right), \tag{3.28}$$

with

$$a(j) = \frac{(D+\omega(D^2+t_j^2))}{D+\omega(DSO-h_jt_j)} \sqrt{\frac{D^2+t_j^2}{(t_j^{+\Delta_u})^2+D^2}}, \tag{3.29}$$

$$b(j) = \frac{(D+\omega(D^2+t_j^2))}{D+\omega(DSO-h_jt_j)} \sqrt{\frac{D^2+t_j^2}{(t_j^{-\Delta_u})^2+D^2}}, \tag{3.30}$$

$$c(j) = \frac{\sqrt{D^2+t_j^2}\sqrt{D^2+t_{j+1}^2}}{D+\omega(DSO-h_jt_j)}, \tag{3.31}$$

$$d(j) = \frac{\sqrt{D^2+t_j^2}\sqrt{D^2+t_{j-1}^2}}{D+\omega(DSO-h_jt_j)}. \tag{3.32}$$

So that Eq. 3.24 can be rewritten as:

$$f(r,\phi) = \sum_{\tau} f_1(\tau)I_1(u-\tau) + f_2(\tau)I_2(u-\tau). \tag{3.33}$$

To generate the data vectors for a certain pixel, first the corresponding detector pixel is defined for every projection. We further on denote this pixel as the central

detector pixel. Then, the two datavectors I_1 and I_2 are generated as described by Eq. 3.27 and Eq. 3.28. For both datavectors, the projection data is shifted so that the central pixel is at the center of the detector as explained in [22] and the data from all projection angles is summed.

References

[1] R. P. Haff and N. Toyofuku, "X-ray detection of defects and contaminants in the food industry," *Sensing and Instrumentation for Food Quality and Safety*, vol. 2, no. 4, pp. 262–273, 2008.

[2] M. Van Dael, S. Lebotsa, E. Herremans, P. Verboven, J. Sijbers, U. Opara, P. Cronje, and B. Nicolaï, "A segmentation and classification algorithm, for online detection of internal disorders in citrus using X-ray radiographs," *Postharvest Biol Technol*, vol. 112, pp. 205–14, 2016.

[3] M. Iovea, M. Neagu, B. Stefanescu, G. Mateiasi, A. L. Clarke, M. Vieyra, and P. I. Nicholson, "Time Delay Integration detector based solution for Industrial X-Ray NDT Inspection," in *11th European Conference on Non-Destructive Testing (ECNDT)*, 2014.

[4] Y. An and G. S. Schajer, "Geometry-based CT scanner for measuring logs in sawmills," *Comput Electron Agric*, vol. 105, pp. 66–73, July 2014.

[5] W. Thompson, W. R. B. Lionheart, E. Morton, M. Cunningham, and R. D. Luggar, "High speed imaging of dynamic processes with a switched source X-ray CT system ," *Meas. Sci. Technol.*, vol. 5, no. 26, 2015.

[6] J. Warnet, V. Titarenko, E. Kiraci, A. Attridge, W. Lionheart, P. Withers, and M. Willems, "Towards in-process X-ray CT for dimensional metrology," *Measurement Science and Technology*, vol. 27, no. 3, p. 035401, 2016.

[7] I. Uroukov and R. Speller, "A preliminary approach to intelligent X-ray imaging for baggage inspection at airports," *Signal Process*, vol. 4, pp. 1–11, 2015.

[8] R. P. Haff, T. C. Pearson, and E. S. Jackson, "One Dimensional Linescan X-ray Detection of Pits in Fresh Cherries," *American Journal of Agricultural Science and Technology*, vol. 1, pp. 18–26, 2013.

[9] J. Kwon, J. Lee, and W. Kim, "Real-time detection of foreign objects using X-ray imaging for dry food manufacturing line," in *IEEE International conference on Consumer Electronics, ISCE*, pp. 1–4, 2008.

[10] J. Maier, C. Leinweber, S. Sawall, H. Stoschus, F. Ballach, T. Müller, M. Hammer, R. Christoph, and M. Kachelrieß, "Simulation-based artifact correction (SBAC) for metrological computed tomography," *Meas. Sci. Technol.*, vol. 28, no. 6, p. 065011, 2017.

[11] A. Jansson and L. Pejryd, " A dual-energy approach for improvement of the measurement consistency in computed tomography ," *Meas. Sci. Technol.*, vol. 27, no. 11.

[12] R. S. Bradley, "Estimation of bias and variance of measurements made from tomography scans," *Meas. Sci. Technol.*, vol. 27, no. 9, p. 095402, 2016.

[13] J. J. Lifton, A. A. Malcolm, and J. W. McBride, "An experimental study on the influence of scatter and beam hardening in X-ray CT for dimensional metrology," *Meas. Sci. Technol.*, vol. 27, no. 1, p. 015007, 2016.

[14] A. du Plessis, S. G. le Roux, and A. Guelpa, "Comparison of medical and industrial X-ray computed tomography for non-destructive testing," *CSNDT&E*, vol. 6, pp. 17–25, Nov. 2016.

[15] E. Y. Sidky, Y. Zou, and X. Pan, "Volume image reconstruction from a straight-line source trajectory," in *Nuclear Science Symposium Conference Record, IEEE*, vol. 5, pp. 2441–2444, 2005.

[16] L. Zhang, H. Gao, J. Cheng, Z. Chen, and Y. Xing, "Feasibility study of applying X-ray tomographic imaging with a straight-line trajectory scan to security inspection," in *Nuclear Science Symposium Conference Record, IEEE*, pp. 1274–1277, 2008.

[17] H. Zhang, L. Wang, B. Yan, L. Li, X. Xi, and L. Lu, "Image reconstruction based on total-variation minimization and alternating direction method in linear scan computed tomography," *Chin Phys B*, vol. 22, p. 078701, July 2013.

[18] E. Janssens, L. F. Alves Pereira, J. De Beenhouwer, I. R. Tsang, M. Van Dael, P. Verboven, B. Nicolai, and J. Sijbers, "Fast inline inspection by Neural Network Based Filtered Backprojection: Application to apple inspection," *CSNDT&E*, vol. 6, pp. 14–20, 2016.

[19] L. F. Alves Pereira, E. Janssens, M. Van Dael, P. Verboven, B. Nicolai, G. D. C. Cavalcanti, I. R. Tsang, and J. Sijbers, "Fast X-ray Computed Tomography via Image Completion," in *6th Conference on Industrial Computed Tomography*, (Wels, Austria), 2016.

[20] T. De Schryver, J. Dhaene, M. Dierick, M. N. Boone, E. Janssens, J. Sijbers, M. Van Dael, P. Verboven, B. Nicolai, and L. Van Hoorebeke, "In-line NDT with X-ray CT combining sample rotation and translation," *NDT&E International*, vol. 84, pp. 89–98, 2016.

[21] D. M. Pelt, J. Sijbers, and K. J. Batenburg, "Fast tomographic reconstruction from highly limited data using artificial neural networks," in *1st International Conference on Tomography of Materials and Structures*, pp. 109–112, 2013.

[22] D. M. Pelt and K. J. Batenburg, "Fast Tomographic Reconstruction from Limited Data Using Artificial Neural Networks," *IEEE Trans Image Process*, vol. 22, no. 12, pp. 5238–5251, 2013.

[23] J. You and G. L. Zeng, "Hilbert Transform Based FBP Algorithm for Fan-Beam CT Full and Partial Scans," *IEEE Trans Med Imaging*, vol. 26, no. 2, pp. 190–9, 2007.

[24] J. You, G. Zeng, and Z. Liang, "FBP Algorithms for Attenuated Fan-Beam Projections," *Inverse Problems*, vol. 21, no. 5, 2005.

[25] A. K. Yadav and S. S. Chandel, "Solar radiation prediction using Artificial Neural Network techniques: A review," *Renew Sustainable Energy Rev*, vol. 33, pp. 772–781, May 2014.

[26] A. K. Bhatt, D. Pant, and R. Singh, "An analysis of the performance of Artificial Neural Network technique for apple classification," *AI Soc*, vol. 29, pp. 103–111, May 2014.

[27] H. Zhu, X. Chen, W. Dai, K. Fu, Q. Ye, and J. Jiao, "Orientation robust object detection in aerial images using deep convolutional neural network," in *IEEE International Conference on Image Processing (ICIP)*, pp. 3735–3739, 2015.

[28] C. Lorenz, A. S. Ferraudo, and L. Suesdek, "Artificial Neural Network applied as a methodology of mosquito species identification," *Acta Trop*, vol. 152, pp. 165–169, Dec. 2015.

[29] F. Rosenblatt, *Principles of neurodynamics: perceptrons and the theory of brain mechanisms*. Spartan Books, 1962.

[30] D. E. Rumelhart, G. E. Hinton, and R. J. Williams, "Learning representations by back-propagating errors," *Nature*, vol. 323, pp. 533–536, 1986.

[31] M. T. Hagan and M. B. Menhaj, "Training feedforward networks with the Marquardt algorithm," *IEEE Trans Neural Netw*, vol. 5, no. 6, pp. 989–993, 1994.

[32] S. Karsoliya, "Approximating Number of Hidden layer neurons in Multiple Hidden Layer BPNN Architecture," *International Journal of Engineering Trends and Technology*, vol. 3, no. 6, pp. 714–717, 2012.

[33] K. Gnana Sheela and S. N. Deepa, "Review on Methods to Fix Number of Hidden Neurons in Neural Networks," *Math Probl Eng*, vol. 2013, 2013.

[34] P. Paschalis, N. D. Giokaris, A. Karabarbounis, G. K. Loudos, D. Maintas, C. N. Papanicolas, V. Spanoudaki, C. Tsoumpas, and E. Stiliaris, "Tomographic image reconstruction using Artificial Neural Networks," *Nucl Instr Meth Phys Res A*, vol. 527, pp. 211–215, July 2004.

[35] R. Cierniak, "A 2D approach to tomographic image reconstruction using a Hopfield-type neural network.," *Artif Intell Med*, vol. 43, pp. 113–25, June 2008.

[36] R. Cierniak, "New neural network algorithm for image reconstruction from fan-beam projections," *Neurocomputing*, vol. 72, pp. 3238–3244, Aug. 2009.

[37] R. Cierniak, "Neural network algorithm for image reconstruction using the "grid-friendly" projections," *Australas Phys Eng Sci Med*, vol. 34, pp. 375–389, Sept. 2011.

[38] X. F. Ma, M. Fukuhara, and T. Takeda, "Neural network CT image reconstruction method for small amount of projection data," *Nucl Instr Meth Phys Res A*, vol. 449, pp. 366–377, July 2000.

[39] M. Teranishi, "Improved neural network tomography by initial learning with coarse reconstructed image," *Neurocomputing*, vol. 172, pp. 399–404, Aug. 2015.

[40] E. C. Larson and D. M. Chandler, "Most apparent distortion: full-reference image quality assessment and the role of strategy," *J Electron Imaging*, vol. 19, no. 1, pp. 011006–1–21, 2010.

[41] X. Zhang, J. Wang, and L. Xing, "Metal artifact reduction in X-ray computed tomography (CT) by constrained optimization," *Medical Physics*, vol. 38, no. 2, pp. 701–711, 2011.

[42] W. van Aarle, W. J. Palenstijn, J. Cant, E. Janssens, F. Bleichrodt, A. Dabravolski, J. De Beenhouwer, K. J. Batenburg, and J. Sijbers, "Fast and flexible X-ray tomography using the ASTRA toolbox," *Optics Express*, vol. 24, no. 22, pp. 25129–25147, 2016.

[43] W. J. Palenstijn, K. J. Batenburg, and J. Sijbers, "Performance improvements for iterative electron tomography reconstruction using graphics processing units (GPUs)," *J Struct Biol*, vol. 176, no. 2, pp. 250–253, 2011.

[44] W. van Aarle, W. J. Palenstijn, J. De Beenhouwer, T. Altantzis, S. Bals, K. J. Batenburg, and J. Sijbers, "The ASTRA Toolbox: a platform for advanced algorithm development in electron tomography," *Ultramicroscopy*, vol. 157, pp. 35–47, 2015.

4

Inline Crack Detection

Contents

4.1 Introduction

An SVS adapter is a small medical device that is one of the several parts of which certain syringes are composed. During production, an ultrasonic welding process is performed that welds two plastic parts together [1, 2]. However, at the welding surface, undesired cracks can appear. Detection of these cracks is essential for a safe functioning of the syringe. Unfortunately, the cracks are not visible from the outside. Currently, they are detected by a leak detection system that puts pressure on the final product after assembly and monitors the decay. This method has some major disadvantages. Since the pressure test can only be applied on the assembled syringe, all the other good components of the syringe are also thrown away when a leakage is detected. The technique is furthermore very time consuming and the detection rate is at a maximum around 80%.
X-ray imaging and tomography can offer an alternative for the detection of cracks. Many algorithms are developed over the year that aim to improve the detection of welding defects on radiographic data [3, 4, 5] and on reconstructed data [6]. In case of the SVS adapters, the defects of interest can be very small, making them appear invisible on the projection data. Considering inspection on the reconstructed data, X-ray inspection is only profitable if it can be applied on every adapter separately before the assembly process. This puts high requirements on the reconstruction and inspection time.
In this work, a fast, accurate and flexible inspection method is developed on the reconstruction data for the detection of cracks in SVS adapters that can be inserted in the inline production process of the adapters. During the inspection, the adapters are translating on a conveyor belt in specific holders where several samples are stacked behind each other. When the holder reaches the central position on the conveyor belt between the source and detector, the conveyor belt stops, the adapters start rotating and projections from a limited number of different projection directions are acquired. After the acquisition, a two-step detection algorithm is applied on the data. In a first step, an adapted version of the NN-hFBP [7] algorithm discussed in Chapter 3 is applied on the inline inspection data to generate reconstructions of the samples of sufficient quality. In the second step, when the reconstructions are performed, an inspection method is applied on the reconstructed images that classifies the data into SVS-adapters with and without cracks. The major advantages of the detection method are its speed, its ability to be incorporated in the manufacturing pipeline and its direct application on the SVS-adapters before the assembly of the syringe. This way, when a crack is present, only the adapter has to be replaced.
The remainder of this chapter is divided as follows: in the next section, the applied method is described. The method is subdivided in the reconstruction part and the

actual detection part. In Section 4.3 the performed experiments are shown and the chapter ends with a general conclusion and some remarks for further improvement of the method in Section 4.4.

4.2 Methods

In this section, the followed methodology for crack detection is discussed. The detection process consists of two subsequent steps: in the first step, a reconstruction is made of the adapters with a limited number of projections. The reconstruction algorithm is an adapted version of the NN-hFBP algorithm described in the previous chapter. In Section 4.2.1, the algorithm is adapted to the scanning geometry of the adapters. Secondly, in Section 4.2.2, the crack detection algorithm that will be applied on the inline reconstructions, is explained.

4.2.1 NN-hFBP for crack reconstruction

In the production line of SVS adapters, an X-ray inspection method can be installed for detection of cracks inside the samples. The scanning geometry is however slightly different as in the previous chapter. The adapters are stacked in groups of five in a multi-object holder. This holder translates on a conveyor belt towards the X-ray source and detector and stops at the central position. At that position, several projections are taken with a rotation of the five samples in between. The number of projections is limited by the maximal acquisition time, which is limited in an inline process. When all projection data is acquired, the sample holder translates further on the conveyor belt and out of the field of view, while another holder with new samples arrives. Since five samples are scanned at the same time, their acquisition geometry is slightly different, dependent on their position on the sample holder. Consequently, five different neural networks should be trained to reconstruct the data of the corresponding positions. Each network is linked to a certain displacement value H of the object position compared to the central position between source and detector. The value H is however constant for a neural network, opposed to the displacement h of the NN-hFBP in Chapter 3 which changes for every projection. Fig. 4.1 shows the scanning geometry at projection angle β. In the figure, D is the distance between the source and detector and SO is the source-object distance.

As in Section 3.2.1, the scanning geometry can be described by two parameters u and β, where u is the detector position and β the rotation angle of the object. The parallel beam coordinates (l, θ) corresponding to the detector pixel and projection angles of the equivalent parallel projection can again be formulated in terms of u

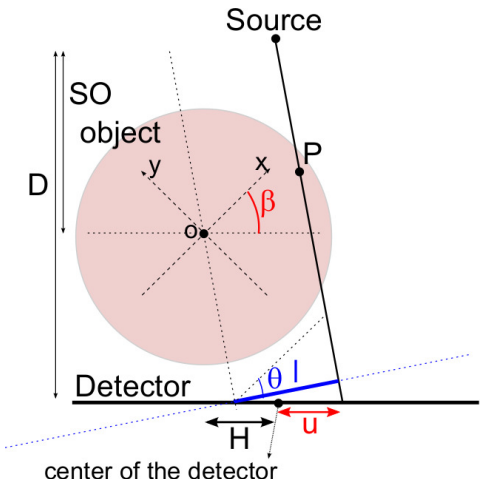

Figure 4.1: Inline acquisition geometry of the adapters

and β:

$$l = \frac{uSO + HD}{\sqrt{D^2 + u^2}}. \tag{4.1}$$

$$\theta = \beta + \arctan\frac{u}{D}. \tag{4.2}$$

In this case, the Hilbert transform of the data can simply be described by the Hilbert transform of fan-beam data with a flat panel detector as written by You et al. in [8] and a similar equation as Eq. 3.6 between the Hilbert transform of the inline data and the Hilbert transform of the parallel beam projection data holds:

$$p_{\mathrm{H}}^{\mathrm{moh}}(u,h) = p_{\mathrm{H}}\left(\frac{uSO + HD}{\sqrt{D^2 + u^2}}, \beta + \arctan\frac{u}{D}\right). \tag{4.3}$$

In Eq. 4.3, p_{H} is the Hilbert transformed parallel beam projection data and $p_{\mathrm{H}}^{\mathrm{moh}}$ is the Hilbert transform of the projection data of the multi-object holder. To adapt the NN-hFBP to the specific geometry of the holder, the same procedure has to be followed as in the previous chapter. First, the partial derivatives of $p_{\mathrm{H}}^{\mathrm{moh}}$ with respect to u and β are calculated based on Eq. 4.3:

$$\frac{\partial p_{\mathrm{H}}^{\mathrm{moh}}}{\partial u}(u,\beta) = \frac{D^2 SO - DHu}{\sqrt{(D^2+u^2)^3}} \frac{\partial p_{\mathrm{H}}(l,\theta)}{\partial l} + \frac{D}{D^2+u^2} \frac{\partial p_{\mathrm{H}}(l,\theta)}{\partial \theta}. \tag{4.4}$$

$$\frac{\partial p_{\mathrm{H}}^{\mathrm{moh}}}{\partial \beta}(u,\beta) = \frac{\partial p_{\mathrm{H}}(l,\theta)}{\partial \theta}. \tag{4.5}$$

After solving the system of equations for $\frac{\partial p_{\mathrm{H}}(l,\theta)}{\partial l}$, the reconstruction formula of the hFBP for inline inspection with the multi-object holder is formulated as:

$$\begin{aligned} f(r,\phi) &= \frac{1}{8\pi} \int_0^{2\pi} \frac{\partial p_H}{\partial l} d\theta, \\ &= \frac{1}{8\pi} \int_0^{2\pi} \frac{\sqrt{D^2+u^2}}{DSO - Hu)} \left[\frac{\partial p_{\mathrm{H}}^{\mathrm{moh}}}{\partial \beta}(u,\beta) + \frac{(D^2+u^2)}{D} \frac{\partial p_{\mathrm{H}}^{\mathrm{moh}}}{\partial u}(u,\beta) \right] \mathrm{d}\theta. \end{aligned} \tag{4.6}$$

Here, f is the reconstructed image and u corresponds to the detector pixel where the ray through (r,ϕ) hits the detector at projection angle β. To perform the reconstruction, interpolation in u and β is required to obtain the values corresponding to the parallel projection angles θ.
In a last step, the hFBP reconstruction algorithm should be incorporated in the NN-FBP algorithm of Pelt [9, 10]. Therefore, discretization of Eq. 4.6 is necessary and the reconstruction equation is written as the convolution of two datavectors, which will serve as the input of the neural network, and two filters. The same procedure is followed as in Section 3.2.3 to derive the NN-hFBP. Since also here interpolation of the data is required, we again work with an heuristic approach where the interpolation is omitted.

4.2.2 Crack detection

As second part of the crack detection method, a classification algorithm is required to label the adapters as good or broken. In this section, a basic classification algorithm is described with which acceptable results can be obtained. At this point, the algorithm only takes the reconstructed slices into account at the part of the assembly surface where the adapter has the shape of a disk. Most of the cracks are visible on these slices.
The classification algorithm consists of five different steps that will now be described in detail:

1. In a first step, the reconstructed image is transformed into polar coordinates. This way, the image can easily be inspected radially, which is of interest since the cracks mainly have a more circular shape.

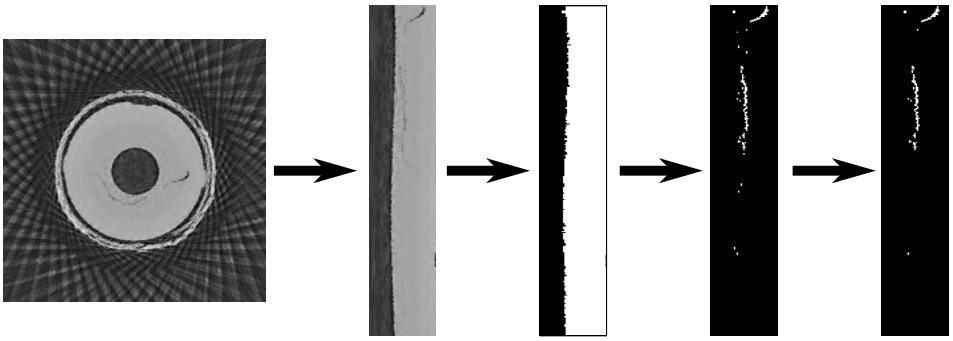

Figure 4.2: Steps 1–4 of the classification algorithm.

2. On the image in polar coordinates, the region of the adapter is marked.

3. In the region of the adapter, the pixels which have a value less than a predefined threshold are highlighted. For the selection of the threshold, reconstructions of adapters without cracks are considered. The mean grey value as well as the mean of the standard deviations over circles with increasing radii are selected and the threshold is defined as the mean grey value minus 4 times the standard deviation.

4. For each of the highlighted pixels, a $3\times3\times3$ region is studied around the pixel by taking the previous and next slice into account. The number of highlighted pixels in this region should be at least 4 to cathegorize the pixel as part of a crack.

5. Since cracks originate from the assembly surface, they are more likely to be detected in the images close to the surface. An adapter is labelled broken if a certain number of successive images have pixels that are classified as part of a crack. The number of successive images increases with increasing distance from the assembly surface.

Fig. 4.2 gives a visual representation of the first four steps of the classification algorithm. After application of the algorithm, the broken adapters can be removed from the conveyor belt to improve the quality of the final products.

4.3 Experiments and Results

In this section, the performance of the crack detection method is evaluated. The reconstruction step and the detection step are discussed separately. First, the

Table 4.1: Specifications scanning geometry.

	Projection Data
Detector pixels	1000
Detector pixel size	150μm
Translation distance [mm]	[-250, 250]
Object Detector distance	713.11mm
Source Object distance	792.94mm
Image pixels	20×200
Image pixel size	75μm

NN-hFBP is evaluated as an inline reconstruction algorithm that meets both an acceptable image quality and a limited reconstruction time. Then, based on the reconstructions acquired in the first step, the crack detection algorithm is evaluated.

4.3.1 NN-hFBP crack reconstruction

To use the NN-hFBP as an algorithm for inline crack detection of samples in a multi-object holder, it has to fulfill two important requirements: the reconstruction must be fast and the reconstruction quality should be sufficient to still detect the cracks. Obviously, the crack detection efficiency will increase with a larger number of projections, but that automatically also leads to a longer reconstruction time as well as a longer acquisition time. Therefore, a trade-off should be made between the two requirements.
To evaluate the performance of the NN-hFBP, 30 adapters with cracks of different (unknown) sizes were scanned by XRE nv. The samples were all scanned at the central position of the object holder, resulting in $H = 0$ in the algorithm. Similar experiments could however also be performed for $H \neq 0$. The adapters were scanned with 1500 projections on a detector of 668×1000 detector pixels. Because of the small cone angle, from each projection 50 slices were taken on which the algorithm was applied since no cone beam artefacts were visible. Specifications on the geometry are given in Table 4.1.

Before evaluating the reconstruction quality in function of the number of projections, a closer look is taken at the selection of the training pixels. The available adapters are subdivided into 20 adapters for training, five adapters for validation and five adapters for testing. Of these adapters, 1.000.000 pixels of 600 images were used for training and 10.000 pixels of 100 images for validation. Since in this application not the overall image quality is of interest but only the reconstruction

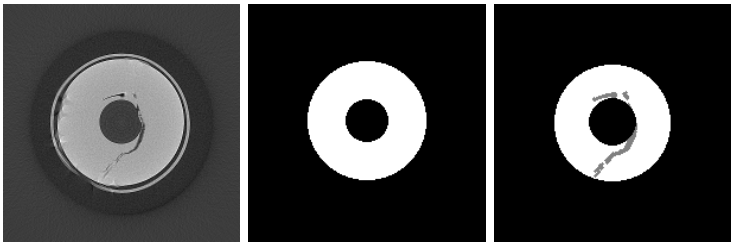

Figure 4.3: (a)Adapter slice, (b) the training disk and (c) a crack map

quality of the cracks, a smart selection of the training and validation pixels is of interest. Therefore, three different selection methods are compared based on the knowledge that the cracks mainly appear at the inner surface. In the first method, the pixels are randomly selected in the image. In the second method, the pixels are randomly selected on a disk with an inner radius of 18 pixels and an outer radius of 50 pixels. In the third method, for every image a crack map is constructed where the regions of the cracks have value 1 and the adapter region inside a radius of 50 pixels value 2. To select the number of pixels in an image, first the pixels which have value 1 on the crack image are considered and when all those pixels are chosen, the remainder of the pixels is chosen from the adapter pixels where the crack map has value 2. Fig. 4.3 shows an image, the disk of which pixels are chosen in the second case and its corresponding crack map. In Table 4.2, the RMSE in the crack region of the crack map and on the whole adapter region of the map (values 1+2) is given for different selection methods and different number of projections. For 25 and 50 projections, it is shown that a smarter selection method improves the RMSE in the crack region as well as the total RMSE. Fig. 4.4 shows reconstructions of two slices of two different adapters based on 50 projections with the three different training methods. It can be seen that there is a better contrast between the cracks and the adapters when training is performed with the crack maps.

In a second experiment, a trade-off is made between the reconstruction quality of the NN-hFBP and the reconstruction time based on the number of projections. Based on the results of the different selection methods, the NN-hFBP will further on be trained with the crack maps. Fig. 4.5 shows the RMSE on the crack regions of the crack map and on the whole crack map as function of the number of projections as well as the reconstruction time for 10 to 150 projections. The overall RMSE only slightly decreases when the number of projections is higher than 50, while

Table 4.2: RMSE in the crack and adapter region for different number of projections and different training methods.

	Random pixels	Disk	Crack Map
crack region 25 proj	$6.4275{\cdot}10^{-4}$	$6.4220{\cdot}10^{-4}$	$6.4156{\cdot}10^{-4}$
adapter 25 proj	$2.2108{\cdot}10^{-4}$	$2.2108{\cdot}10^{-4}$	$2.1798{\cdot}10^{-4}$
crack region 50 proj	$6.2946{\cdot}10^{-4}$	$6.2506{\cdot}10^{-4}$	$5.6711{\cdot}10^{-4}$
adapter 50 proj	$2.2160{\cdot}10^{-4}$	$2.1011{\cdot}10^{-4}$	$1.9522{\cdot}10^{-4}$
crack region 100 proj	$4.8019{\cdot}10^{-4}$	$4.7388{\cdot}10^{-4}$	$4.7729{\cdot}10^{-4}$
adapter 100 proj	$1.8501{\cdot}10^{-4}$	$1.8314{\cdot}10^{-4}$	$1.8554{\cdot}10^{-4}$

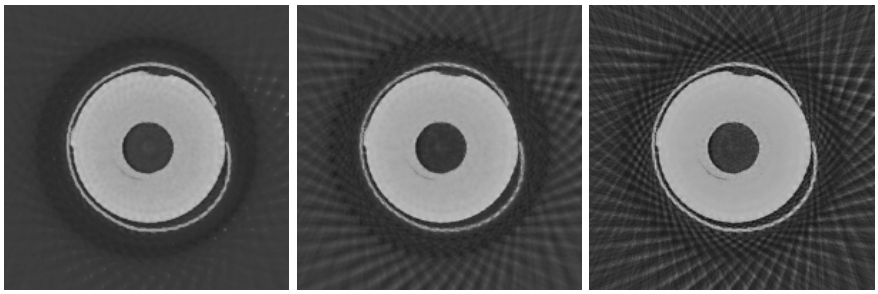

(a) random pixels **(b)** disk **(c)** crack map

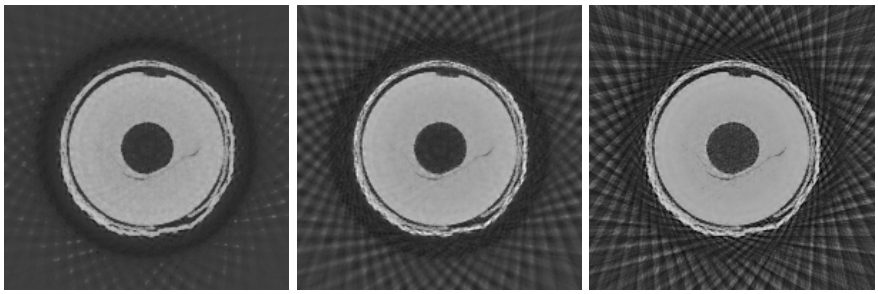

(d) random pixels **(e)** disk **(f)** crack map

Figure 4.4: NN-hFBP reconstructions of two adapter slices obtained with different training methods: random pixel selection, disk selection and crack map selection.

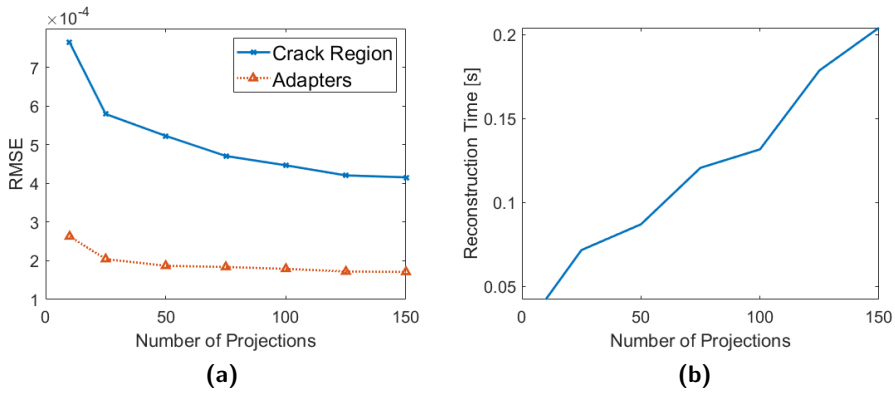

Figure 4.5: RMSE on the crack region and on the adapter region (a) and reconstruction time (b) in function of the number of projections

the RMSE in the crack region keeps improving when more projections are taken into account. As expected, the reconstruction time increases with the number of projections. Based on these two graphs, we chose 50 projections to perform the inline crack detection on since the total RMSE from here on only slightly improves and the reconstruction time is below 100ms. In Fig. 4.6 an FBP reconstruction of an adapter slice with 1500 projections is compared to NN-hFBP reconstructions of the same slice with an increasing number of projections. When 50 projections are used, the crack can clearly be detected.

4.3.2 Crack Detection

To evaluate the performance of the detection algorithm, four measures are used: the precision, accuracy, recall and specificity [11]. Their values can be calculated with the following formulas:

$$\text{precision} = \frac{\text{TP}}{\text{TP} + \text{FP}}, \tag{4.7}$$

$$\text{accuracy} = \frac{\text{TP+TN}}{\text{TP+TN+FP+FN}}, \tag{4.8}$$

$$\text{recall} = \frac{\text{TP}}{\text{TP+FN}}, \tag{4.9}$$

$$\text{specificity} = \frac{\text{TN}}{\text{TN+FN}}. \tag{4.10}$$

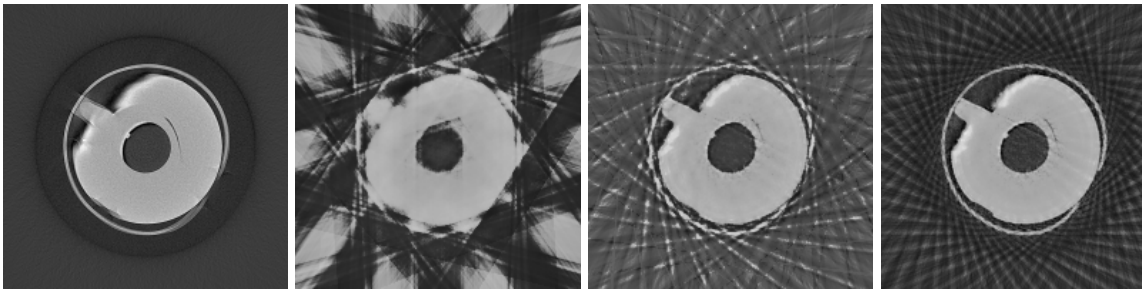

(a) **(b)** 10 proj **(c)** 25 proj **(d)** 50 proj

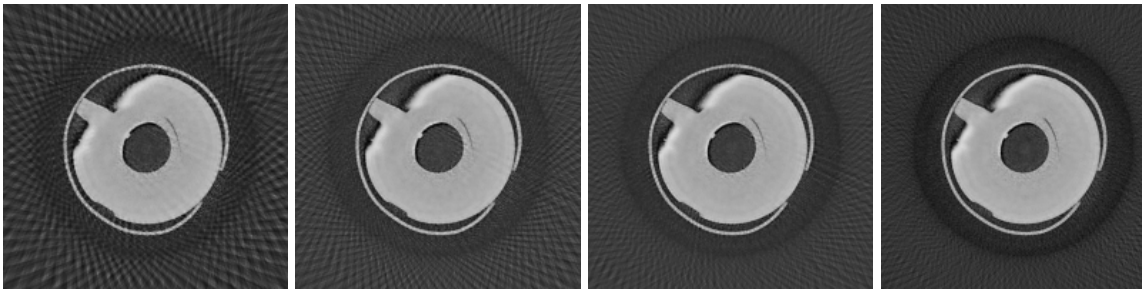

(e) 75 proj **(f)** 100 proj **(g)** 125 proj **(h)** 150 proj

Figure 4.6: a) Ground truth FBP reconstruction with 1500 projections, (b)-(h) NN-hFBP reconstructions of the same adapter slice with an increasing number of projections

Table 4.3: Precision, accuracy, recall, specificity and classification time of the classification algorithm after application on a high-quality dataset made with 1500 projections an on the reconstructed dataset with 50 projections.

	High-quality dataset	Inline reconstructions
precision	0.9643	0.8519
accuracy	0.9412	0.8038
recall	0.9310	0.7931
specificity	0.9130	0.7500
classification time [s]	0.1975	0.1975

In the equations, TP stands for True Positives, TN for True Negatives, FP for False Positive and FN for False Negatives. True Positives are the broken detectors that are classified as broken, true negatives are the good adapters that are classified as good, false positives are good adapters that are classified as broken and false negatives are broken adapters that are classified as good.
The algorithm is applied on a dataset of 51 adapters scanned by XRE with the same parameters as described in the previous section. Of the adapters, 29 contain a crack and 22 are good adapters and of each adapter 30 consecutive slices are inspected. Before the classification algorithm is applied on the reconstructed data, its performance is tested on high-quality reconstructions of the SVS adapters made with 1500 projection images. The results for the recall, accuracy, precision and specificity for application of the algorithm on both the high-quality dataset an on the inline reconstructed dataset are shown in Table 4.3.

Despite the large difference in amount of projection data, still 80% of the adapters are classified correctly and 79% of the adapters with cracks are detected on the inline reconstructed data. This value is similar to the percentage of cracks that can be detected with the currently used pressure tests. The advantage of this method is its applicability in the inline production process before the syringe is assembled, allowing the inspection of every adapter individually. The classification time of the algorithm is also given in Table 4.3. The time easily fits into the timeframe for inline inspection.
Despite the good results, it is always interesting to study the adapters that were detected incorrectly. For the high-quality dataset, two false negatives and one false positive was obtained. In Fig. 4.7, reconstruction images of the wrongly classified adapters are shown. Even through visual inspection, no crack can be detected in the false negative images. There is a high chance that the sizes of the cracks are of subpixel resolution in these adapters, making them impossible to detect with the algorithm. The last adapter is falsely detected as broken because the clear spot at the border of the inner circle moves towards the center of adapter, causing the

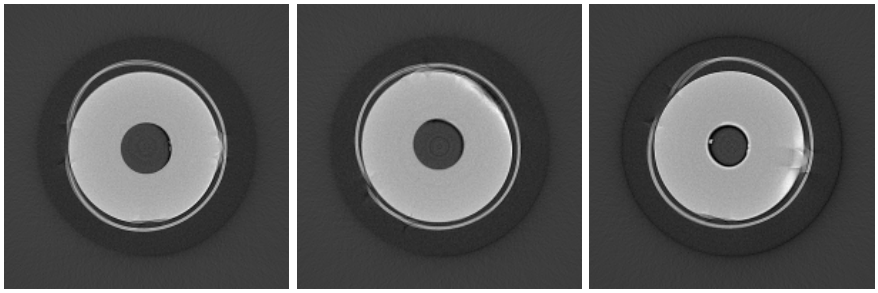

(a) FN **(b)** FN **(c)** FP

Figure 4.7: Images of wrongly classified adapters with the classification algorithm applied on the high-quality dataset

detection of crack pixels in the small region between the adapter and the small spot. This problem can be solved by a small adaptation of the algorithm.
With the inline dataset, 6 false negatives and 4 false positives are generated. Among them are the adapters that were also wrongly classified with the high-quality dataset. The other adapters are shown in Fig. 4.8. Here again, no cracks can be visually detected in the false negative adapters. The resolution of the NN-hFBP reconstruction with 50 projections is not high enough to visualize the cracks. Therefore, the algorithm cannot classify the adapters correctly. For the false positive adapters, artefacts that originate from the limited data are wrongly detected as cracks.

4.4 Conclusion

In this chapter, the feasibility of inline crack detection is demonstrated by a two-step detection procedure. First, 2D reconstructions of the adapter slices are made with a slightly altered NN-hFBP algorithm. Secondly, the reconstructed images are used for classification of the adapters with a basic classification algorithm. Both the reconstruction and classification can be performed very fast so they can be used for inline inspection purposes. At this point, the accuracy of the classification algorithm is 80%, which is equal to the accuracy of the offline pressure tests that are currently used. The two major advantages of the inline algorithm are the ability to fit the algorithm in the inline manufacturing line and the detection of cracks before the different components are assembled. Interesting topics for further research are extending the classification algorithm for all slices in the assembly region and the use of deep learning to classify the images automatically.

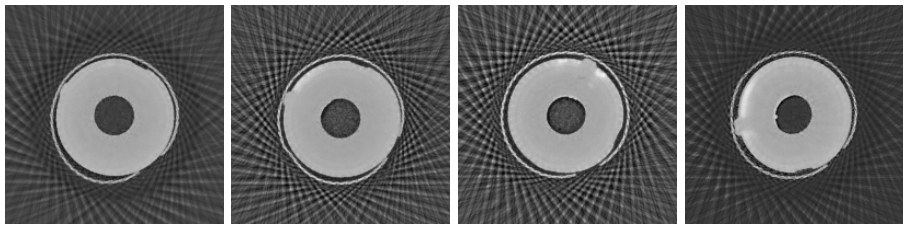

(a) FN **(b)** FN **(c)** FN **(d)** FN

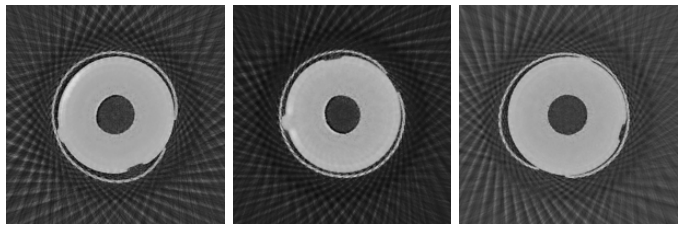

(e) FP **(f)** FP **(g)** FP

Figure 4.8: Images of wrongly classified adapters with the classification algorithm applied on the inline dataset

References

[1] V. K. Stokes, "Joining methods for plastics and plastic composites: An overview," *Polymer Engineering & Science*, vol. 29, no. 19, pp. 1310–1324, 1989.

[2] S. Ng, Z. Wang, and N. de Rooij, "Microfluidic connectors by ultrasonic welding," *Microelectronic Engineering*, vol. 86, no. 4-6, pp. 1354–1357, 2009.

[3] R. Vilar, J. Zapata, and R. Ruiz, "An automatic system of classification of weld defects in radiographic images," *NDT&E International*, vol. 42, no. 5, pp. 467–476, 2009.

[4] J. Zapata, R. Vilar, and R. Ruiz, "Performance evaluation of an automatic inspection system of weld defects in radiographic images based on neuro-classifiers," *Expert Systems with Applications*, vol. 38, no. 7, pp. 8812–8824, 2011.

[5] N. Boaretto and T. Mezzadri Centeno, "Automated detection of welding defects in pipelines from radiographic images DWDI," *NDT&E International*, vol. 86, pp. 7–13, 2017.

[6] V. Lashkia, "Defect detection in X-ray images using fuzzy reasoning," *Image and Vision Computing*, vol. 19, no. 5, pp. 261–269, 2001.

[7] E. Janssens, J. De Beenhouwer, M. Van Dael, T. De Schryver, L. Van Hoorebeke, P. Verboven, B. Nicolaï, and J. Sijbers, "Neural network Hilbert transform based filtered backprojection for fast inline X-ray inspection," *Measurement Science and Technology*, vol. 29, no. 3, p. 034012, 2018.

[8] J. You, G. Zeng, and Z. Liang, "FBP Algorithms for Attenuated Fan-Beam Projections," *Inverse Problems*, vol. 21, no. 5, 2005.

[9] D. M. Pelt, J. Sijbers, and K. J. Batenburg, "Fast tomographic reconstruction from highly limited data using artificial neural networks," in *1st International Conference on Tomography of Materials and Structures*, pp. 109–112, 2013.

[10] D. M. Pelt and K. J. Batenburg, "Fast Tomographic Reconstruction from Limited Data Using Artificial Neural Networks," *IEEE Trans Image Process*, vol. 22, no. 12, pp. 5238–5251, 2013.

[11] D. L. Olson and D. Delen, *Advanced Data Mining Techniques*. Springer, 1st edition, 2008.

Part III

TLGI Reconstruction Algorithms

5
Dual-axis Tomography

Contents

5.1 Introduction

Carbon Fiber Reinforced Polymer (CFRP) is a high-tech material used for many applications like sports goods [1], aerospace [2, 3] and civil engineering [4]. It owes its success to its macroscopic properties, for instance its high strength-to-weight ratio. CFRP is made of bundles of carbon fibers, which provide the strength of the material, as well as a resin matrix acting as a glue component. For most applications, it is important to know both the positions and the directions of the fibers or fiber bundles, as well as the positions of the pores between the fiber bundles where the resin matrix is situated [5].

To link the macroscopic properties to the microscopic structure of CFRP, non-destructive inspection is preferred. In transmission CT, the difference between the attenuation coefficients of the carbon fiber bundles and the resin matrix is however often very small, resulting in a low contrast image on which segmentation is challenging. To visualize the fiber bundles, PCCT is more recommended since the phase shifts induced by the fibers and the resin matrix are substantially different. Also small angle scattering can be of interest since the resin matrix hardly causes any scattering, while the fibers induce a lot of scattering when the direction of the fiber is parallel to the X-ray path.

As discussed in Chapter 2, in PCCT with a TLGI, the interference pattern at the detector is measured by recording several projection images with a translation of the absorption grating G_2 in between [6, 7]. Due to the orientation of the grating, the change in the interference pattern can only be measured in the direction perpendicular to the grating. Therefore, only the small angle scattering in the plane perpendicular to the grating can be measured. As a consequence, fiber bundles parallel to the grating will hardly be detected since the scattering mainly occurs when the fiber bundles are oriented parallel to the X-ray path. To overcome this limitation, an Eulerian cradle is often used [8, 9]. With the cradle, a sample can be oriented in any possible direction to acquire scattering information in many different planes. Combination of the different planes with scattering information allows to make a good estimation of the scattering profile in each pixel. Despite its large possibilities, an Eulerian cradle is a specialized piece of equipment that is not present in every lab. In addition, the extended scanning trajectory easily leads to very long scan times.

In this chapter, an alternative approach is proposed based on the knowledge that the fibers are oriented in two perpendicular directions. In the approach only two scans are performed for which the object is rotated over 90 degrees around an axis perpendicular to the gratings in between the two scans. We refer to this approach as a dual-axis scan. A dual-axis scan has less demanding requirements on the experimental hardware side compared to an Eulerian cradle, since no additional

equipment is required. Nevertheless, it is still sufficient to visualize the scattering in the fibers in two different directions which allows to greatly improve the 3D DFC reconstructions of scanned CFRP samples.
Apart from the small angle scattering, with a TLGI, also the differential phase shift can only be measured in the direction perpendicular to the gratings. Since the method is very sensitive to small phase shifts, the fibers parallel to the gratings are often detected best. The measured differential phase shifts from the fiber bundles perpendicular to the grating are less reliable when the fibers lie along the X-ray path because the large amount of small angle scattering caused by these fibers flattens out the measured interference pattern which makes the sinusoid fitting and the detection of the correct phase shift harder. Hence, the DPC reconstructions of CFRP samples can also benefit from a dual axis scan where information of the two scan are combined to improve the 3D DPC reconstruction.

5.2 Methods

Several steps are required to improve 3D DFC and DPC tomographic reconstructions with a dual-axis approach. The different steps are described in detail in this section.

Step 1: Data acquisition For the acquisition of a full dual-axis dataset, a sample was scanned twice with the TLGI with the same scanning parameters but once rotated over an angle of approximately 90 degrees around the axis connecting the source with the detector. This way, scattering information from two perpendicular directions was available as well as DPC information from two different directions.

Step 2: Holder Substraction AC To generate one tomographic reconstruction of the DPC and DFC data from the complete scan data of the dual-axis scan, the separate reconstructions of the two single datasets first have to be registered. However, since the holder is still at the same position while scanning the object in the rotated position, it is located at a different orientation relative to the sample for each of the two scans. It should therefore be subtracted from the projection data prior to the registration. The subtraction was performed by first generating two separate reconstructions of the AC data. Then, the holder was segmented out of the reconstructions and forward projections were simulated of the holder. These simulated projections were finally subtracted from the original projections.

Step 3: Dataset registration With the projection data without holder, two reconstructions of the AC data of both the scans were made. The two reconstructions were then registered using ASTRA toolbox [10] based alignment

software to find a good approximation of the orientations of the scans compared to one another. [11, 12] The software aims to minimize the projection distance between the measured projections and simulated projections of the sample made with an estimated projection geometry. Based on the projection distance, the projection geometry is altered in an attempt to find the optimal geometry vector.

Step 4: Holder Substraction DFC and DPC Since the ASTRA Toolbox is not capable of simulating DFC projection data of the segmented holder, the same procedure as for the AC data could not be followed. A more rudimentary approach is used instead in which certain pixels of the projection data are simply set to zero. These are pixels of which we are certain that the measured data is only from the holder and not from the sample. At detector pixels where the holder overlaps with the sample, the data from the holder cannot be subtracted. This has a small influence on the final reconstruction but does not affect the fiber detection. The same procedure was followed for the DPC data.

Step 5: Dual-axis reconstruction Several reconstruction algorithms were used to generate 3D reconstructions of the dual-axis scans of the DFC and DPC data. Hereby, the projections without holder as well as the correct projection geometry obtained after registration were considered.

5.3 Experiments and Results

A CFRP sample was scanned twice at the University of Applied Sciences in Wels with a TLGI. For each orientation of the sample, 1200 equiangular projections were acquired over a range of 360 degrees. After registration, we found that the second scan was obtained after a rotation of around 87.3 degrees and a slight translation and tilt. In the remainder of this section, the first scan will be referred to as the scan at zero degrees and the second scan at 90 degrees. The results for the DFC data and the DPC data are discussed separately.

5.3.1 DFC data

The reconstruction algorithms applied on the DFC data are SIRT for the single axis reconstructions and both SIRT and a maximum reconstruction algorithm for the dual-axis reconstructions. The maximum reconstruction algorithm takes for every voxel in the reconstruction image the maximum of the zero degrees reconstruction and the 90 degrees reconstruction. Since the small angle scattering is direction dependent and only one direction can be detected at the gratings, SIRT is, however,

not an optimal algorithm to reconstruct the dual-axis scan. Therefore, the dual-axis scan is also reconstructed with a directional SIRT algorithm used in X-ray tensor tomography. The directional SIRT takes into account the direction of the gratings, X-rays and scattering to adapt the projection model and predict values at the detector. It makes several reconstructions, each showing the scattering inside a pixel in a predefined direction. This way, a scattering tensor is reconstructed in every voxel [13, 14].
In Fig. 5.1, 3D DFC reconstructions and two orthogonal slices throughout the corresponding volumes are compared for single-axis and dual-axis scans based on 1200 projections. Similar reconstructions of the same samples are shown in Fig. 5.2 in case the reconstructions were made with 300 projections. In the single-axis scans, only the scattering of fibers oriented in one direction is detected. These are the fibers that lie in the scanning plane. In subimage (c),(g) and (k), a dual-axis reconstruction is shown where for each pixel, the maximum value of the two separate reconstructions is taken. Since the two images reveal information from two different directions, the result nicely shows all the pixels where small angle scattering occurs in these directions. The pixels can thus be classified as part of the fiber bundles. Subimages (d),(h) and (l) show a dual axis reconstruction where SIRT is performed on the data of the two scans together. Also here, more scattering information from different directions is visible in one image, allowing to see the fiber bundles in two directions in subimage (d). However, the projection model is not correct when simply applying SIRT on the data since the scattering is direction-dependent. The results are therefore not as good as the reconstruction that uses the maximum. The advantage of the dual reconstruction is that only one reconstruction needs to be made instead of two. When only limited projection data can be acquired due to physical or time constraints, Fig. 5.2 shows that it is better to acquire two scans with less projections to get an image of the small angle scattering inside the sample than performing only one scan with many more projections as shown in Fig. 5.1.

As mentioned earlier, the projection model for dual-axis reconstruction with SIRT is incorrect since it does not take the directionality of the scattering into account. Fig. 5.3 shows reconstructions of the scattering inside the sample in different directions for two orthogonal slices (left and right) obtained with the method of Malecki [8]. The scattering directions are:

$$[(1,0,0),(0,1,0),(1,1,0),(1,-1,0),(0,0,1),(1,0,1),(-1,0,1)]. \qquad (5.1)$$

Here, the small angle scattering in different directions is nicely visualized. Based on the reconstructions, a scattering profile of the fiber bundles can be constructed, which gives a lot more insight into the fiber structure compared to the maximum or dual SIRT reconstruction mentioned before.

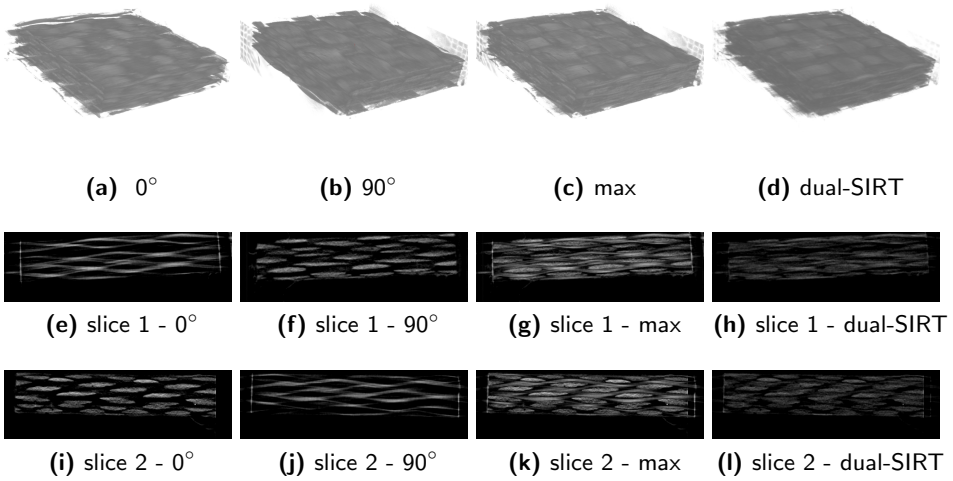

Figure 5.1: 3D reconstructions and two orthogonal slices throughout the volumes obtained with SIRT from 1200 projections for the zero degrees scans [(a)(e) and (i)], the 90 degrees scan [(b),(f) and (j)], a dual scan with maximum reconstruction [(c),(g) and (k)] and the dual axis scan with SIRT reconstruction [(d),(h) and (l)]

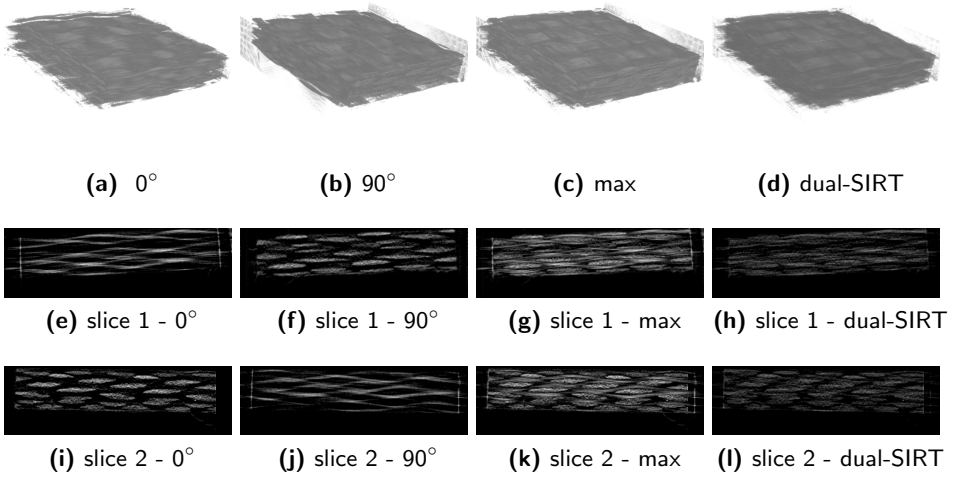

(a) 0° **(b)** 90° **(c)** max **(d)** dual-SIRT

(e) slice 1 - 0° **(f)** slice 1 - 90° **(g)** slice 1 - max **(h)** slice 1 - dual-SIRT

(i) slice 2 - 0° **(j)** slice 2 - 90° **(k)** slice 2 - max **(l)** slice 2 - dual-SIRT

Figure 5.2: 3D reconstructions and two orthogonal slices throughout the volumes obtained with SIRT from 300 projections for the zero degrees scans [(a)(e) and (i)], the 90 degrees scan [(b),(f) and (j)], a dual scan with maximum reconstruction [(c),(g) and (k)] and the dual axis scan with SIRT reconstruction [(d),(h) and (l)]

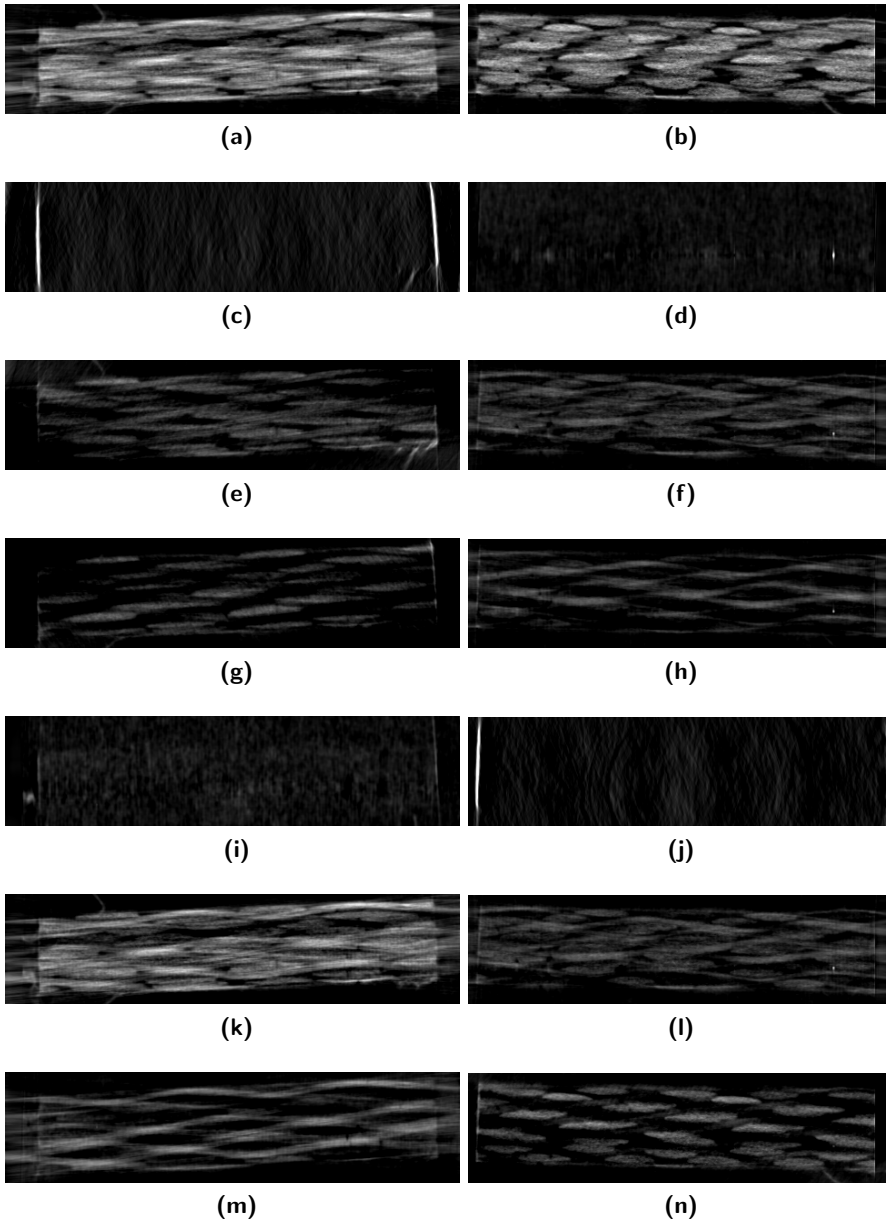

Figure 5.3: Two orthogonal slices through 3D reconstructions of small angle scattering in seven different directions: (a=b) (1,0,0), (c-d) (0,1,0), (e-f) (1,1,0), (g-h) (1,-1,0), (i-j) (0,0,1) (k-l) (1,0,1) and (m-n) (-1,0,1)

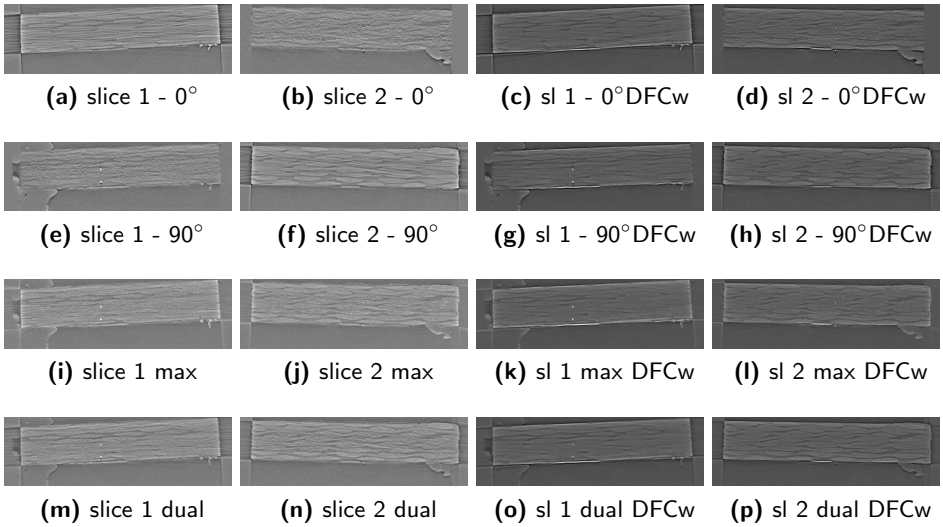

Figure 5.4: Images of two orthogonal slices through several 3D reconstructions based on 1200 projections. First row: 1st scan at 0°rotation, second row: 2nd scan at 90°rotation, third row: max of first and second scan, fourth row: dual axis reconstruction. Left two columns: DPC reconstruction, right two columns: DPC reconstruction with DFC weighting (DFCw)

5.3.2 DPC data

Due to the measurement of the differential phase shift, CG was used as a reconstruction algorithm for the DPC data. Reconstructions were made with and without DFC weighting. In DFC weighting, the DPC projection data is replaced by a scaled version of the AC projection data at detector pixels were the scattering exceeds a certain threshold. The replacement is performed because the measurement of the differential phase is very unreliable at these pixels. The method was proposed by Jerjen in [15].
Fig. 5.4 and 5.5 show two orthogonal slices through DPC reconstructions with and without DFC weighting of the two single-axis scans and dual-axis scans for 1200 en 300 projections. In the single axis scans, the fiber bundles that are best visualized are perpendicular to the ones visualized in DFC. These are the ones of which the measurement is least affected by scattering. In case of DFC weighting, the reconstructions all look very similar since the information of the absorption reconstruction is incorporated into the reconstruction. The reconstruction is therefore similar to the absorption reconstruction which is direction invariant and the added

value of a dual-axis scan is limited.
For DPC data without DFC weighting, a dual axis scan improves the reconstruction. Here, little difference is found between the maximum reconstruction and the dual CG reconstruction. DPC is however less direction dependent than DFC. A single DPC reconstruction of 1200 projections generally obtains better reconstructions than a dual reconstruction of 300 projections. Fig. 5.6 shows 3D reconstructions of the single-axis and dual-axis DPC reconstructions without DFC weighting for 1200 and 300 projections. On these reconstructions, one can see that the dual-axis CG reconstruction is clearly better in capturing information on the phase shift caused by the fiber bundles in two directions opposed to the single axis reconstructions, certainly for 1200 projections.

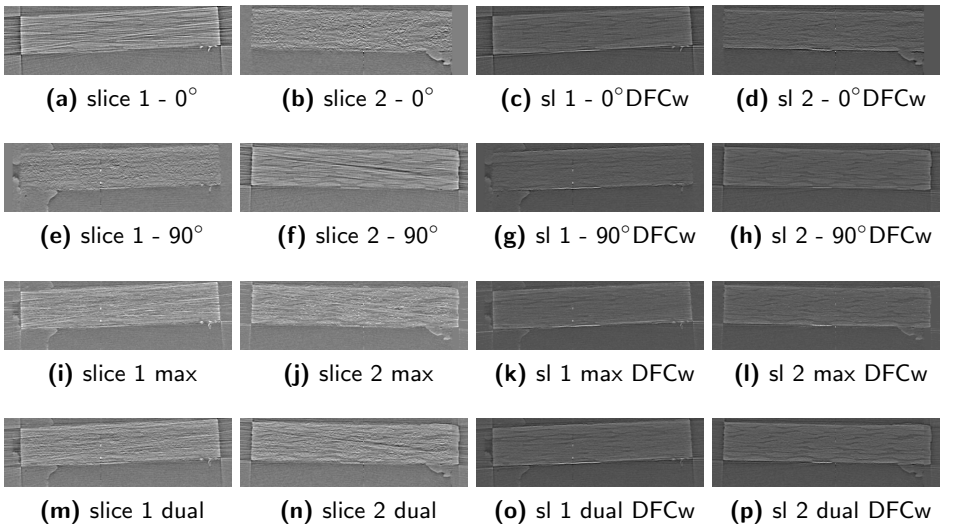

Figure 5.5: Images of two orthogonal slices through several 3D reconstructions based on 300 projections.

5.4 Conclusion

For visualization of the fiber structure inside a CFRP sample, it is beneficial to scan the sample twice, with a 90 degrees rotation in between, and use both sets of projection data to make one 3D reconstruction of the DPC and DFC data. This way, fiber bundles with different orientations can be visualized in one reconstruction. With the dual-axis scans, sufficient information on the small angle scattering

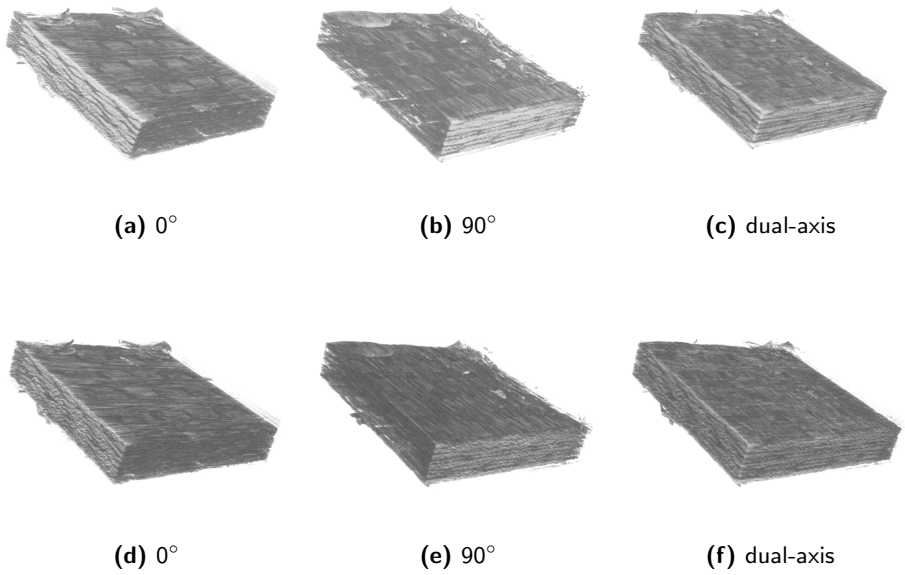

(a) 0° **(b)** 90° **(c)** dual-axis

(d) 0° **(e)** 90° **(f)** dual-axis

Figure 5.6: 3D reconstructions of the first dataset acquired at 0°(left) and the second dataset acquired at approximately 90°(middle) and dual-axis reconstruction (right) for 1200 (top) and 300 (bottom) projections

and phase shifts inside the sample can be acquired to detect fiber bundles in orthogonal directions, which drastically decreases the need for an Eulerian cradle. In this work, SIRT and CG were used as reconstruction algorithms as well as a more realistic directional SIRT algorithm. Further work should however be performed to improve the models with even more realistic scattering profiles.

References

[1] D. Z. Tang, "The Application of Carbon Fiber Materials in Sports Equipment," in *Computer-Aided Design, Manufacturing, Modeling and Simulation III*, vol. 443, pp. 613 – 616, 2014.

[2] N. V. Nayak, "Composite Materials in Aerospace Applications," *International Journal of Scientific and Research Publications*, vol. 4, no. 9, 2014.

[3] E. R. Guzman Solares, *A Novel Structural Health Monitoring Method for Full-Scale CFRP Structures*. PhD thesis, École Polytechnique Fédérale de Lausanne, 2015.

[4] I. Olofin and R. Liu, "The Application of Carbon Fibre Reinforced Polymer (CFRP) Cables in Civil Engineering Structures," *SSRG International Journal of Civil Engineering (SSRG-IJCE)*, vol. 2, no. 7, 2015.

[5] C. Goidescu, H. Welemane, C. Garnier, M. Fazzini, R. Brault, E. Peronnet, and S. Mistou, "Damage investigation in CFRP composites using full-field measurement techniques: combination of digital image stereo-correlation, infrared thermography and X-ray tomography," *Composites Part B: Engineering*, vol. 48, pp. 95–105, 2013.

[6] F. Pfeiffer, T. Weitkamp, O. Bunk, and C. David, "Phase retrieval and differential phase-contrast imaging with low-brilliance X-ray sources," *Nat. Phys.*, vol. 2, pp. 258–261, 2006.

[7] M. Bech, *X-ray imaging with a grating interferometer*. PhD thesis, University of Copenhagen Faculty of Science, 2009.

[8] A. D. Malecki, *X-Ray Tensor Tomography: From Two-Dimensional Directional X-Ray Dark-Field Imaging to Three Dimensions*. PhD thesis, Technische Universität München, 2013.

[9] Y. Sharma, M. Wieczorek, F. Schaff, S. Seyyedi, F. Prade, F. Pfeiffer, and T. Lasser, "Six dimensional X-ray Tensor Tomography with a compact laboratory setup," *Appl. Phys. Lett.*, vol. 109, p. 134102, 2016.

[10] W. van Aarle, W. J. Palenstijn, J. De Beenhouwer, T. Altantzis, S. Bals, K. J. Batenburg, and J. Sijbers, "The ASTRA Toolbox: a platform for advanced algorithm development in electron tomography," *Ultramicroscopy*, vol. 157, pp. 35–47, 2015.

[11] W. van Aarle, W. J. Palenstijn, J. Cant, E. Janssens, F. Bleichrodt, A. Dabravolski, J. De Beenhouwer, K. J. Batenburg, and J. Sijbers, "Fast and flexible X-ray tomography using the ASTRA toolbox," *Optics Express*, vol. 24, no. 22, pp. 25129–25147, 2016.

[12] B. Goris, J. De Beenhouwer, A. De Backer, D. Zanaga, K. Batenburg, A. Sánchez-Iglesias, L. Liz-Marzán, S. Van Aert, S. Bals, J. Sijbers, and G. Van Tenderloo, "Measuring lattice strain in three dimensions through electron microscopy," *Nano letters*, vol. 15, no. 10, pp. 6996–7001, 2015.

[13] A. Malecki, G. Potdevin, T. Biernath, E. Eggl, K. Willer, T. Lasser, J. Maisenbacher, J. Gibmeier, A. Wanner, and F. Pfeiffer, "X-ray tensor tomography," *EPL Europhysics Letters*, vol. 105, no. 3, p. 38002, 2014.

[14] J. Vogel, F. Schaff, A. Fehringer, C. Jud, M. Wieczorek, F. Pfeiffer, and T. Lasser, "Constrained X-ray tensor tomography," *Optics Express*, vol. 23, no. 12, pp. 15134–15151, 2015.

[15] I. Jerjen, V. Revol, P. Schuetz, C. Kottler, R. Kaufmann, T. Luethi, K. Jefimovs, C. Urban, and U. Sennhauser, "Reduction of phase artifacts in differential phase contrast computed tomography," *Optics Express*, vol. 19, no. 14, pp. 13604–13611, 2011.

6

Discrete Phase Contrast Computed Tomography: MV-DART

Contents

6.1 Introduction

In tomography, a 3D reconstruction of the inside of a sample is made by applying a reconstruction algorithm on a set of 2D measured projection data. In general, the reconstructed values are continuous and no prior knowledge exists about the sample. For some applications, discretization of the final reconstruction is of interest. For instance for Fiber Reinforced Polymer (FRP) samples, it can be used to segment out the fibers or fiber bundles. In discrete tomography, the reconstructed values are all elements of a discrete set of output values of the algorithm. This set may be known in advance as prior knowledge, or it can be constructed during the reconstruction. Discrete tomography has important applications in multivalued imaging such as TLGI imaging. With a TLGI, three different imaging modalities can be recorded, resulting in three images with information on the absorption, differential phase shift and small angle scattering present in a sample as discussed in Chapter 2. When the material distribution inside a sample is of interest, the information on the different modalities should be combined to allow optimal material segmentation. The field of image fusion copes with the combination of different modalities into one fused image. Until now, the most common way of fusing the AC, DPC and DFC information is by performing separate reconstructions and afterwards combining the reconstructions for analysis. A two-step fusion process was proposed by Stampanoni et al. [1] in 2013 where first the absorption and differential image were fused into a single grey value image and afterwards, a color-coded dark field image was superimposed on the fused image. Scholkmann et al. [2] introduced a two-step fusion method based on the shift-invariant wavelet transform, while Haas et al. [3] proposed to use a linear combination of the three imaging modalities with specially designed weights. Recently, Gusenbauer et al. [4] used a simple image fusion method which combines both high-pass and low-pass filtered AC, DPC and DFC images with their corresponding image masks to highlight desired features.

Instead of fusing the images after they are reconstructed, in this work, the images are already fused during the reconstruction process by exploiting discrete tomography. For multimodal images, Nielsen [5] proposed to improve the quality of the segmentation by using multivariate segmentation with the Euclidean norm on the AC and DPC reconstructions. Hereby, he also performed a kind of discrete image fusion. It would however be interesting if the segmentation could steer the reconstruction and vice versa. Batenburg and Sijbers [6] proposed in 2011 the DART algorithm, which is an iterative reconstruction technique that provides discrete reconstructions by exploiting prior knowledge on the grey levels and performing intermediate segmentations to steer the reconstruction.

In this dissertation, a Multivariate DART (MV-DART) algorithm is presented that

combines the steered discrete reconstruction method of Batenburg and Sijbers with the multivariate segmented image fusion of Nielsen. The algorithm performs two DART reconstructions on the AC and DPC data, in which the segmentation step is replaced by a multivariate segmentation step that fuses the two modalities. In addition, also an MV-DART algorithm with DFC weighting is proposed to exploit all information captured in the TLGI data. In the algorithm, the DFC data is used to steer the segmentation towards the AC segmentation in case of high small angle scattering inside the sample.

6.2 Methods

The most important building block of the MV-DART algorithm is the discrete reconstruction algorithm DART. In this section, the DART algorithm is first explained, before going into more detail on the new MV-DART algorithm. Last, an extension of the MV-DART algorithm, the MV-DART algorithm with DFC weighting, is discussed.

6.2.1 Discrete Algebraic Reconstruction Technique

The Discrete Algebraic Reconstruction Technique or DART algorithm was first developed by K.J. Batenburg and J. Sijbers in 2011 [6]. It is an iterative reconstruction algorithm that results in a segmented reconstruction of the scanned object by imposing prior knowledge on the reconstruction. The prior knowledge exploited in the algorithm is the value of the attenuation coefficients or grey values of the different materials inside the object. Knowing these values, the reconstruction can be steered towards them. The algorithm consists of several steps over which is iterated:

1. First, an initial reconstruction is made with an algebraic reconstruction method, often SIRT or SART, that aims to converge to a solution of :

$$\boldsymbol{x}_{\text{opt}} = \arg\min_{\boldsymbol{x}}(\|\boldsymbol{A}\boldsymbol{x} - \boldsymbol{p}\|_2^2), \tag{6.1}$$

   where $\boldsymbol{p} \in \mathbb{R}^{M\times 1}$ is the measured projection data, $\boldsymbol{A} \in \mathbb{R}^{M\times N}$ is the projection matrix and $\boldsymbol{x} \in \mathbb{R}^{N\times 1}$ is the reconstructed image.

2. The reconstruction is segmented by global thresholding based on the available prior knowledge on the grey values.

3. The segmented image is subdivided into a set of fixed and a set of free pixels.

4. Several iterations of the algebraic reconstruction method are performed on the set of free pixels while the fixed pixels are kept constant.

5. As long as a certain stopping criteria is not met, the reconstruction is smoothed and the algorithm jumps back to step 2, otherwise, the final reconstruction image is obtained.

The division of the free and fixed pixels in step 2 is made based on 'how certain' one is that the segmentation value of a pixel is correct. In general, this certainty is high inside a material but lower at the boundaries. Therefore, boundary pixels are classified as free pixels and bulk pixels are classified as fixed pixels. A boundary pixel is defined as a pixel of which the value is different from at least one of its neighbouring pixels. Since this segmentation prevents detection of holes inside an object, a percentage of randomly selected pixels are added to the set of free pixels. These random pixels, together with the last smoothing step, also help the algorithm cope with noise. In the smoothing step, a Gaussian smoothing filter with radius 1 is applied.

The strength of the DART algorithm is the substantial reduction of unknowns due to the set of fixed pixels and the intermediate segmentations. Therefore, the algorithm is capable of obtaining good segmented reconstructions, even in case of limited wedge or truncation artefacts. The performance of the algorithm is however limited when the projection data is corrupted with noise. Also when the number of grey values is too high or when they are close together, the segmentation is less reliable which reduces the performance of the algorithm.

An important challenge for DART is to obtain the correct grey values as prior knowledge. In case of experimental data, this is not a straightforward task. Therefore, among others, the PDM-DART algorithm was introduced by van Aarle et al. [7] in which the correct grey values are automatically estimated by projection distance minimization. Furthermore, the last years several other algorithms are derived from DART like SDART [8], PDART [9], TVR-DART [10], DIPS-DART [11],... all aiming to improve the DART algorithm for specific situations.

6.2.2 Multivariate DART

Based on the DART algorithm described in the previous section, the Multivariate DART (MV-DART) algorithm is now introduced. With the MV-DART algorithm, one segmented reconstruction of an object is made, based on the combined information of the AC and DPC data. On a side note, the method could for example also be used on two datasets acquired in a dual energy scan. However, in this thesis, the focus lies on the application of MV-DART on PCCT data. Instead of reconstructing and segmenting the AC and DPC signals separately and combining the final

results, here, the aim is to combine the signals during reconstruction to obtain an improved final segmented image. The basis for MV-DART are two separate DART algorithms: one for the AC data and one for the DPC data. The two algorithms are combined in the segmentation step where the two individual segmentations are replaced by a multivariate segmentation step. In this thesis, a basic multivariate segmentation method is applied, namely the Euclidean norm. For each material inside the object, the corresponding grey value pair $\boldsymbol{r} = (\rho, \phi)$ for the AC and DPC reconstruction is assumed to be known in advance. Suppose the set of known grey value pairs to be $R = \{\boldsymbol{r}_1, \boldsymbol{r}_2, ..., \boldsymbol{r}_K\} = \{(\rho_1, \phi_1), (\rho_2, \phi_2)...(\rho_K, \phi_K)\}$ with K the number of materials inside the object. For every point in the reconstructed AC and DPC image denoted by $\boldsymbol{q} = (x, y)$, the corresponding segmented reconstructed point $\boldsymbol{S} = (S_x, S_y)$ is calculated by the minimal Euclidean norm as follows:

$$\boldsymbol{S} = \arg\min_{\boldsymbol{r}_j \in R} \|\boldsymbol{q} - \boldsymbol{r}_j\|_2. \tag{6.2}$$

Since the attenuation coefficient and the phase shift are often not of the same order of magnitude, a better approach is to use a weighted Euclidean norm. This norm can cope with scaling differences and can be tuned to favour either the contribution of the AC signal or the DPC signal.

$$\boldsymbol{S} = \arg\min_{\boldsymbol{r}_j \in R} \|(\boldsymbol{q} - \boldsymbol{r}_j)\boldsymbol{w}\|_2, \tag{6.3}$$

where $\boldsymbol{w} = (\omega, 1-\omega)^T, \omega \in [0, 1]$ specifies the contribution of each imaging modality to the weighted Euclidean norm.

All the PCCT data in this thesis is acquired with a TLGI. The interferometer measures the differential phase. In order to perform the DART algorithm on the differential phase data, the algebraic reconstruction method on which the algorithm is built, should be able to handle the differential data. Therefore, in the MV-DART algorithm, the Conjugate Gradient (CG) algorithm [12] has been chosen as algebraic reconstruction method. The algorithm can reconstruct both the AC and DPC data. Concerning the DPC data, the algorithm aims to converge to a solution of:

$$\boldsymbol{x}_{\text{opt}} = \arg\min_{\boldsymbol{x}}(\|\boldsymbol{A^T D^T D A x} - \boldsymbol{A^T D^T p}\|_2^2), \tag{6.4}$$

where $\boldsymbol{D} \in \mathbb{R}^{M \times M}$ is a derivative matrix, modelling the forward, central or backward derivative of the projection data. For CG, the number of iterations is critical on real data: too many iterations introduces artefacts in the reconstruction. Hence, the number of initial and intermediate iterations should be kept low, typically less than 100. Furthermore, as with conventional DART, selecting the correct grey values as prior knowledge remains a very difficult task.

6.2.3 Multivariate DART with Dark Field weighting

In PCCT with a TLGI, also a DFC image can be reconstructed which is not yet incorporated in the MV-DART algorithm despite its valuable information on the small angle scattering inside an object. The measured sinusoid at the detector pixels that contain information on regions with a lot of small angle scattering has a decreased amplitude which makes the detection of the phase shift harder and the DPC image at voxels with high scattering less reliable. At these voxels, the AC data gives a better representation of the underlying structure, which can be exploited to improve the MV-DART algorithm. Jerjen et al [13] already performed phase weighting on the DPC data in the projection space by replacing the DPC data with a weighted version of the AC data at those detector pixels where the small angle scattering was above a certain threshold. A disadvantage of the technique is that a conversion factor from the absorption projection space towards the differential phase contrast projection space is required. In the proposed MV-DART with DFC weighting, the weighting is performed in the reconstruction space at the segmentation step. At the reconstruction voxels where the DFC signal is high, the weight of the AC reconstruction in the Euclidean norm is higher than the weight of the DPC reconstruction. One can choose to either use a hard threshold or a softer weighting. In case of a hard threshold, the segmentation is purely based on the AC image when the DFC image exceeds the threshold. Define d as the value of a pixel in the DFC image and t as a predefined threshold. The value of the segmented image at that pixel will then be defined as:

$$\boldsymbol{S} = \begin{cases} \arg\min_{\boldsymbol{r}_j \in R} |x - \rho_j| & d \geq t, \\ \arg\min_{\boldsymbol{r}_j \in R} \|\boldsymbol{q} - \boldsymbol{r}_j\|_2 & d < t. \end{cases}$$

In a softer version, an extra weighting factor can be added to the weighted Euclidean norm which favours the absorption segmentation in case of a higher DFC reconstruction signal. The segmented value will then be:

$$\boldsymbol{S} = \arg\min_{\boldsymbol{r}_j \in R} \|(\boldsymbol{q} - \boldsymbol{r}_j)\boldsymbol{w'}\|_2, \tag{6.5}$$

where $\boldsymbol{w'} = (\alpha\omega, 1-\omega)^T, \omega \in [0,1]$ specifies the contribution of each imaging modality to the weighted Euclidean norm, multiplied by a factor α that favours AC segmentation in case of high scattering. In this work, experiments are only performed with a hard threshold due to the low quality of the DPC data.
In the DART algorithm, the acquisition process of X-ray interactions with matter is modelled by the forward model of the ASTRA toolbox [14, 15] extended with a derivative when applied to the DPC data. Unfortunately, the model does not take into account the scattering that occurs inside the sample. Minimization of

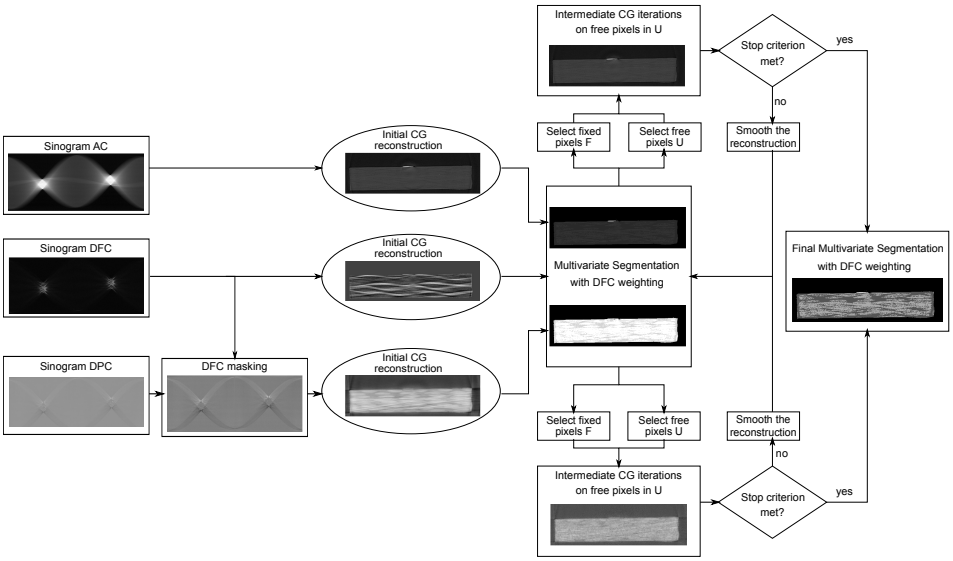

Figure 6.1: Schematic of the MV-DART algorithm with DFC weighting.

the DPC projection error is therefore unreliable at detector pixels which measure high scattering. A solution for the problem is to omit these pixels from the reconstruction problem when the DFC image exceeds another predefined threshold. Therefore, the projection matrix should be altered by setting the corresponding rows to zero. The MV-DART algorithm with DFC weighting requires two additional thresholds on the DFC data. Although introducing extra parameters makes the optimization of the algorithm even harder, significantly better results can be obtained. Fig. 6.1 gives a schematic overview of the MV-DART algorithm with DFC weighting.

6.3 Experiments and Results

The performance of the MV-DART algorithm is evaluated in this section. First, simulation experiments are performed on which the Relative Number of Misclassified Pixels (RNMP) can be used as a measure for the reconstruction quality. Afterwards, the MV-DART without and with DFC weighting is tested on a real CFRP dataset.

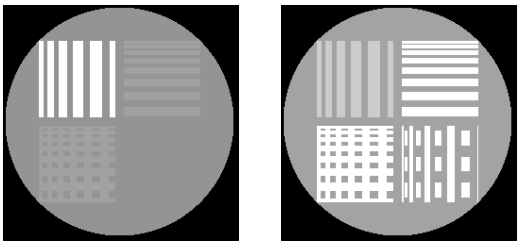

(a) (b)

Figure 6.2: Simulation phantom for (a) absorption contrast data and (b) differential phase contrast data.

6.3.1 Simulation Data

The best way to evaluate the performance of the MV-DART algorithm, is by simulating a real data scan. With the ASTRA toolbox, it is however not possible at the moment to accurately simulate data acquired with a TLGI. The toolbox can not simulate the scattering inside the sample. In this section, a 2D sample is simulated consisting of four different materials, but the simulation can easily be extended to 3D. The simulated data is shown in Fig. 6.2 and the corresponding values for the simulated attenuation coefficients and phase shifts are given in the last row of Table 6.1. In the AC image, one of the fiber materials has the same attenuation coefficient as the simulated resin matrix and in the DPC image, the same material cannot be distinguished from one of the other simulated fiber materials. Reconstructing only one of the modalities will not provide enough information on the materials inside the sample. Assume that a reconstruction pixel has a size of 1μm by 1μm, then all the projection data simulated from the phantom in this section is acquired over a range of 2π with 500 detector pixels of 1μm, a source-object distance of 1000μm and an object-detector distance of 400μm.

Before comparing the MV-DART algorithm to another reconstruction algorithm, in a first experiment the weight factor ω which determines the contributions of each modality, is studied. In the right column of Table 6.1, the values for the different parameters of the MV-DART algorithm are specified. The smoothing parameter and the fraction of random pixels are chosen empirically. For DPC data, the number of initial CG iterations depends on the number of projections and decreases with an increasing number of projections. The number of DART iterations is chosen so that the RNMP approximately stagnates. In Table 6.1, I is a measure for the noise that is added to the projection data. In case of the DPC data, the noise was added right before the differential was taken. A higher value

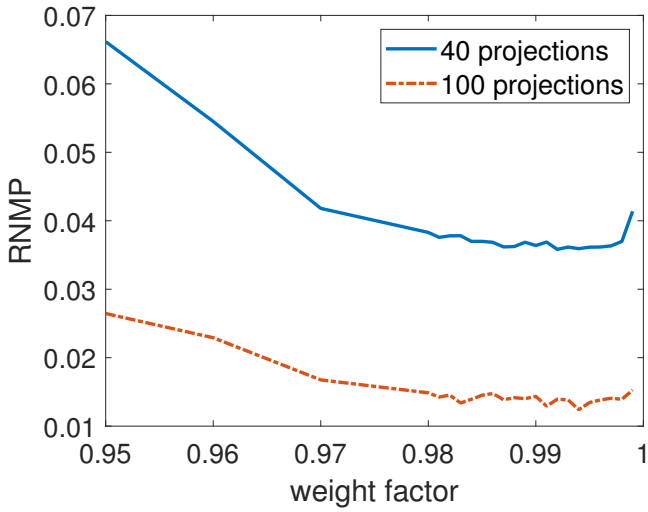

Figure 6.3: Evaluation of the RNMP in function of the weight factor ω for 40 and 100 projections.

of I means less noise is added to the data. Since the grey values of the AC data are much closer together than those of the DPC data, less noise is added to make sure that the underlying structure can still be detected. Fig. 6.3 shows the RNMP for MV-DART reconstructions with 40 and 100 projections where the weight factor ω has a value between 0.95 and 0.999. This high value is caused by the difference in magnitude between the grey values of the AC data and those of the DPC data. Since the noise added to the data and the random pixels selected during the DART algorithm are different for every reconstruction, the results are never identical and therefore the RNMP can slightly fluctuate. The optimal value lies between $\omega = 0.98$ and $\omega = 0.999$ and in the remainder of this chapter, $\omega = 0.997$ is chosen.

In a second step, the simulated data is reconstructed both with the conventional DART algorithm on the AC and DPC data and with the combined MV-DART algorithm for an increasing number of projections. Additionally, the influence of a median filter is evaluated. The median filter is applied during the algorithm after each segmentation step. Specifications of the parameters for DART are given in Table 6.1. Fig. 6.4 shows the RNMP for the DART and MV-DART reconstructions of the AC and DPC data with and without a median filter. Based on the graph, the MV-DART algorithm outperforms the single DART algorithms in reconstruction quality for both AC and DPC data when evaluated with the RNMP. Addition of the

Table 6.1: Specifications (MV-)DART algorithm.

	DART AC	DART DPC	MV-DART
volume size	250×250 pix	250×250 pix	250×250 pix
ARM algorithm	CG	CG	CG
smoothing parameter	0.6	0.6	0.6
fraction random pixels	0.4	0.4	0.4
initial CG iterations	20	65-249	[20,65-249]
intermediate CG iterations	5	5	5
DART iterations	30	30	30
I (Poison noise)	500000	100000	[500000,100000]
weight Euclidean norm ω	-	-	0.999
differentiation method	-	-	central
material values	$\begin{bmatrix} 0 \\ 0.0011 \\ 0.0012 \\ 0.0019 \end{bmatrix}$	$\begin{bmatrix} 0 \\ 0.016 \\ 0.020 \\ 0.025 \end{bmatrix}$	$\begin{bmatrix} 0 & 0 \\ 0.0011 & 0.016 \\ 0.0011 & 0.025 \\ 0.0012 & 0.025 \\ 0.0019 & 0.020 \end{bmatrix}$

median filter improves the reconstruction quality of the DART algorithm for both modalities but does not improve the performance of the MV-DART algorithm.

Fig. 6.5 and Fig. 6.6 show the reconstruction images made with the DART and MV-DART algorithm for 100 and 40 projections as well as the maps with misclassified pixels. The MV-DART algorithm clearly improves the reconstruction quality by reducing the noise and the classification of the boundary pixels at the border of the simulated fiber bundles is more accurate. In the DART reconstructions, the boundary pixels are badly classified since for certain simulated fiber bundles another grey value is present between the grey value of the fiber bundle and the grey value of the background. At this boundary, the pixels are classified into the intermediate value. In the MV-DART algorithm, the combined segmentation step avoids this situation. For the AC and DPC data, the median filter reduces the noise, but for the MV-DART, it reduces the spatial resolution, therefore better reconstructions are obtained without the median filter. The observations are in accordance with the results obtained from the graphs in Fig. 6.4. The reconstruction quality of MV-DART for 40 projections is similar or even better than the reconstruction quality of DART for 100 projections, therefore, the algorithm has potential to solve limited data problems.

An advantage of the MV-DART algorithm is that a combined segmentation of the sample is made simultaneously. This segmentation shows the different materials that are present inside the sample, which should normally be done afterwards as a post-processing step. Validation of the material identification is of most in-

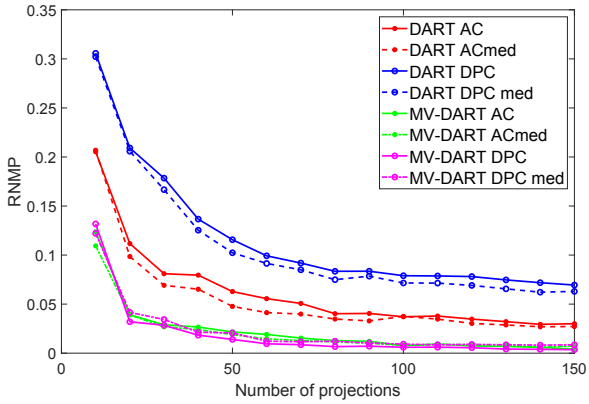

Figure 6.4: Relative Number of Misclassified Pixels (RNMP) in function of the number of projections for the absorption and DPC reconstructions with DART and MV-DART with and without median filter.

terest for the user. Therefore, in Fig. 6.7, the RNMP is plotted in function of the number of projections for the final material segmentation of MV-DART compared to a material segmentation of DART obtained with a post-processing step. The MV-DART algorithm clearly obtains better reconstructions. For all number of projections, the reconstructions made with MV-DART have a lower RNMP compared to the DART reconstructions, both when a median filter is applied and without the median filter. Again, the median filter does not provide added value to the MV-DART algorithm.

Fig. 6.8 shows the material segmentation reconstructions for the MV-DART algorithm and for the combination of the AC and DPC DART algorithm in case of 100 and 40 projections. In the combined DART reconstructions, white spots appear in the reconstructions. These are pixels in which the combination of the absorption and DPC reconstruction values does not correspond to one of the five materials defined at the beginning (see the third column of table 6.1). They represent other materials that are not present in the sample and a more complex classification method should be used to classify them into one of the five pre-set categories. In case of 40 projections, the combined DART reconstruction is highly corrupted with noise compared to the MV-DART reconstruction. Applying the median filter reduces the difference but from the images it is still clear that a better reconstruction quality can be obtained with the MV-DART algorithm.

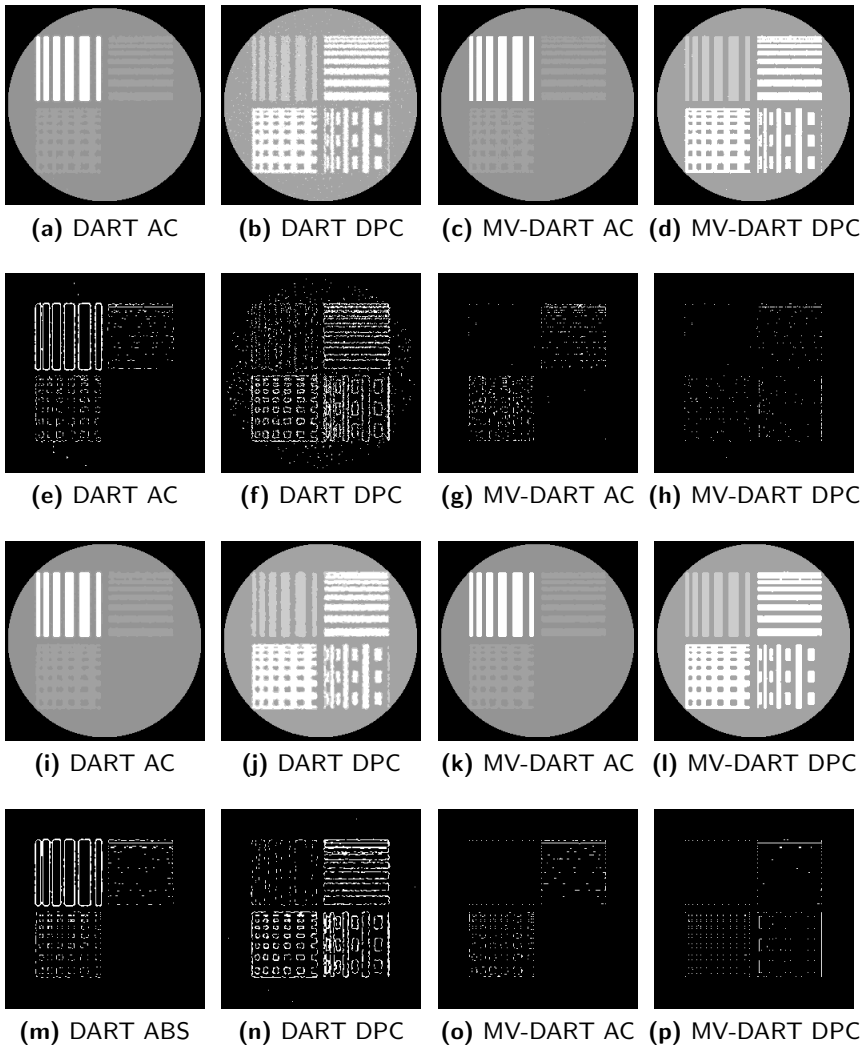

(a) DART AC **(b)** DART DPC **(c)** MV-DART AC **(d)** MV-DART DPC

(e) DART AC **(f)** DART DPC **(g)** MV-DART AC **(h)** MV-DART DPC

(i) DART AC **(j)** DART DPC **(k)** MV-DART AC **(l)** MV-DART DPC

(m) DART ABS **(n)** DART DPC **(o)** MV-DART AC **(p)** MV-DART DPC

Figure 6.5: Reconstructions and error maps based on 100 projections without (first and second row) and with (third and fourth row) a median filter.

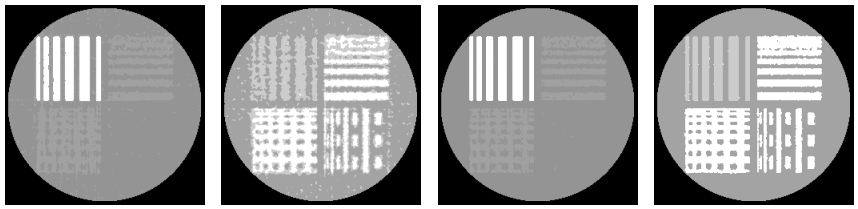

(a) DART AC **(b)** DART DPC **(c)** MV-DART AC **(d)** MV-DART DPC

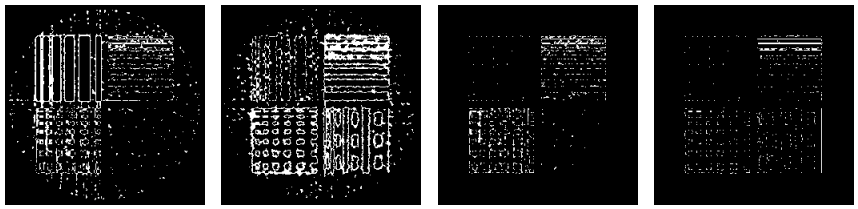

(e) DART AC **(f)** DART DPC **(g)** MV-DART AC **(h)** MV-DART DPC

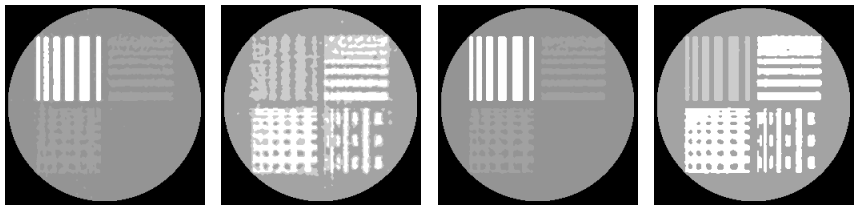

(i) DART AC **(j)** DART DPC **(k)** MV-DART AC **(l)** MV-DART DPC

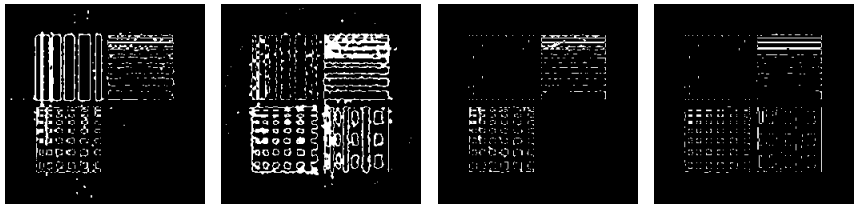

(m) DART AC **(n)** DART DPC **(o)** MV-DART AC **(p)** MV-DART DPC

Figure 6.6: Reconstructions and error maps based on 40 projections without (first and second row) and with (third and fourth row) a median filter.

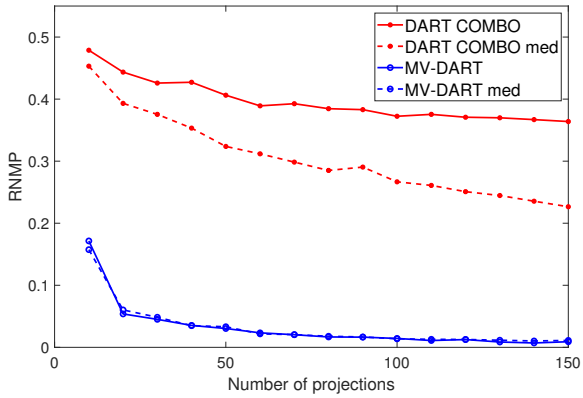

Figure 6.7: Relative Number of Misclassified Pixels (RNMP) in function of the number of projections for the combined AC and DPC reconstructions with DART and the MV-DART algorithm with and without median filter.

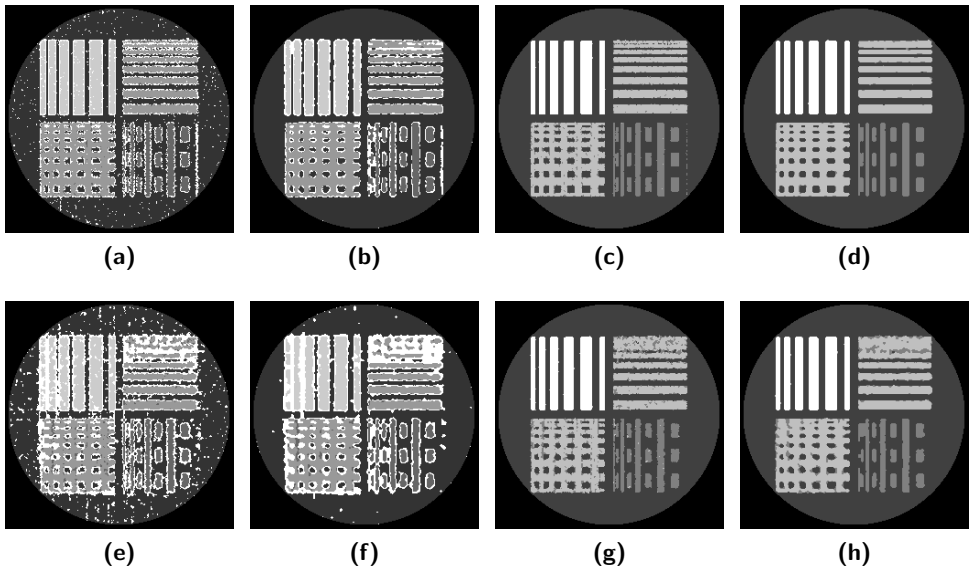

Figure 6.8: Reconstructions based on 100 (top row) and 40 (bottom row) projections: (a) and (e) combined DART reconstruction of AC and DPC data, (b) and (f) combined DART reconstruction with median filtering, (c) and (g) MV-DART reconstruction, (d) and (h) MV-DART reconstruction with median filtering.

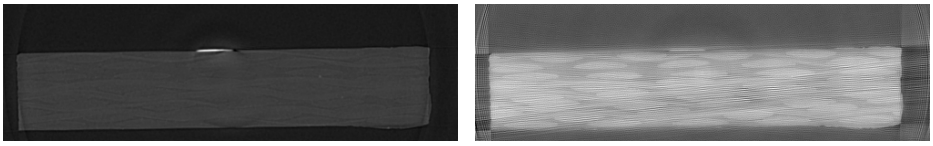

(a) (b)

Figure 6.9: CG reconstructions based on 1200 projections for (a) absorption contrast data and (b) differential phase contrast data.

6.3.2 Real Data

For the real data experiments, a sample in which different materials had the same attenuation coefficient or phase shift was not at hand. However, the method also works when DPC data is corrupted with artefacts due to small angle scattering. Therefore, a CFRP sample was chosen for the real data scans in which the fibers could be distinguished from the resin matrix in the AC reconstruction made with 1200 projections but at a very low contrast, which makes segmentation hard. In the DPC data, the contrast between the fibers and the resin matrix is higher, but the reconstruction is corrupted with streaking artefacts as shown in Fig. 6.9. The CFRP sample was scanned at the University of Applied Sciences in Wels with a TLGI. Specifications of the scan can be found in Table 6.2. For all the DART algorithms used in this section, the Gaussian kernel width was set to 0.3 pixels and the fraction of randomly selected pixels to 0.6. Other parameters of the DART and MV-DART algorithm used are mentioned together with the images as they vary from image to image. When multiple t0 values (initial ARM iterations) or t values (intermediate ARM iterations) are shown for the MV-DART algorithm, they correspond to the iterations for the AC, DPC and DFC reconstructions in that order. When DFC weighting is applied, two extra thresholds are present: the threshold tDFrec which is the threshold for small angle scattering in the reconstruction domain and tDFproj which is the threshold for small angle scattering in the projection domain.

Before DART or MV-DART can be used to obtain a segmented reconstruction of the sample, the grey values of the materials inside the sample should be determined. Very little prior knowledge exists on the sample, therefore the grey values is determined based on the CG reconstructions of 1200 projections. To determine the values, a segmentation of the reconstruction was performed. Several methods were evaluated like manual segmentation, Otsu segmentation, kmeans segmentation and PDM-DART segmentation. For the absorption reconstruction, all methods generated very similar results for the segmentation values, which gave

Table 6.2: Specifications of CFRP scan

SOD	140mm
SDD	286mm
detector row width	11.6um
detector column width	11.6um
binning	4
number of projections	1200
angular range	2π
number of detectors in 1 row	500
reconstruction voxel size	22.8um
number of reconstruction voxels	150×500×500

an indication that the chosen segmentation values are close to the actual grey values. In the DPC data, the high absorbing glue on top of the sample had a similar phase shift as the fiber bundles. Thus, only three different values for the phase shifts were chosen. With Otsu and kmeans segmentation, detection of the correct grey values gave unsatisfactory results. The final grey values were determined by the PDM-DART algorithm where high scattering pixels were omitted from the projection data. It is however very hard to decide whether these values are accurate since similar results can be found with other segmented grey values.
Fig. 6.10 shows the central slice of the reconstructed sample obtained with different reconstruction methods. For 1200 projections, the segmented CG and DART reconstructions are very similar for the AC data. On the images it can be seen that when all DPC data is used and small angle scattering is not taken into account, the DART algorithm does not provide a good segmented reconstruction for the DPC data. Better segmentations could be obtained with other grey values, although the reconstructions would still be distorted by artefacts. The MV-DART reconstruction is very similar to the DART reconstruction of the AC data. Since the DPC data is corrupted with artefacts, the segmentation is mainly based on the AC data causing the presence of the same artefacts from ring artefact correction in MV-DART as in DART for AC. However, when DFC weighting is applied, the artefacts in the DPC reconstruction are largely removed. As a result, the DPC data can be used to improve the AC segmentation and a better segmented reconstruction is obtained with MV-DART. Similar results are obtained for the reconstructions made with 300 projections as shown in Fig. 6.11. The images show that the MV-DART algorithm with DFC weighting is capable of reconstructing fiber bundles inside the CFRP sample, which is not possible when only the AC or DPC data is taken into account. Fig. 6.11(f) shows that after application of the

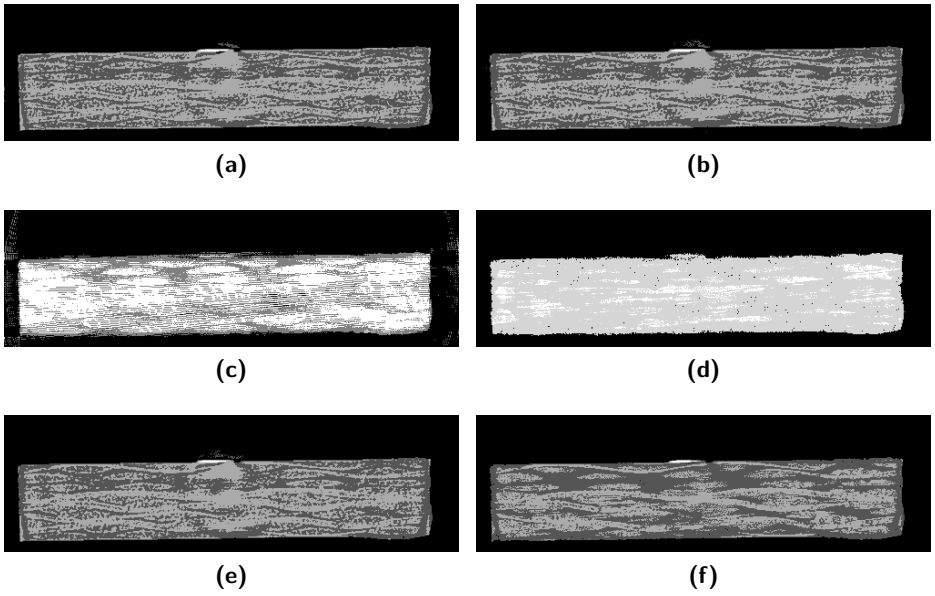

Figure 6.10: Reconstructions made of 1200 projections: (a) segmented CG for AC data, (b) DART for AC data [t0=20, t=10], (c) segmented CG for DPC data, (d) DART for DPC data [t0=20, t=1], (e) MV-DART [t0=[15,25],t=[10,1],ω=0.997](f) MV-DART with DFC-weighting [t0=[15,18,10],t=[10,1], ω=0.997, tDFrec=0.2, tDFproj=2].

MV-DART algorithm with DFC weighting on 300 projections, the reconstruction image has a similar or even better quality for further fiber segmentation compared to the single DART reconstructions of Fig. 6.10(a) and (c) on AC and DPC data of 1200 projections. This indicates that the MV-DART algorithm is a valid method when only limited projection data is available.

6.4 Conclusions & Work in progress

Based on the simulations and experiments performed in the previous section, the MV-DART algorithm with DFC weighting can be considered a promising technique for fiber segmentation which combines the fields of discrete tomography and image fusion for PCCT. It can be used to improve the reconstruction quality both in cases where different materials have the same attenuation coefficient or phase shift and in cases where the DPC image is corrupted by artefacts that originate from small angle scattering. In our lab, much effort is done at the moment to create

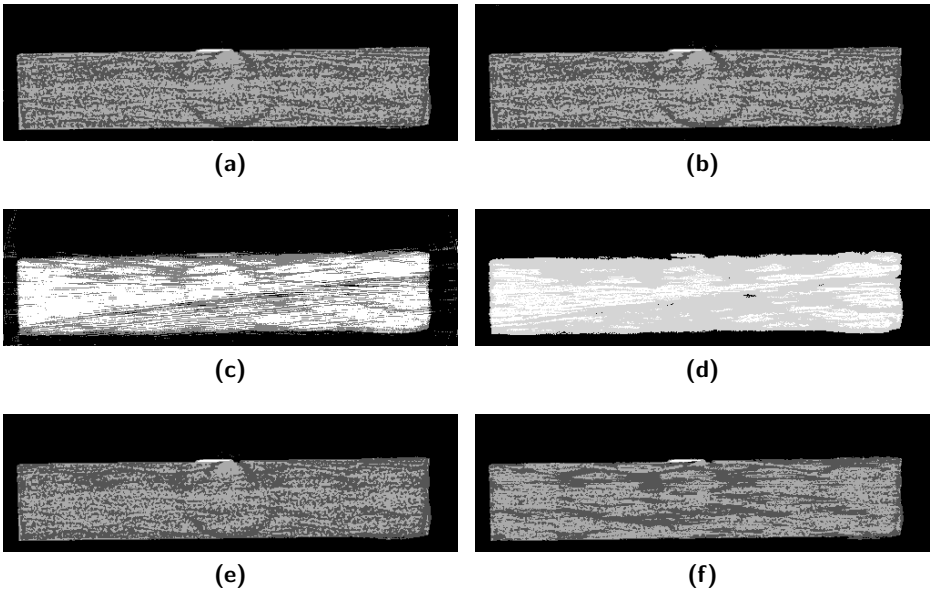

Figure 6.11: Reconstructions made of 300 projections: (a) segmented CG for AC data, (b) DART for AC data [t0=20, t=10], (c) segmented CG for DPC data, (d) DART for DPC data [t0=20, t=1], (e) MV-DART [t0=[15,25],t=[10,1],ω=0.997](f) MV-DART with DFC-weighting [t0=[15,25,10],t=[10,1], ω=0.997, tDFrec=0.1, tDFproj=2].

a simulator for TLGI PCCT data. Once this simulator is available, it will be interesting to perform more simulation studies with more accurately simulated data.
A possible improvement of the current MV-DART algorithm with DFC weighting can be obtained by studying the segmentation step. Currently, a very simple weighted Euclidean norm is chosen as a metric for segmentation. More accurate and complex segmentation methods like Markov Random Fields [16] exist of which the algorithm could benefit.

References

[1] M. Stampanoni, Z. Wang, T. Thüring, C. David, E. Rössl, U. van Stevendaael, T. Köhler, M. Trippel, G. Singer, R. Kubik-Huch, M. Hohl, and N. Hauser, "Toward clinical differential phase contrast mammography: preliminary evaluations and image processing schemes," *JINST*, vol. 8, no. C05009, 2013.

[2] F. Scholkmann, V. Revol, R. Kaufmann, H. Baronowski, and C. Kottler, "A new method for fusion, denoising and enhancement of X-ray images retrieved from Talbot-Lau grating interferometry," *Phys. Med. Biol.*, vol. 59, pp. 1425–1440, 2014.

[3] W. Haas, M. Polyanskaya, F. Bayer, K. Gödel, H. Hofmann, J. Rieger, A. Ritter, T. Weber, L. Wucherer, J. Durst, T. Michel, G. Anton, and J. Hornegger, "Image fusion in X-ray differential phase-contrast imaging," in *Proc. SPIE 8314, Medical Imaging 2012: Image Processing*, p. 83143U, 2012.

[4] C. Gusenbauer, M. Reiter, B. Plank, S. Senck, C. Hannesschläger, S. Renner, R. Kaufmann, and J. Kastner, "Multi-modal Talbot-Lau grating interferometer XCT data for the characterization of carbon fibre reinforced polymers with metal components," in *7th Converence on Industrial Computed Tomograhpy (iCT2017)*, 2017.

[5] M. Nielsen, T. Lauridsen, M. Thomsen, T. Jensen, M. Bech, L. Christensen, E. Olsen, M. Hviid, R. Feidenhansl, and F. Pfeiffer, "X-ray tomography using the full complex index of refraction," *Phys. Med. Biol.*, vol. 57, pp. 5971–5979, 2012.

[6] K. Batenburg and J. Sijbers, "DART: A practical reconstruction algorithm for discrete tomography.," *IEEE Transactions on Image Processing*, vol. 20, no. 9, pp. 2542–2553, 2011.

[7] W. van Aarle, K. Batenburg, and J. Sijbers, "Automatic Parameter Estimation for the Discrete Algebraic Reconstruction Technique (DART)," *IEEE Transactions on Image Processing*, vol. 21, no. 11, pp. 4608–4621, 2012.

[8] F. Bleichrodt, F. Tabak, and K. Batenburg, " SDART: An algorithm for discrete tomography from noisy projections ," *Computer Vision and Image Understanding*, vol. 129, pp. 63–74, 2014.

[9] R. Pua, M. Park, S. Wi, and S. Cho, "A pseudo-discrete algebraic reconstruction technique (PDART) prior image-based suppression of high density artifacts in computed tomography," *Nuclear Instruments and Methods in Physics Research A*, vol. 840, pp. 42–50, 2016.

[10] X. Zhuge, W. Palenstijn, and K. Batenburg, "TVR-DART: A More Robust Algorithm for Discrete Tomography From Limited Projection Data With Automated Gray Value Estimation," *IEEE Transactions on Image Processing*, vol. 25, no. 1, pp. 455–468, 2016.

[11] T. Sanders, "Discrete Iterative Partial Segmentation Technique (DIPS) for Tomographic Reconstruction," *IEEE Transactions on Computational Imaging*, vol. 2, no. 1, pp. 71–82, 2016.

[12] C. Paige and M. Saunders, "LSQR: An algorithm for sparse linear equations and sparse least squares," *ACM Transactions on Mathematical Software*, vol. 8, pp. 43–71, 1982.

[13] I. Jerjen, V. Revol, P. Schuetz, C. Kottler, R. Kaufmann, T. Luethi, K. Jefimovs, C. Urban, and U. Sennhauser, "Reduction of phase artifacts in differential phase contrast computed tomography," *Optics Express*, vol. 19, no. 14, pp. 13604–13611, 2011.

[14] W. van Aarle, W. J. Palenstijn, J. De Beenhouwer, T. Altantzis, S. Bals, K. J. Batenburg, and J. Sijbers, "The ASTRA Toolbox: a platform for advanced algorithm development in electron tomography," *Ultramicroscopy*, vol. 157, pp. 35–47, 2015.

[15] W. van Aarle, W. J. Palenstijn, J. Cant, E. Janssens, F. Bleichrodt, A. Dabravolski, J. De Beenhouwer, K. J. Batenburg, and J. Sijbers, "Fast and flexible X-ray tomography using the ASTRA toolbox," *Optics Express*, vol. 24, no. 22, pp. 25129–25147, 2016.

[16] H. Einarsdóttir, M. Schou Nielsen, R. Miklos, R. Lametsch, R. Feidenhans'l, R. Larsen, and B. Ersbøll, "Analysis of micro-structure in raw and heat treated meat emulsions from multimodal X-ray microtomography," *Innovative Food Science and Emerging Technologies*, vol. 24, pp. 88–96, 2014.

Part IV

Conclusions and Appendices

7 Conclusions

Numerous CT and PCCT applications deal with limited data problems caused by a limited projection geometry or a limited acquisition time. When classical reconstruction algorithms are exploited to solve these problems, the reconstructions are typically deteriorated by limited data artefacts.
In this thesis, multiple new reconstruction algorithms that cope with limited data artefacts have been proposed for use in tomography. Although the algorithms developed in this thesis are very different, they share the following characteristics:

1. For all methods, *prior knowledge* about the scanned object is incorporated into the acquisition model or reconstruction algorithm to improve the quality of the reconstructed images.

2. All methods are developed for a *specific application*, but can be generalized for application in other fields.

All methods described in this work can be divided into two cathegories: *transmission computed tomography* and *phase contrast computed tomography*. Hereafter, the main conclusions of Chapters 3-6 are discussed.

Part II: Inline X-ray inspection

Chapter 3 – NN-hFBP for fast inline X-ray inspection

In this chapter, the NN-hFBP (Neural Network Hilbert transform based Filtered Back Projection) algorithm was introduced. It is a fast and flexible algorithm for inline inspection of objects, in this case agricultural products. The algorithm combines several hFBP reconstructions into one final reconstruction image. The hFBP reconstructions are distinguishable by their filters, which are trained in advance in a neural network. Prior knowledge is used to train the neural network.

The proposed approach was validated on both simulated and experimental data, indicating its ability to generate reconstructions of sufficient quality in a realistic time frame which proves the feasibility of inline inspection.

Chapter 4 – Inline Crack Detection

In this chapter, an inline crack detection method for SVS adapters was proposed. The method consists of two consecutive steps. In the first step, reconstructions of the adapters with cracks are acquired with an adapted version of the NN-hFBP of Chapter 3. The method is able to provide acceptable reconstructions with highly limited projection data in a very short time frame. Secondly, a crack detection algorithm is applied on the reconstructions for classification of the adapters. The proposed technique was validated on a set of scanned adapters with and without cracks. The results reveal that the technique is able to detect cracks inside the adapters with a similar accuracy as the currently used offline pressure tests.

Part III: TLGI reconstruction Algorithms

Chapter 5 – Dual-axis Tomography

In this chapter, a dual-axis tomographic scan is proposed as an alternative to scans with an Eulerian cradle for the application of CFRP samples based on the knowledge that the fibers are oriented in two perpendicular directions. The samples are scanned twice with an intermediate rotation of 90 degrees. After holder substraction and registration of the absorption reconstructions, dual axis reconstructions of the DPC and DFC data are obtained with several reconstruction algorithms. For a dual-axis scan, no special equipment is acquired but directional information can still be recorded in more than one plane. The method was applied on a CFRP sample and results indicate that a dual-axis scan improves the reconstruction quality of the images for fiber detection even when the number of projections is greatly reduced.

Chapter 6 – Discrete Phase Contrast Computed Tomography: MV-DART

In this chapter, the MV-DART (MultiVariate Discrete Algebraic Reconstruction Technique) algorithm is proposed. The algorithm exploits both the AC and DPC projection data to generate a segmented reconstruction of the scanned object, highlighting the different materials inside the object. Two separate DART reconstructions are performed that are combined in the segmentation step where the Euclidean Norm is used for multivariate segmentation. The algorithm is validated both on simulation experiments and experimental data. The results show that the algorithm is able to significantly improve the discrete reconstruction. Furthermore,

the MV-DART algorithm with DFC weighting was proposed and validated on real data where the small angle scattering information is used to steer the segmentation towards the AC reconstruction. Results reveal an improved reconstruction quality compared to separate segmentation techniques.

Overall, with this work a step forward has been made in the field of fast inline inspection as well as in reconstruction algorithms for limited data with TLGI imaging. Results show that incorporating prior knowledge in the reconstruction or acquisition model can significantly improve the reconstruction quality for limited data problems.

A

List of common abbreviations

Common abbreviations

AC	Absorption Contrast
ART	Algebraic Reconstruction Technique
ASTRA	All Scales Tomographic Reconstruction Antwerp
CFRP	Carbon Fibre Reinforced Polymer
CG	Conjugate Gradient
CGLS	Conjugate Gradient Least Squares
CT	Computed Tomography
DART	Discrete Algebraic Reconstruction Technique
DFC	Dark Field Contrast
DPC	Differential Phase Contrast
FBP	Filtered Back Projection
FDK	Feldkamp-David-Kress algorithm
FSIM	Functional Similarity Index
GBI	Grating Based Interferometer
GPU	Graphics Processing Unit
hFBP	Hilbert transform based Filtered Back Projection
MAD	Most Apparent Distortion
MV-DART	Multivariate Discrete Algebraic Reconstruction Technique
NN-hFBP	Neural Network Hilbert transform based Filtered Back Projection
PCCT	Phase Contrast Computed Tomography
RMSE	Root Mean Squared Error
RNMP	Relative Number of Misclassified Pixels
SART	Simultaneous Algebraic Reconstruction Technique
SIRT	Simultaneous Iterative Reconstruction Technique
TLGI	Talbot Lau Grating based Interferometer

B

Scientific contributions

Journal articles

- *E. Janssens*, L.F. Alves pereira, J. De Beenhouwer, I.R. Tsang, M. Van Dael, P. Verboven, B. Nicolaï, and J. Sijbers, *"Fast inline inspection by neural network based filtered backprojection: Application to apple inspection"*, Case Studies in Nondestructive Testing and Evaluation, vol. 6, pp. 14–20, 2016.

- W. Van Aarle, W. J. Palenstijn, J. Cant, *E. Janssens*, F. Bleichrodt, A. Dabravolski, J. De Beenhouwer, K.J. Batenburg, and J. Sijbers, *"Fast and Flexible X-ray Tomography Using the ASTRA Toolbox"*, Optics Express, vol. 24, no. 22, pp. 25129–25147, 2016.

- L. F. Alves Pereira, *E. Janssens*, G.D.C. Cavalcanti, I.R. Tsang, M. Van Dael, P. Verboven, B. Nicolaï, and J. Sijbers, *"Inline Discrete Tomography system: application to agricultural product inspection"*, Computers and Electronics in Agriculture, vol. 138, pp. 117–126, 2017.

- T. De Schryver, J. Dhaene, M. Dierick, M.N. Boone, *E. Janssens*, J. Sijbers, M. Van Dael, P. Verboven, B. Nicolaï, and L. Van Hoorebeke, *"In-line NDT with X-ray CT combining sample rotation and translation"*, NDT&E International, vol. 89, pp. 89–98, 2016.

- *E. Janssens*, J. De Beenhouwer, M. Van Dael, T. De Schryver, L. Van Hoorebeke, P. Verboven, B. Nicolaï, and J. Sijbers, *"Neural network Hilbert transform based filtered backprojection for fast inline x-ray inspection"*, Measurement Science and Technology, vol. 29, no. 0340102, 2018.

Conference proceedings

- *E. Janssens*, D. Pelt, J. De Beenhouwer, M. Van Dael, P. Verboven, B. Nicolaï, and J. Sijbers, *"Fast Neural Network Based X-Ray Tomography of Fruit on a Conveyor Belt"*, Chemical Engineering Transactions, vol. 44, pp. 181-186, Frutic conference, Milan, Italy, 2015.

- *E. Janssens*, J. De Beenhouwer, M. Van Dael, P. Verboven, B. Nicolaï, and J. Sijbers, *"Neural Network Based X-Ray Tomography for Fast Inspection of Apples on a Conveyor Belt"*, IEEE International Conference on Image Processing, Quebec, Canada, pp. 917-921, 2015.

- *E. Janssens*, L. F. Alves Pereira, J. De Beenhouwer, M. Van Dael, P. Verboven, B. Nicolaï, and J. Sijbers, *"Fast Inline Inspection of Apples by a Neural Network based Filtered Backprojection Method"*, 6th Conference on Industrial Computed Tomography (iCT), Wels, Austria, 2016.

- L.F. Alves Pereira, *E. Janssens*, M. Van Dael, P. Verboven, B. Nicolaï, G. Cavalcanti, I.J. Tsang, and J. Sijbers, *"Fast X-ray Computed Tomography via Image Completion"*, 6th Conference on Industrial Computed Tomography (iCT), Wels, Austria, 2016.

- *E. Janssens*, S. Senck, C. Heinzl, J. Kastner, J. De Beenhouwer, and J. Sijbers, *"Fast Reconstruction of CFRP X-ray Images based on a Neural Network Filtered Backprojection Approach"*, 7th Conference on Industrial Computed Tomography (iCT), Leuven, Belgium, 2017.

- T. De Schryver, J. Dhaene, M. Dierick, M. Boone, *E. Janssens*, J. Sijbers, M. Van Dael, P. Verboven, B. Nicola, and L. Van Hoorebeke, *"In-line non-destructive evaluation of food with X-ray computed tomography using a non-standard conveyor belt trajectory"*, 7th Conference on Industrial Computed Tomography (iCT), Leuven, Belgium, 2017.

Conference abstracts

- *E. Janssens*, J. De Beenhouwer, T. De Schryver, L. Van Hoorebeke, M. Van Dael, P. Verboven, B. Nicolaï, and J. Sijbers, *"Fast in-line X-ray quality inspection of apples by segmentation with the NN-hFBP"*, EFFoST conference, Vienna, Austria, 2016.

- T. De Schryver, J. Dhaene, M. Dierick, M.N. Boone, *E. Janssens*, J. Sijbers, M. Van Dael, P. Verboven, B. Nicola, and L. Van Hoorebeke, *"In-line 3D X-ray*

CT inspection of food on a continuous high throughput conveyor belt ssytem", EFFost conference, Vienna, Austria, 2016.

- *E. Janssens*, J. De Beenhouwer, J. Sanctorum, S. Senck, C. Heinzl, and J. Sijbers, *"Dual axis Dark Field Contrast Tomography for visualisation of scattering directions in a CFRP sample"*, 4th Conference on X-ray and Neutron Phase Imaging with Gratings, Zürich, Swiss, pp 79-80, 2017.

- J. Sanctorum, *E. Janssens*, A.J. den Dekker, S. Senck, C. Heinzl, J. De Beenhouwer, and J. Sijbers, *"A workflow to reconstruct grating-based X-ray phase contrast CT images: application to CFRP samples"*, 4th Conference on X-ray and Neutron Phase Imaging with Gratings, Zürich, Swiss, pp.139-140 2017.